Application of External Torque on the Bacterial Flagellar Motor

Ren Chong Lim

St Catherine's College

University of Oxford

A thesis submitted in partial fulfilment of the requirements for the degree of *Doctor of Philosophy* at the University of Oxford

Hilary 2015

For Mum and Dad.

Acknowledgements

I would like to thank and acknowledge the various types of support and guidance which I received from the following people, without which the writing of this thesis would not have been possible.

First and foremost, I would like to thank my supervisor, Dr Richard Berry for offering me the opportunity to carry out this project. Richard has always been a great source of support, guidance, ideas and encouragement over the years. I also appreciate very much the freedom he has afforded me to learn all sort of different skills and techniques both related and not related to this project.

Next, I would like to thank and acknowledge both Dr Alexy Karenowska and Dr Kousuke Nogawa whose preliminary contributions were very important for later experiments involving the delivery of magnetic torque to the bacterial flagellar motor. Alexy has been very generous in sharing her knowledge of electromagnets and her four-pole prototype was crucial in the development of the three-pole electromagnets used in this thesis. Kousuke, an academic visitor from the University of Nagoya, worked very closely with me in developing the first variant of the magnetic bead-filament assay during his visit here at Berry Lab between September 2012 and February 2013.

I would like to thank the many members of Berry Lab, some of whom have left during my time, for making the lab a fun and stimulating place of discussion and debate. They include Dr Bradley Steel, Dr James Flewellen, Dr Irwin Zaid, Dr Ashley Nord, Dr Liang Le, Dr Aidan Russell, Bastiaan Leerkotte, Dewei Jia, Diana di Paolo, and Samuel Tusk. Notable mentions go to Dr Robert Ishmukhametov, Dr Mostyn Brown, Dr Murray Tipping and Dr Nicolas Delalez for going out of their way to educate me further on topics and techniques related to the fundamentals of molecular and microbiology.

I would also like to acknowledge various contributions from the support staff at the Department of Physics, in particular Simon Moulder and his team at the Clarendon Research Workshop who helped fabricate bits and pieces of the electromagnet, Tony Hickman for the Kapton and magnetic wire, and finally, the technicians based at the Undergraduate Teaching Lab, Keith Long and Mohamed Cheddi, for allowing me to borrow various kits and devices from the teaching labs which I needed at different stages of my project.

Most of the equipment funding came from BBSRC UK and my living expenses were mostly covered for using funds from the Human Resources Dana Scholarship awarded by the Prime Minister's Office of Brunei Darussalam.

I must not forget to mention my partner-in-crime in all matters not related to the bacterial flagellar motor, Swii Yii Lim, for the enormous support and encouragement she has given me for as long as I have known her. I very much appreciate her many attempts and efforts to broaden and expand the mind of a four-square person.

My final special mention has to go to my parents. I would not be where I am today if it is not for their unconditional support and encouragement.

Abstract

The bacterial flagellar motor is an ion-driven molecular rotary machine about 50 nm in diameter. It is the main source of propulsion for bacterial cells and has a mechanosensing ability, features of which are essential for survival. The details of its torque-generating mechanism still remains obscure and there is a strong need for a mechanical method to apply external torque to the bacterial flagellar motor in order to investigate this mechanism in greater detail.

In this thesis, I explored various methods to deliver torque at the single-molecule level, in particular the use of angular optical trapping and magnetic tweezers. The inability to establish a suitable method to attach birefringent particles to the motor made it very difficult to deliver optical torque to the motor. Further progress was made using magnetic tweezers. A magnetic bead assay was developed along with electromagnets capable of generating fast-rotating magnetic fields at magnitudes on the order of tens of mT.

Using the system of delivering magnetic torque developed, I was able to stall and rotate the motor forwards at speeds up to 220 revolutions per second and in the backwards direction. Stalling experiments carried out on the motor revealed that stator mechanosensing depends on torque and not rotation. Signatures of stators dropping out at low load experiments further confirm the load dependence of stators. The torque-speed curve measured between 0 Hz and 155 Hz is consistent with previous results obtained but requires that the superparamagnetic bead used behaved like a ferromagnetic particle, that is the particle can only follow the magnetic field at one angle. This is inconsistent with observations made on the same beads in which the same bead was capable of following the field at two different angles. The lack of a suitable model to describe the magnetic behaviour of the beads complicates the use of the angle between the magnetic field and the easy axis of the bead for torque measurements.

Contents

Chapter 1

The Bacterial Flagellar Motor

The ability for bacterial cells to navigate themselves in a viscous environment in search of more favourable regions is one hallmark of life. Motility is essential for bacteria as it allows the bacterium to explore, reproduce and survive in its native surroundings. For instance, motility due to chemotaxis allows bacteria to navigate towards regions containing higher concentration of chemical attractants (Berg & Brown, 1972; Adler, 1973).

The main provider of motility in bacteria is the flagellar motor, a rotary nano-machine embedded in the membrane. The bacterial flagellar motor allows the bacteria to convert energy derived from an electrochemical gradient of ions into mechanical energy. Depending on the species, the ions are either protons (H^+) or sodium ions (Na^+).

The motor forms the basal part of the flagellum organelle. Other components that make up the flagellum include a universal joint known as the hook and a helical filament. The motor rotates the helical filament through the hook. This filament has been observed to rotate at speeds up to several hundreds of revolutions per second (Kudo *et al.*, 1990; Magariyama *et al.*, 1994; Muramoto *et al.*, 1995). The flagellum is able to propel the bacterial cells at speeds up to several times its body length per

second. This is especially remarkable given that the bacterium is swimming in an environment having a low Reynold's number (Purcell, 1977).

The flagellar motor has a molecular mass of about 11 MDa and is made up of roughly 13 different proteins with varying copy numbers (Berg, 2003; Sowa & Berry, 2008). It has a diameter of approximately 45 nm. This makes the motor one of the largest molecular machines in the bacterial cell. Of approximately 50 genes involved in the expression and assembly of the flagellum, only about 25 genes produce the gene products present in the final structure.

During the early 1970s, it was widely agreed that bacteria swim by moving their flagella but the actual mechanism behind this motion was not known. Berg & Anderson (1973) used a schematic model to argue that bacteria swim by rotating their filaments. With the assistance of Dr. A. Klug, Calladine (1974) correctly pointed out that the schematic model proposed did not conclusively prove that bacteria swim by rotating their filaments. Nonetheless, the whole issue was put to bed when Silverman & Simon (1974) observed rotation of bacterial cell bodies using video microscopy and polyhook mutants of *Escherichia coli* (*E. coli*). The polyhook mutants carried two mutations, one of which stops the formation of flagellar filaments and the other prevents the cells from terminating the assembly of the hook structure (Silverman & Simon, 1972). These structures allowed the bacterial cells to be tethered to the microscope slide and rotation of such cells around this tethered point were observed. The rotational speeds recorded ranged from two to nine revolutions per second.

Subsequent experiments carried out on rotating cells by Larsen *et al.* (1974b) revealed that mutants that swim smoothly rotated their filaments predominantly in the counter-clockwise (CCW, viewed from filament to the motor) direction in the presence of chemical attractants. The filament has a left-handed helical structure and rotation in the CCW direction pushes the bacterium forward. Mutants which changed swimming direction continually often rotate their filaments in the clockwise (CW) di-

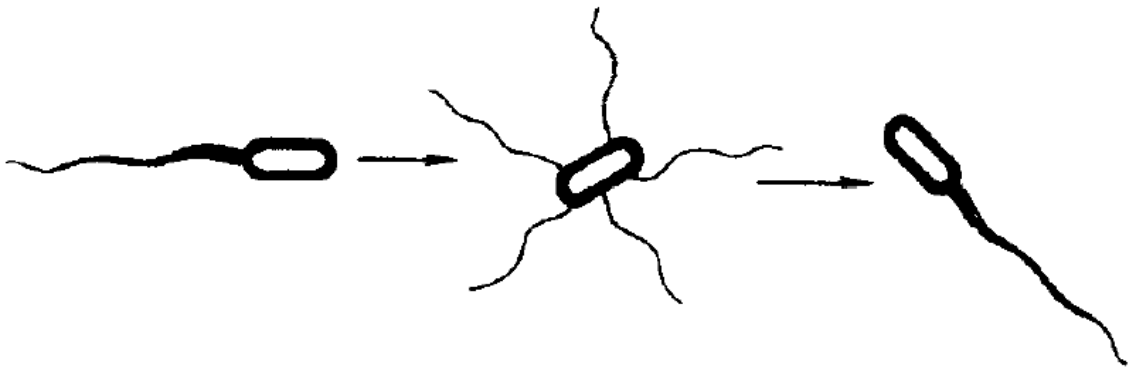

Figure 1.1. Line drawings of bacterial flagella visualised by high intensity dark field microscopy, taken from Macnab & Koshland (1974). A flagellar bundle is observed during smooth, fast motility. This is followed by a dispersion of the flagellar bundle during a tumble in which the cell randomly reorientates the direction of its body. Reformation of the flagellar bundle allows the bacterial cell to recover its smooth motility in a different direction.

rection. Furthermore, their experiments showed that non-chemotactic mutants never rotate in the CW direction. These observations were also confirmed in experiments carried out by Berg (1974) using a bacterial tracking microscope previously developed by Berg (1971).

It is well-understood that filaments in multiflagellated enteric bacteria, such as *E. coli* and *Salmonella enterica* serovar Typhimurium (*S. typhimurium*), form a bundle when all motors are synchronise to rotate in the CCW direction (Macnab & Koshland, 1974; Macnab, 1976). The bundle allows the bacterial cell to swim smoothly in a straight line. A single event in which the bacterial cell changes its swimming direction is called a "tumble". During this tumbling event, the bundle disperses as a result of one or more flagellar motors switching direction to rotate in the CW direction (Turner *et al.*, 2000). The cell reorientates itself randomly before all the motors are synchronised in the CCW direction to form a bundle. This allows the cell to swim smoothly in a different direction.

Even though *Sinorhizobium* (formerly called *Rhizobium*) *meliloti* is multiflagellated, it does not swim in the same manner as the enteric examples described above.

Instead, cells of *Sinorhizobium meliloti* change direction by modulating the speeds of each motor (Sourjik & Schmitt, 1996; Armitage & Schmitt, 1997).

Uniflagellated bacteria swim differently, for example, the cell body of *Rhodobacter sphaeroides* reorientates itself by relaxation of the polar flagellar filament from a normal helix to a short-wavelength, high-amplitude helix which coiled against the cell body (Armitage *et al.*, 1999). Another example includes the marine bacterium *Vibrio alginolyticus* (*V. alginolyticus*) whose single polar flagellum pushes or pulls the cell depending on the direction of rotation (Homma *et al.*, 1996). Uniflagellated cells execute a cyclic, three-step swimming pattern (forward, reverse, and flick) which is different from the run and tumble pattern observed for *E. coli* (Son *et al.*, 2013). The transition from reverse back to forward motion is characterised by a distinctive change in direction of travel, usually in the direction approximately 90° from the previous one, known as a flick. These flicking events have been shown to be associated with the compressive buckling of the hook (Son *et al.*, 2013). *Caulobacter crescentus* (*C. crescentus*), another uniflagellated bacterium was observed to flick after reversing for a few seconds before recovering motility in the forward direction (Liu *et al.*, 2014). It was also shown that *C. crescentus* simws more efficiently in the forward direction due to the helical path traced out by the cell.

Chemotaxis is by no means the only way bacteria navigate their environment but its chemosensory pathway is one that has been studied in great detail. We are able to achieve a detailed understanding of this pathway due to our ability to manipulate bacterial genetics relatively easily. This allows us to engineer various chemotactic and non-chemotactic mutants to probe this pathway (Blair, 1995; Wadhams & Armitage, 2004). Other navigational methods include phototaxis and aerotaxis, and they have been shown to depend on active electron transport (Armitage & Schmitt, 1997). Very little else is known about the actual sensing mechanism.

Another subsidiary function of the flagellar motor is its mechanosensing ability

(Belas, 2014). Mechanosensing is important for bacteria to sense surfaces which in turn triggers the onset of the formation of a biofilm. The biofilm is composed of extracellular matrix-forming polymers produced by the bacteria and they allow bacterial cells to live as members of organised surface-attached microbial communities (Monds & O'Toole, 2009). There is major clinical relevance in biofilms because they provide protective environments against stresses, immune responses, antibacterial agents, and antibiotics (Jefferson, 2004).

We may know a great deal about the general structure of the motor, its genetics, assembly and function (Berg, 2003), but we have yet to unravel the structural details behind its the torque-generating mechanism. This is due to the large size and complexity of the motor (Sowa & Berry, 2008). In addition, detailed atomic structures have been difficult to obtain especially since the motor is embedded in the membrane.

The aim of this thesis is to develop a single-molecule mechanical method capable of directly manipulating the motor speed which will allow us to investigate the torque-generating mechanism in more detail. One of the many quantities we aim to measure using this tool is the torque output from a single motor under different external conditions. In addition, we can use this technique to directly investigate how ion transit is coupled to rotation and torque (in both CW and CCW directions). Such an investigation will require bacterial strains that report the ion-flux using fluorescence.

The remainder of this chapter will deal with several topics of relevance to this thesis. I will first describe the overall structure of the flagellar motor, highlighting the proteins of importance in torque-generation. In this section, I will also discuss the core architecture of the flagellar motor that is conserved between different bacterial species. This is followed by an exposition on the energetics of the motor, how it can be manipulated and the torque-speed relationships we have been able to measure. Finally, I will describe our existing knowledge of the structural details and theoretical models of the torque-generating mechanism.

1.1 Structure

The bacterial flagellum consists of three parts: the filament, hook, and a membrane-embedded basal body which acts as a reversible rotary motor. The filament and hook are present outside the cell in gram-negative bacteria. The filament is about 10 μm long and 20 nm thin, and consists of a polymer of the flagellin proteins (FliC) arranged in a helix. The hook consists of a polymer of the hook proteins (FlgE) and acts as a universal joint.

Early electron microscopy studies of freeze-fractured components of the basal body of the flagellum revealed a set of rings up to about 45 nm in diameter that spans three layers of the cell envelope (DePamphilis & Adler, 1971a,b,c). Further structural details of the motor core were determined using single-particle image reconstruction by cryo-electron microscopy (cryo-EM), in which the reconstructed image is obtained by rotationally averaging images taken using cryo-EM (Stallmeyer *et al.*, 1989; Francis *et al.*, 1994; Thomas *et al.*, 1999, 2006). Images were often taken from samples that were fixed, frozen and purified. Recently, improved 3D projection and averaging methods have been developed to obtain larger and better resolved intact motor cores allowing flagellar structures to be obtained *in situ* (Murphy *et al.*, 2006). The improved reconstruction method is now commonly known as cryo-electron tomography (cryo-ET). A comparison of reconstructed images taken using cryo-EM and cryo-ET for the motor core of *S. typhimirium* is shown in Figure 1.2.

Several morphological domains make up the motor core. They are the L and P rings, the rod, the MS ring, the C ring, the stator and the export apparatus. A schematic diagram of one such motor core from a gram-negative bacterium is shown in Figure 1.3. The L ring is embedded in the outer lipopolysaccharide membrane while the P ring is embedded in the peptidoglycan cell wall. Both the L and P ring are thought to serve as bushings at their respective layers. It is currently not known if these rings rotate with the rod or remain fixed in the membrane. The rod connects

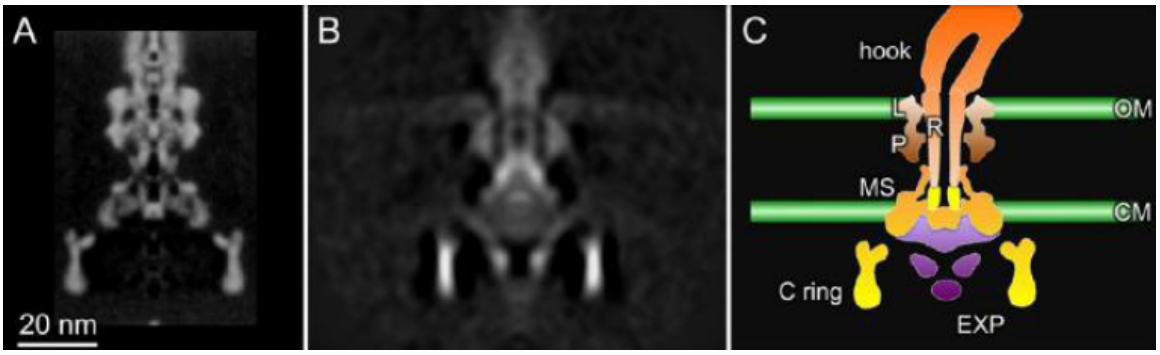

Figure 1.2. Comparison of single-particle reconstructed images of the motor core for *S. typhimirium* and a schematic diagram of its structure. **A**: Purified structure of the basal body determined using cryo-EM by Francis *et al.* (1994). **B**: Structure obtained *in situ* using cryo-ET by Chen *et al.* (2011). **C**: Schematic diagram of the motor structure for *S. typhimurium* taken from Zhao *et al.* (2014). OM, CM and EXP are respectively abbreviations for the outer membrane, cytoplasmic membrane and the export apparatus.

the MS ring and the hook and it behaves as a drive shaft to transmit torque. The MS ring is located at the cytoplasmic membrane and it was previously thought that it consisted of two separate rings (membrane, M, and supra-membranous, S, rings). This is no longer true as it was subsequently shown that the MS ring is a single ring made up of the protein FliF (Ueno *et al.*, 1992, 1994). The number of FliF present in the MS ring was determined using cryo-EM (Suzuki *et al.*, 2004). Representative 3D structures of the this ring were obtained by averaging cryo-EM images of rings in different orientations. The MS ring was deduced to follow a 26-fold symmetry indicating that there are 26 copies of FliF in the ring. The MS ring is the first part of the motor to be assembled and forms the platform on which the other parts of the motor is built (Aizawa, 1996; Macnab, 2003).

The cytoplasmic face of the MS ring is attached to the C ring consisting of the proteins FliG, FliM and FliN. A 3D reconstruction of the MS ring and the C ring is shown in Figure 1.4. The C ring is thought to be the site of torque generation (Khan *et al.*, 1991; Francis *et al.*, 1994; Katayama *et al.*, 1996) and is known as the "switch complex" as it regulates motor rotation (Yamaguchi *et al.*, 1986b,a). FliG

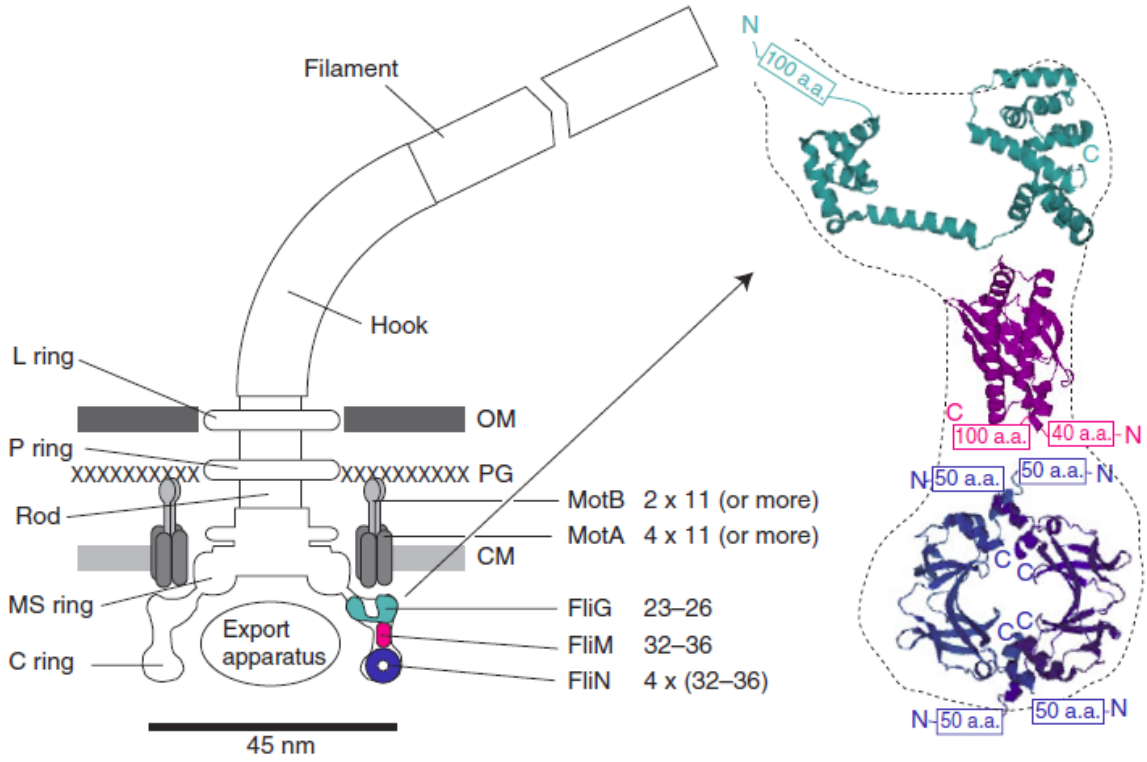

Figure 1.3. Left: Schematic diagram of a H^+-driven flagellar motor from a gram-negative bacteria, with the proposed location and copy number of proteins involved in torque generation. The motor spans the outer membrane (OM), the peptidoglycan cell wall (PG) and the cytoplasmic membrane (CM). Right: X-ray crystal structures of the truncated rotor proteins, FliG (cyan), FliM (magenta) and FliN (blue) in their proposed location and orientation in the C ring. The schematic diagram above was taken from Sowa & Berry (2008).

was believed to have a 1:1 stoichiometry with FliF from experiments in which various deletions were carried out in *FliF* and *FliG* genes to fuse both genes in-frame (Francis *et al.*, 1992). *In vitro* binding assays carried out by (Oosawa *et al.*, 1994) showed that FliG co-sedimented with the MS ring complex at a FliG/FliF molar ratio between 1:3 and 1:1. These indirect evidences led to the belief that the inner lobe of the C ring having a 26-fold symmetry. The middle domain of FliG provides a binding site for FliM (Brown *et al.*, 2007; Paul *et al.*, 2011; Lam *et al.*, 2012; Vartanian *et al.*, 2012; Lam *et al.*, 2013; Sircar *et al.*, 2014) and FliM has a 1:1 stoichiometry with a tetramer of FliN (Brown *et al.*, 2005). The stoichiometry between FliM and FliN was determined using velocity-sedimentation experiments and video densitometry of bands in gels containing dissociated subunits from purified FliN-FliM complexes. The outer lobe of the C ring is believed to contain a 32-fold to 36-fold rotational symmetry using data from cryo-EM carried out by Thomas *et al.* (1999). Plausible models as to how these proteins are organised to reconcile the mismatch in symmetry between the ring of FliG proteins and the overall C ring have been recently proposed by Stock *et al.* (2012). The models made use of crystal structures of FliG (Lloyd *et al.*, 1999; Brown *et al.*, 2002; Lee *et al.*, 2010; Minamino *et al.*, 2011), FliM (Park *et al.*, 2006), FliN (Brown *et al.*, 2005) and the FliG-FliM complex (Paul *et al.*, 2011). More data incorporating specific structural constraints are required to further refine the overall structure of the C ring.

It is worth noting that the C ring is not a static structure. The proteins making up the C ring are dynamic in nature and can exchange with the pool of available proteins in the cytoplasm. Turnover of these proteins have been observed for FliM and FliN (Delalez *et al.*, 2010, 2014; Branch *et al.*, 2014).

The stator is an energy-converting membrane protein complex in the motor and it interacts directly with the C ring to generate torque. The stator subunits are known to anchor to the peptidoglycan cell wall and form ion-channels which span

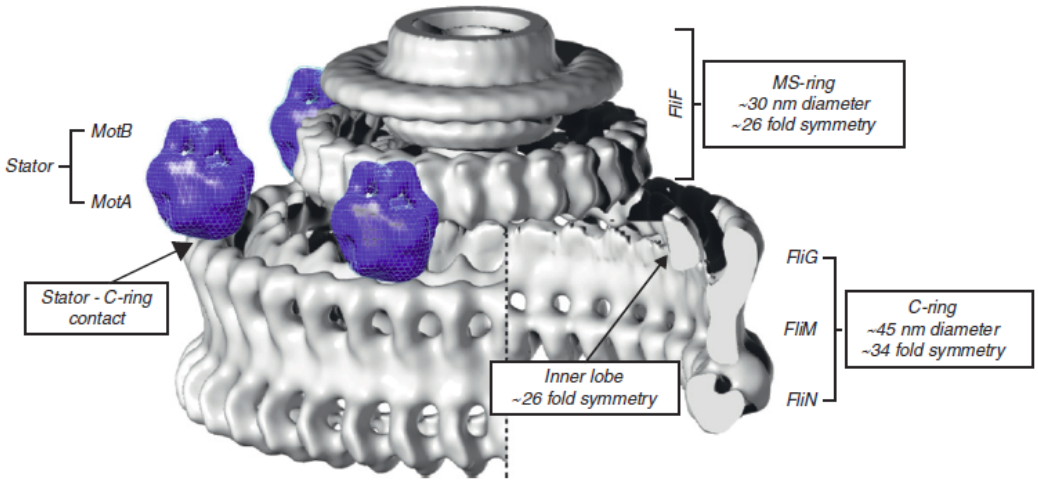

Figure 1.4. Architecture of the MS ring and the C ring of the bacterial flagellar motor. Stator complexes are shown in blue and positioned above the outer lobe of the C ring where they are seen in images taken using cryo-ET. The diagram above was taken from Stock *et al.* (2012).

the cytoplasmic membrane (De Mot & Vanderleyden, 1994; Sato & Homma, 2000; Blair, 2003). Freeze-fracture cryo-EM showed that the stators are located in rings at the periphery of the rotor and each ring can contain a variable number of units depending on the species and the individual motor (Coulton & Murray, 1978; Khan *et al.*, 1988, 1992). The stators are dynamic and the turnover of these proteins were observed using total-internal-reflection fluorescence microscopy of green-fluorescent-protein (GFP) labelled stators (Leake *et al.*, 2006). The dynamic nature of these stators were also captured in speed-time traces recorded from rotating polystyrene beads attached to motors (Reid *et al.*, 2006). These traces showed that up to at least 11 stators can be present in the motor at any one time. The dynamic nature of the stator can be attributed to the ability for stators to sense and detect external load, an ability known as mechanosensing (Lele *et al.*, 2013; Tipping *et al.*, 2013a).

In H^+-driven motors such as those of *E. coli* and *S. typhimurium*, the stator is a complex made up of two proteins, MotA and MotB (Blair & Berg, 1990; Togashi *et al.*, 1997). MotA and MotB are thought to form a complex with stoichiometry A_4B_2 (Kojima & Blair, 2004; Braun *et al.*, 2004). The electrostatic interactions between

MotA and FliG in the C ring are understood to generate torque (Garza *et al.*, 1995; Zhou *et al.*, 1998a,b).

In Na^+-driven motors such as *V. alginolyticus*, the stators are made from the proteins PomA and PomB (Hirota *et al.*, 1981). The Mot and Pom proteins share a high degree of homology in their sequence and appear to be equivalent in both topology and function (Asai *et al.*, 1997; Yorimitsu & Homma, 2001). Two further proteins, MotX and MotY, are found only in Na^+-driven motors from *V. alginolyticus* (McCarter, 1994a,b). They form the T ring in the periplasmic space and are understood to play a role in stablising the Na^+ stators (Terashima *et al.*, 2006).

The export apparatus is a large complex located below the MS ring and is known to pump proteins which make the hook and the filament outside the cell (Macnab, 2003; Minamino & Namba, 2004). In addition to using the ion-motive force (IMF), the export apparatus uses the energy obtained from the hydrolysis of ATP (ATP-hydrolysis) to complete the export process following a type III pathway (Fan & Macnab, 1996; Minamino & Namba, 2008; Paul *et al.*, 2008). This apparatus has garnered interest from the medical community because of its homology in sequence, structure and functionality to the pathogenic type III secretion system which is involved in the injection of virulence factors into host cells (Macnab, 2004).

A comprehensive study of intact flagellar motors using cryo-ET work was carried out by Chen *et al.* (2011). They were able to obtain reconstructed images of the motors at resolutions at a few nanometres for a number of bacterial species including *E. coli*, *Campylobacter jejuni* (*C. jejuni*) and *Hylemonella gracilis* (*H. gracilis*). A comparison of motor structures obtained from these species is shown in Figure 1.5.

Even though the overall architectures vary between species, the MS ring, the C ring, the rod, and the export apparatus have the same overall configuration as those determined in *S. typhimirium* shown in Figure 1.2. This suggests that the core components of the motor and their interactions are conserved between species.

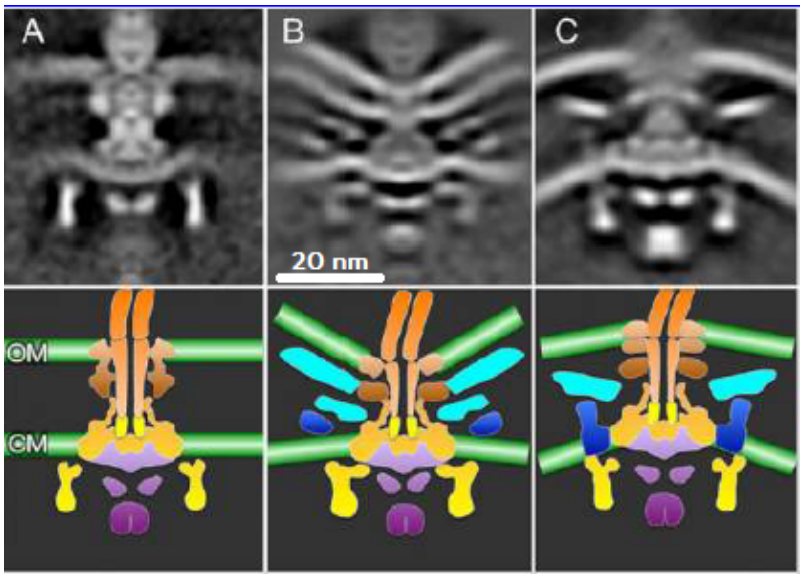

Figure 1.5. **Top**: *In situ* flagellar motor structures from different gram-negative bacteria, **(A)** *E. coli*, **(B)** *C. jejuni*, and **(C)** *H. gracilis*, determined by cryo-ET taken from Chen *et al.* (2011). **Bottom**: Schematic diagrams of the same motor structures shown above with the same colour scheme as found in Figure 1.2. The regions coloured in blue are stators while the regions coloured in cyan represent periplasmic structure which are believed to keep stators intact. Figures on the bottom were taken from Zhao *et al.* (2014).

Notable periplasmic structures (coloured in cyan) and stator complexes (coloured in blue) were observed for *C. jejuni* and *H. gracilis* which suggests that they are closely associated with the stator. High-throughput genetic screening carried out for *C. jejuni* has revealed several potential candidates responsible for these periplasmic structures but further cryo-ET and biochemical studies have to be carried out to identify the exact protein (Gao *et al.*, 2014).

These periplasmic structures are not present in *E. coli* and *S. typhimirium*. This could be attributed to the dynamic nature of the stators in these organisms which may contribute to the lack of clearly defined stator structures in the reconstructed cryo-ET images. The implications of less dynamic stators in ε-proteobacteria on their ability to mechanosense is not known.

It is clear that the flagellar motor is a very complex molecular machine. The assembly of such a machine is a finely tuned biochemical process involving highly

regulated expression of motility genes and ordered assembly of proteins (Kubori *et al.*, 1992; Macnab, 2004; Chevance & Hughes, 2008). Systematic investigation of cryo-ET images obtained from various mutants in a single species will allow us to develop a model as to how the flagellar motor is assembled, an attempt of which has been carried out for *Borrelia burgdorferi* (Zhao *et al.*, 2013). Such studies carried out in conjunction with a systematic investigation of how motors are assembled in different species can paint a picture of how the bacterial flagellar motor evolved over time between species.

Another topic of interest related to the evolution of the flagellum is the origin of the type III secretion system. It has been suggested that type III secretion system for virulence factors evolved from the type III secretion system for exporting flagellar proteins as the flagella are far more ancient than the organisms that are targets for virulence factors (Macnab, 2004). Macnab (2004) noted that it is very well possible that the original targets were other bacteria and it could be argued that the less complex structure of the virulence secretion system evolved to a more complex one such as the flagellum than the other way around. More structural data collected across different species and various virulence factors are required to resolve this long-standing debate.

1.2 Energetics

1.2.1 Energy transduction

The bacterial flagellar motor is a molecular machine which converts chemical energy derived from an ion gradient to mechanical energy. It operates very close to the level of thermal energy in which the natural counting unit for energy is k_bT, where k_b is Boltzmann's constant and T is the absolute temperature. Liquid environments are required for the study of biological specimens and so the absolute temperature is

usually very close to room temperature. There is little variation in k_bT and it can be assumed to be approximately equal to 4×10^{-21} J.

The free energy obtained from a single ion passing through the cytoplasmic membrane is defined as the elementary charge of the ion multiplied with the ion-motive force (IMF). The IMF is an analogue of the Newtonian force operating in terms of electric charge instead of distance (c.f. the electro-motive force). Two components make up the IMF: an electrical potential and a electrochemical transmembrane potential. The IMF can be defined as

$$\text{IMF} = V_m + \Delta\mu/q \tag{1.1}$$

where V_m is the membrane voltage, $\Delta\mu = k_bT\ln(C_{in}/C_{out})$ is the transmembrane chemical potential difference with C_{in} and C_{out} representing the internal and external ion concentrations respectively, and q is the elementary charge of the ion. The free energy associated with a single ion transit is $6k_bT$ which corresponds to an IMF value of about -150 mV.

The main form of biological free energy in most species is the proton-motive force (PMF) where the ion of interest is the proton (H^+) (Mitchell, 1966). Early direct experiments aimed at identifying the main source of free energy for the bacterial flagellar motor were carried out on gram-positive *Streptococcus* and *Bacillus subtilis* (*B. subtilis*) cells. The first direct evidence that the bacterial flagellar motor is driven by ions and not ATP-hydrolysis, another source of biological free energy, was the observation of flagellar rotation in starved *Streptococcus* and *B. subtilis* cells energised using an artificial membrane potential or pH gradient (Manson *et al.*, 1977; Matsuura *et al.*, 1977). This confirmed earlier indirect evidence that the motor was ion-driven, evidence of which was obtained using mutants from *E. coli* and *S. typhimirium* (Larsen *et al.*, 1974a). Soon after, the existence of Na^+-driven motors was

discovered in alkalophilic *V. alginolyticus* and *Bacillus* cells (Chernyak *et al.*, 1983; Hirota *et al.*, 1981; Hirota & Imae, 1983).

The ability to genetically engineer chimeric mutants became available towards the late 1990s. The first chimera was made by replacing the PomA in *V. alginolyticus* with the homologous MotA from the H^+-driven *R. sphaeroides* motor (Asai *et al.*, 1999). Various functional chimeras were engineered subsequently in order to investigate the details of ion selectivity behind in the stator complex (Asai *et al.*, 2000a,b, 2003; Gosink & Hase, 2000; Yorimitsu *et al.*, 2003). The results revealed that there is no single determining component for ion-selectivity.

Even so, one of the many mutants engineered has been very useful in studies involving Na^+ kinetics behind the flagellar motor. This particular chimeric *E. coli* mutant uses stators PomA and PotB, a fusion protein between the MotB from *E. coli* and PomB from *V. alginolyticus* (Asai *et al.*, 2003). Changing the Na^+-motive force (SMF) has a lesser effect on the functionality of proteins compared to changing the pH. It is also known that the SMF is not central to the metabolism of *E. coli*. It is thus more straightforward to work with Na^+-driven motors as the SMF can be controlled over a wide range without damaging cells or motors.

This chimeric motor has been used to show stepping in the bacterial flagellar motor (Sowa *et al.*, 2005). Low values of SMF were used which sufficiently slowed the motor, allowing the steps to be resolved. The 26 steps observed in stepping has been attributed to the periodicity of the interface between the inner lobe of FliG in the C ring and FliF in the MS ring.

Hybrid motors that express both H^+ and Na^+ stators exist in nature in species such as *B. subtilis* and *Shewanella oneidensis* (*S. oneidensis*) (Ito *et al.*, 2004, 2005; Paulick *et al.*, 2009; Thormann & Paulick, 2010). They contain multiple sets of stator genes in order to express both types of stators but only a single set of genes to express the rotor.

Attempts to show motors operate using a hybrid-fuel system have been carried out on *E. coli* mutants with inducible H^+ and chimeric Na^+ stators (Sowa *et al.*, 2014). These stators were induced by arabinose or iso-propyl-β-D-thiogalactopyranoside (IPTG). It was observed that Na^+ stators dominated at high Na^+ concentrations ($[Na^+]$). These units were then replaced by H^+ units when Na^+ was removed. This demonstrated that stators compete for spaces in a motor and are sensitive to their own ion-gradient.

Various experiments have been carried out over the past three decades to understand the effects of IMF on the rotation of flagellar motors. Meister *et al.* (1987) reported an average ion flux (1240 ± 240) protons travelled through each motor per revolution in experiments conducted in a dense suspension of swimming *Streptococcus* cells. It is worth noting that several assumptions have been taken to estimate this flux such as the number of cells present and the volume of each cell.

The first attempt to directly control the membrane voltage across the flagellar motor was carried out by (Fung & Berg, 1995). This was achieved by drawing filamentous *E. coli* cells into custom-made micropipettes and energised using an external voltage source. A schematic of this method is shown in Figure 1.6. Since the motor operates in a regime having low Reynold's number, the torque, τ, was determined using

$$\tau = \gamma\omega \tag{1.2}$$

where γ is the rotational drag coefficient of the marker cell attached to the motor and ω is the angular frequency of the motor. It was observed that the torque measured was proportional to PMF up to -150 mV. The result obtained was consistent with earlier indirect measurements where the membrane voltage was controlled using different K^+ diffusion potentials (Manson *et al.*, 1980; Khan *et al.*, 1985; Meister *et al.*, 1987). De-energisation experiments further carried out using sodium azide or carbonyl cyanide *m*-chlorophenylhydrazone (CCCP) yielded consistent results (Gabel & Berg, 2003).

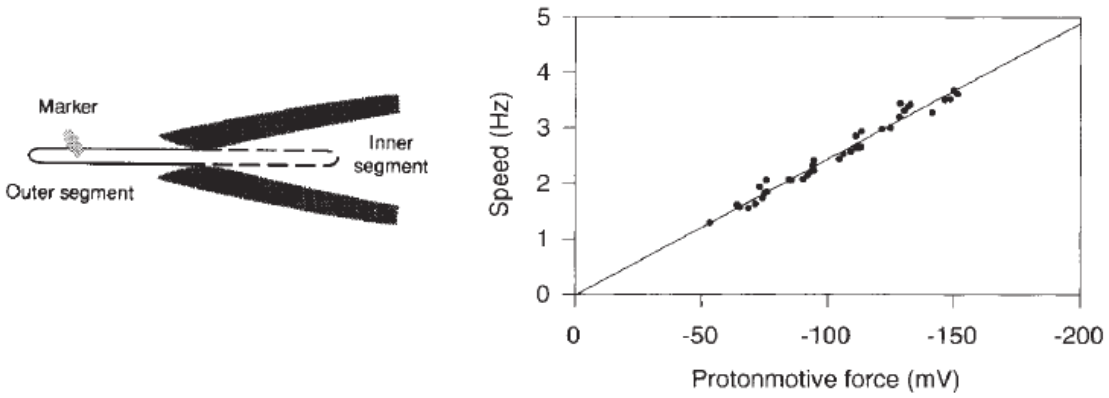

Figure 1.6. Left: Schematic of voltage-clamp method using filamentous *E. coli* cells held in custom-made micropipettes. **Right**: Flagellar rotational speed, equivalent to torque, is proportional to the PMF between 0 and about -150 mV. The figure above was taken from Fung & Berg (1995).

More recently, it is possible to control the PMF *in vivo* by illuminating *E. coli* cells capable of expressing the light-driven H^+-pumping proteorhodopsin (pR) (Tipping *et al.*, 2013b).

The chimeric Na^+-driven mutant mentioned previously has been very useful in investigating how SMF affects flagellar rotational speed. A linear relationship between torque and SMF was observed in *V. alginolyticus* (Sowa *et al.*, 2003), a result consistent with previous experiments carried out on H^+-driven motors. In order to study the effects of SMF on flagellar motors in greater detail, a method of loading a Na^+ fluorescent indicator, Sodium Green, into chimeric mutants was developed by Lo *et al.* (2006). Methods to vary the pH and external Na^+ concentration were later developed (Lo *et al.*, 2007) which allowed one to measure and control the two components of the SMF, the membrane voltage (V_m) and the Na^+-concentration gradient ($\Delta\mu$). They were able to control values of V_m between -140 mV and -85 mV, and $\Delta\mu$ between -50 mV and 40 mV. The added level of control combined with the ability to work with beads having smaller diameter allowed the authors to explore the relationship between the two components of the SMF in greater detail. At high load (using

beads having a diameter of 1 μm), it was shown that the contribution from V_m was equivalent to $\Delta\mu$. At low loads, the contribution from V_m was no longer equivalent to $\Delta\mu$. This non-equivalent contribution of the two components of the SMF at low loads was similarly observed in *V. alginolyticus* (Sowa *et al.*, 2003).

Lo *et al.* (2013) further conducted a systematic investigation of 25 different combinations of V_m and $\Delta\mu$ in which the authors were able to determine the number of ions per revolution per stator unit at high load. This can be achieved by assuming that Stokes efficiency is close to 1 as torque and SMF is tightly coupled to rotation at high load and the motor operates close to the thermodynamic equilibrium in this high-load regime (Berry & Berg, 1999). Thus the work done against viscous drag is nearly equal to the free energy of the ions driving the motor. Equating the work done per revolution with the free energy supplied by the ion-number n yields

$$n = \frac{2\pi \times \tau}{q \times \mathrm{SMF}} \tag{1.3}$$

Beads of various diameters were attached to truncated filaments of the motor and the overall drag coefficient was given by $\gamma = \gamma_b + \gamma_f$ where γ_b and γ_f are the rotational drag coefficients of the bead and the filament stub respectively. The rotational drag coefficient of the bead is the sum of the rotational drag of a bead rotating on its axis and an eccentricity factor which takes into account the orbital trajectory of the bead, i.e. $\gamma_b = 8\pi\eta r_b^3 + 6\pi\eta r_b r_e^2$ where η is the viscosity of water, r_b is the radius of the bead and r_e is the eccentricity of the orbit of the bead. The rotational mode considered here is one where the a bead is stuck onto a rotating stub as opposed to the mode where the bead precesses around the stub. The hook behaves as an universal joint and the bead is unlikely to precess around the stub. The rotational drag of the filament was determined empirically as described in Inoue *et al.* (2008) because the length of the filament stub was not known.

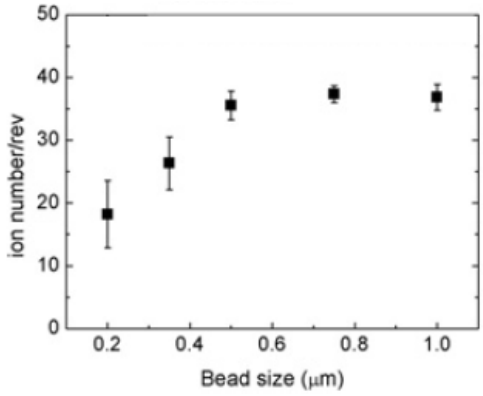

Figure 1.7. Plot of ion number n against bead sizes for fully energised motors (maximum V_m at pH 7, 85 mM [Na^+]). This figure was taken from Lo *et al.* (2013).

It is important to note that n is a lower limit to the actual number of ions N passing through the motor. As the load decreases, the work done by the motor decreases and the efficiency of the motor of is no longer close to 100%.

A plot of n against various bead sizes for fully energised motors is shown in Figure 1.7. In the high-load regime, n was estimated to be (37 ± 2) independent of SMF, V_m and $\Delta\mu$. This value is different from the 26 steps observed by Sowa *et al.* (2005) but the rotational symmetry of the outer lobe of the C ring is within the experimental error. This is clear evidence that the stator interacts with the outer lobe of the C ring. The space between the inner lobe and outer lobe of the C ring has low electron density and may behave as an elastic link between rings. In addition, it is possible that there is an elastic link between the stators and the cell wall. Both elastic contributions working in tandem could deliver a smooth torque to the inner ring, blurring the signature of the outer rotational symmetry of the C ring (Lo *et al.*, 2013).

At lower loads, n was observed to decrease which is consistent with the reduced efficiency in this regime and n is no longer expected to be a good approximation to the actual number of ions passing through the motor per revolution.

One possible method to measure ion-flux directly is to combine the ability to load

Sodium Green dyes into cells expressing single flagellar motors with a mechanical method to exert external torque. Furthermore, we can extend these experiments to investigate the reversible nature of the motor. Is it possible to observe ion-pumping when the motor is physically rotated in the reverse direction?

1.2.2 Torque-speed relationships

An important quantity in the study of any rotary motor is the torque-speed relationship as it allows one to develop models to describe how the motor works. Figure 1.8 summarises measurements of the torque-speed relationships of flagellar motors obtained from different species and different methods from 1987 until the year of publication of Sowa & Berry (2008).

Models of varying complexity, ranging from simple kinetic models (Oosawa & Hayashi, 1986; Berry & Berg, 1999) to more complicated models (Läuger, 1988; Berry, 1993; Xing *et al.*, 2006), have been developed to describe the mechano-electrochemical cycle of the flagellar motor. Models dealing specifically with stepping in the bacterial flagellar motor, or both stepping and the mechano-electrochemical cycle have also been developed (Mora *et al.*, 2009a,b; Meacci & Tu, 2009; Meacci *et al.*, 2011). The rate at which models are developed has diminished lately due to the lack of experimental data, in particular torque-speed relationships obtained from single motors.

The torque for most of the relationships obtained was varied by changing viscous load on the motor. This can be achieved by either varying the viscosity of the surrounding medium or the size of the load attached to the motor. Early experiments measured the rotation of motor either using video microscopy of cells tethered to the coverslip using hydrophobic means or scattering of light from flagellar bundles (Manson *et al.*, 1980; Lowe *et al.*, 1987). Scattering has also been used to determine the torque exerted by *C. crescentus* cells (Li & Tang, 2006). The first use of polystyrene beads attached to motors using hydrophobic means, an assay also known

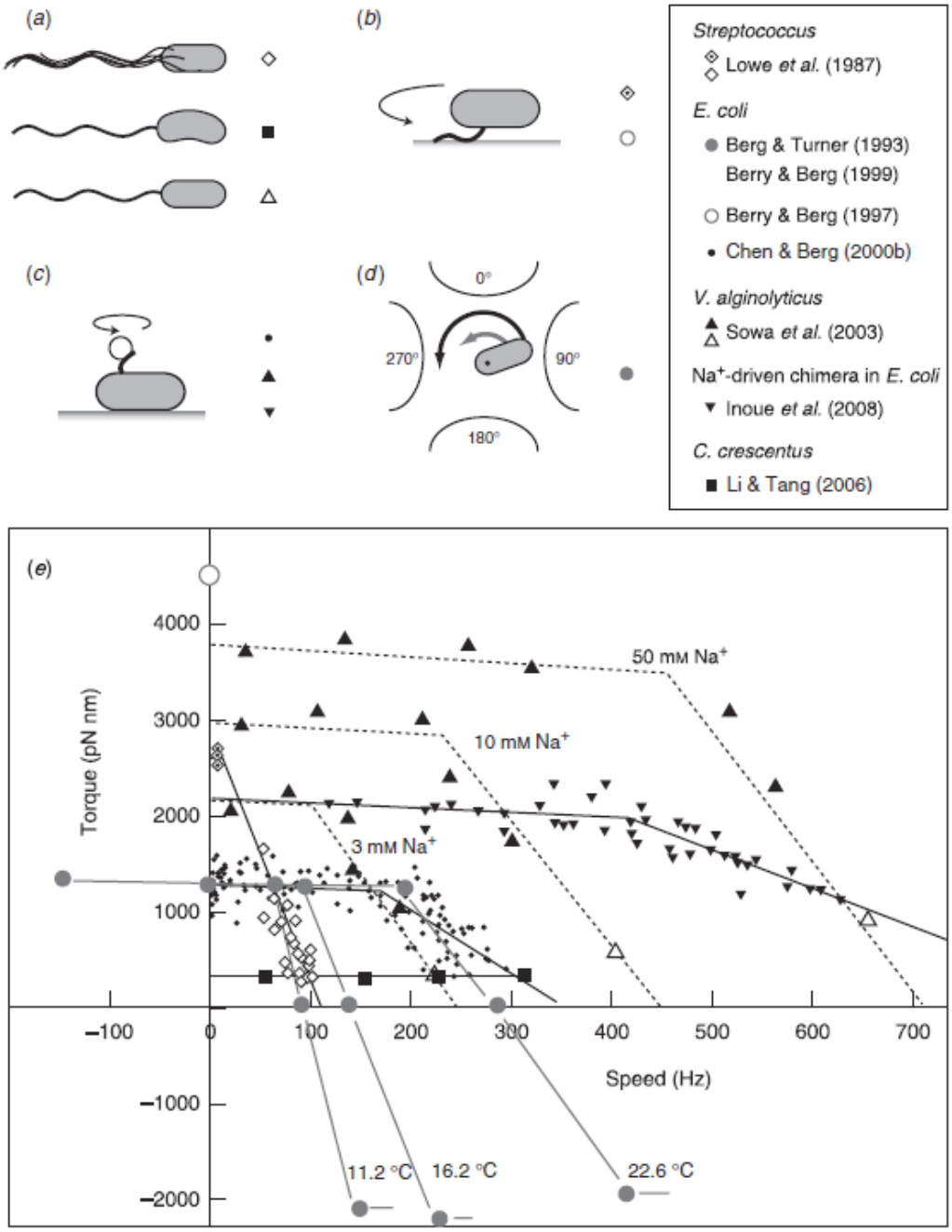

Figure 1.8. Summary of torque-speed relationships taken from Sowa & Berry (2008). (a)–(d) Methods of measuring torque-speed relationships. **(a)** Scattering from swimming cells. **(b)** Tethered cells. **(c)** Beads attached to flagella (bead assay) **(d)** Electrorotation of tethered cells where the microelectrodes generate a megahertz rotating electric field at the cell that applies an external torque (black arrow), which adds to the motor torque (grey arrow). **(e)** Torque-speed relationships obtained for flagellar motors from various species using the different methods indicated using the same set of symbols used in (a)–(d).

as the polystyrene-bead assay, was reported by Ryu *et al.* (2000). The rotational speed for this assay was usually determined from the scattered light of a weak focused laser beam on the spinning polystyrene bead attached to the motor, a method also known as back-focal-plane (BFP) interferometry (Gittes & Schmidt, 1998). This assay has been used extensively in obtaining torque-speed curves for motors from *E. coli* (Chen & Berg, 2000a), *V. alginolyticus* (Sowa *et al.*, 2003) and the Na^+-driven chimera (Inoue *et al.*, 2008).

The only torque-speed curves measured from single motors were obtained using electrorotation on tethered cells (Washizu *et al.*, 1993; Berg & Turner, 1993; Berry *et al.*, 1995; Berry & Berg, 1996, 1999). An electric field rotating at megahertz frequencies polarises the cell body inducing a dipole moment. Due to the finite time required for redistribution of charges, the dipole moment either leads or lags the electric field which gives rise to a torque. The speed at which the cell can be made to rotate is a direct function of the applied electric field strength. Using this method, it was possible to drive the cell both backwards and forwards beyond the zero-torque speed.

All torque-speed relationships measured so far exhibit certain general characteristics. The torque at zero speed, also known as the stall torque, is estimated to be (1260 ± 190) pNnm using the polystyrene-bead assay by Reid *et al.* (2006). Another estimate for the zero-torque speed is (1300 ± 50) pNnm using tethered cells measured by Meister & Berg (1987) and Blair & Berg (1988).

As the speed increases from stall, there is a plateau of nearly constant torque up to a "knee" speed of several hundreds of Hz. The torque plateau represents a regime where motion of the attached load in the mechano-electrochemical cycle is rate-limiting. In this regime, the system is understood to operate with high efficiency close to the thermodynamic equilibrium and is proportional to the IMF (Sowa *et al.*, 2003; Lo *et al.*, 2013).

As the load is reduced and the motor speeds up, a knee is observed which represents the beginning of the point at which internal processes inside the motor become rate-limiting. Finally, there is a sharp transition to a regime where torque falls linearly towards the zero-torque speed. The zero-torque speed is understood to be a measure of the limiting rate of the mechano-chemical cycle in the absence of load. Previous assumption that the rate-limiting step is the binding of Na^+ ions was shown to be too simplistic (Lo *et al.*, 2013). Further systematic exploration of torque-speed curves obtained from single motors near the zero-torque speed will shed more light on the possible rate-limiting step(s).

It is important to note that torque-speed curves measured using the polystyrene bead assay is often a composite of both the IMF and the number of stators (stator number). A publication in which I was recently involved in has shown that the stator number varies with external load (Tipping *et al.*, 2013a), the result of which was also observed in Lele *et al.* (2013). These experiments demonstrated that stators behave as mechanosensors. In addition, it has been previously established that the stability of stator binding to the flagellar motor also depends upon the IMF (Kojima *et al.*, 2009; Tipping *et al.*, 2013b). The only known torque-speed relationships obtained for which the stator number has been carefully stated are those measured by (Ryu *et al.*, 2000) and (Lo *et al.*, 2013), data of which are both shown in Figure 1.9.

In the work carried out by Ryu *et al.* (2000), they noted that extrapolating these curves will yield the same zero-torque speed. This result was not constrained by the experimental data collected and depended more on the results of the modelling carried out in the paper. They were not able to collect sufficient data at low loads as polystyrene beads with diameters less than 200 nm scatter very little light. Data obtained at low loads, down to beads having a diameter of 60 nm, were only recently achieved using the gold-bead assay (Yuan & Berg, 2008). Rotational measurements of the gold-bead assay are carried out using a back-scatter dark-field microscope (Sowa

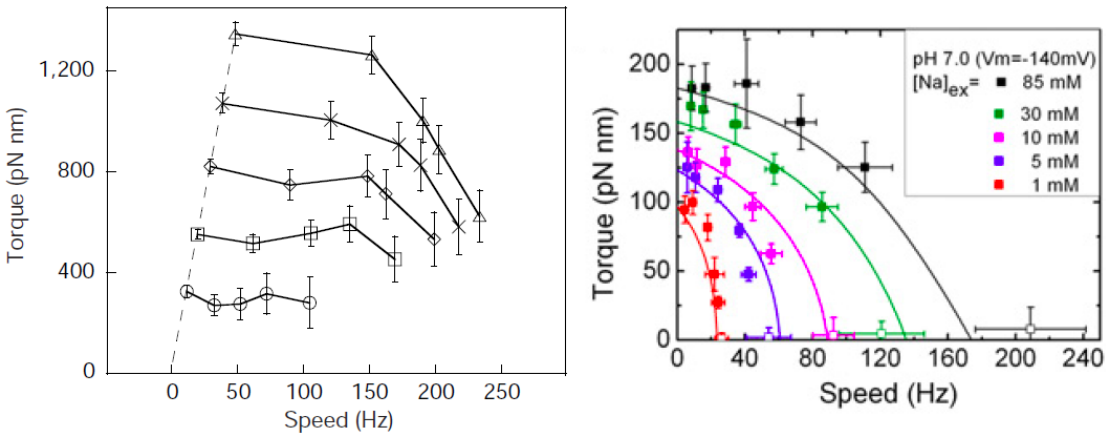

Figure 1.9. Left: Torque-speed relationships for motors having 1 (bottom) to 5 (top) stators, taken from Ryu *et al.* (2000). **Right**: Torque-speed relationships of fully energised motors having a single stator at different external Na^+ concentrations ($[Na]_{ex}$), taken from Lo *et al.* (2013).

et al., 2010). This microscope exploits the high signal-to-noise ratio of back-scattered light from gold beads compared to back-scattered light from the bacterial cell body.

The zero-torque speeds measured by Lo *et al.* (2013) for fully energised motors having a single stator reveal a different characteristic. Extrapolated zero-torque speeds were shown to vary with $\Delta\mu$ which is due to the various internal rate-limiting process. There are a few candidates for this internal process at work: ion-binding at low concentration, ion-transit, or ion-release into the cytoplasm at high concentration. Further results obtained by the same authors showed that the zero-torque speed decreases more steeply with $\Delta\mu$ than with V_m.

On a final note, it has been shown that torque-speed curves are affected by temperature (Berg & Turner, 1993; Inoue *et al.*, 2013) and solvent-isotope effects (Chen & Berg, 2000b; Yuan & Berg, 2010). Such factors are known to directly affect ion-transition rates and thus display more pronounced effects at low loads.

1.3 The torque-generating mechanism

1.3.1 Structural details

There is a large body of work aimed at unravelling the structural details behind the torque-generating mechanism. We understand that torque is generated as a result of interactions between stators and the rotor. More detailed understanding of this mechanism is currently hindered by the lack of crystal structures obtained for the stators even though some progress has been made for certain domains of MotB (O'Neill & Roujeinikova, 2008; Roujeinikova, 2008a,b; Kojima *et al.*, 2009; O'Neill *et al.*, 2011; Reboul *et al.*, 2011; Andrews *et al.*, 2013). Most of our existing understanding of the topology, stoichiometry and likely active regions of the stators is due to the extensive studies carried out using biochemical cross-linking and site-directed mutagenesis, work of which is largely reviewed in Sowa & Berry (2008) and Morimoto & Minamino (2014).

MotA is made up of four membrane-spanning α-helices, two short periplasmic loops and two extensive cytoplasmic regions while MotB consists of a N-terminal cytoplasmic region, one membrane-spanning α-helix and a C-terminal periplasmic region which contains a well-conserved peptidoglycan binding domain (PBD) that is known to bind to the peptidoglycan (Dean *et al.*, 1984; Stader *et al.*, 1986; Chun & Parkinson, 1988; De Mot & Vanderleyden, 1994). The general structure of one of the cytoplasmic regions of MotA contains two charged residues that interact with five charged residues in the C-terminal domain of FliG to generate torque (Lloyd & Blair, 1997; Zhou & Blair, 1997; Zhou *et al.*, 1998a). A schematic of the stator topology and interaction between the rotor and a single stator in *E. coli* motors in shown in Figure 1.10.

It is widely accepted that the tertiary structures of MotA and MotB are the same as PomA and PomB (Li *et al.*, 2011) but comparative studies of the rotor-

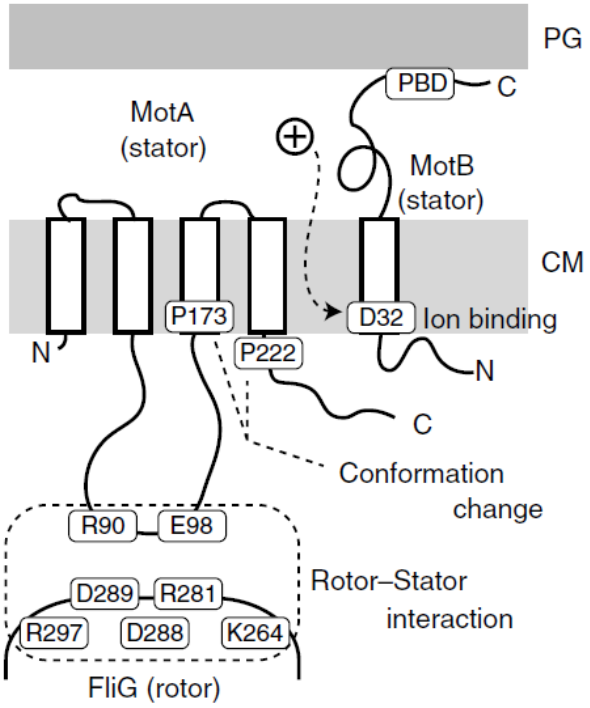

Figure 1.10. A side-view schematic of the stator topology and interaction between the rotor and a partial stator complex containing 1 MotA and 1 MotB in *E. coli* motors. The figure above was taken from Sowa & Berry (2008).

stator interaction between the two species differ slightly (Yorimitsu *et al.*, 2002, 2003; Yakushi *et al.*, 2006). There are additional charged residues in the cytoplasmic C-terminal region of PomA and these residues are speculated to participate in various inter- or intra-molecular interactions (Obara *et al.*, 2008). It is very well possible that additional interactions are required in order to maintain stability of these Na^+ stators which operate in high-salt environments.

The ion-binding site in the stator in *E. coli* has been established to be the highly conserved residue Asp32 and it is postulated that each stator contain two ion-channels, each containing one MotB-Asp32 residue (Braun & Blair, 2001). The ion-channels are indicated as orange-shaded regions in Figure 1.11. The equivalent ion-binding residue in *V. alginolyticus* is Asp24 in PomB (Yakushi *et al.*, 2004; Terashima *et al.*, 2010).

Various biochemical studies such as simulating ion-binding to MotB32 (Braun *et*

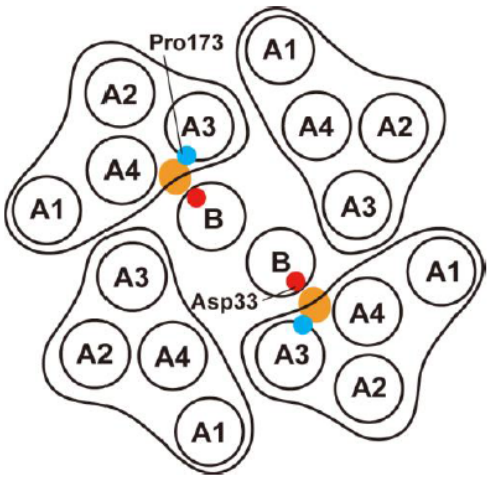

Figure 1.11. Top-down view of cross-section of the stator complex showing α-helix domains of MotA and MotB for *Salmonella*, taken from Morimoto & Minamino (2014). The orange-shaded regions represent the H^+-conducting pathways. MotB-Asp33 of *Salmonella* corresponds to MotB-Asp32 of *E. coli*.

al., 1999; Kojima & Blair, 2001) and site-directed mutagenesis on other conserved residues, Pro173 and Pro222 (Sharp *et al.*, 1995a,b), provide indirect evidence for a conformational-change model of the torque-generating mechanism. Ion-flux coordinates conformational changes in MotA via MotB-Asp32. These conformational changes involve motions about the MotA proline residues that lead to a cyclic interaction with FliG which generates torque. Torque-speed relationships of single motors obtained from stator variants carrying different site-directed mutagenesis will be useful to determine the rate-limiting process at low loads.

Recently, there has been a growing interest in understanding the actual mechanism behind stator mechanosensing, in particular the details of how varying the external load leads to structural changes in the stator (Morimoto & Minamino, 2014). This is led primarily by availability of crystal structure data obtained for the periplasmic region of MotB (Roujeinikova, 2008b; Kojima *et al.*, 2009). Such structural changes will affect its stability and the number of stators engaged with the rotor. It has previously been shown that stators are recruited with increasing external load (Lele *et al.*,

2013; Tipping *et al.*, 2013a) and the stability of stator binding to the motor depends on the IMF (Kojima *et al.*, 2009; Tipping *et al.*, 2013b). Stators were observed to leave both Na^+- and H^+-driven motors when the IMF is disrupted and they return when the IMF is restored.

Several mechanisms have been proposed from the direct measurements of stator dynamics with load. Lele *et al.* (2013) suggested that any instantaneous increase in torque will result in an equal and opposite force on the peptidoglycan cell wall to which the stators are anchored. The structure of the stator will change as increment in forces causes conformational changes in neighbouring sites or in the binding properties of the stators. Shape changes such as this can increase the probability of additional stator binding. The authors went on to discuss how this mechanism can explain why stators leave when the IMF is disrupted. The stators no longer apply force to the peptidoglycan layer and binding sites might not remain open thus promoting unbinding of the stators. However, no plausible candidates for where the conformational changes take place were put forward.

In the main model proposed by Tipping *et al.* (2013a), we noted that the observed decrease of stator number with reduced IMF and load, pointed towards the common feature of reduced torque generated by each stator. The reduction in torque can be attributed to a simple conformational change that altered the length of the linker between the cytoplasmic domains of each stator and its point of anchorage to the peptidoglycan layer. This conformational change could provide the necessary mechanosensitivity as the free-energy difference between long and short forms would contain a term equal to the length change times the force on a stator. There is indirect evidence that such a mechanism is at play, in the form of conformational changes observed in the periplasmic domain of MotB coupled to other conformational changes observed in MotB during stator binding (Hosking *et al.*, 2006; Kojima *et al.*, 2009; Morimoto & Minamino, 2014). Systematic investigation of MotB variants with mutant

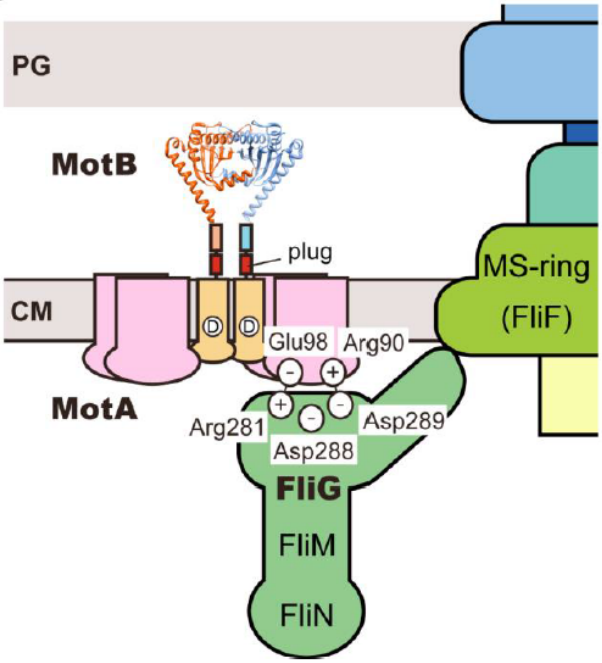

Figure 1.12. Side-view schematic of the stator-rotor interface showing the periplasmic region of MotB in greater detail, taken from Morimoto & Minamino (2014). The C-terminal domain of MotB, known to bind to the peptidoglycan cell wall (PG), is represented by the crystal structure shown above the plug.

periplasmic regions can help test this model. A schematic showing the periplasmic region of MotB in more detail is shown in Figure 1.12.

We also proposed more complicated mechanisms could be at work. These mechanisms will involve conformational changes in other motor components which are sensitive to the change in stator-rotor interactions caused by external load, such as FliL (Raha *et al.*, 1994; Jenal *et al.*, 1994). If this is true, such mechanisms will form precursors to a surface-sensing transduction pathway which will lead to the formation of biofilm. Some of these surface-sensing mechanisms are very well understood for other bacterial species and have been extensively reviewed by Belas (2014).

1.3.2 Models

Various models have been developed to describe how ion transit through the stator is coupled to rotation (Berg & Turner, 1993; Berry, 2000). Torque-speed relationships

discussed earlier often form the main quantitative prediction of these models. The other quantitative prediction that can be obtained using these models is the dynamics of stepping. The models developed can be divided into three main categories: ion-turbines, ion-turnstiles and ion-binding with conformational change (Berry, 2000). An illustration of these categories of models are shown in Figure 1.13. In order for any of the models developed from any of these categories to be valid, they must first be consistent with known facts about the structure of the motor. Following this, they must be able to reproduce torque-speed relationships and stepping-dynamics already measured for the flagellar motor.

In models that fall under the ion-turbine category, the path of the ions across is partly formed by elements in the stator and partly by elements in the rotor. These elements carry a particular elementary charge and are arranged in lines which are tilted with respect to each other. These elements can be either half-binding sites on the rotor and stator that need to be aligned to bind a ion (Läuger, 1977) or ion-channels in the stator that interact by long-range electrostatic interactions with the tilted lines of charge on the rotor (Berry, 1993; Elston & Oster, 1997; Walz & Caplan, 2000). Models that fall under this category follow a power-stroke mechanism in that free energy supplied by the influx of ions is directly coupled to the creation of a torque-generating state. Thermal fluctuations are not necessary for rotation to occur. This category of models has been ruled out as there is no structural data to suggest the existence of tilted lines of charges.

In an ion-turnstile model, ions from outside the cell are deposited onto the rotor by one type of stator channel. The rotor rotates by thermal diffusion and carries the ion into a second type of stator channel, allowing the ion to travel into the interior of the cell (Khan & Berg, 1983; Meister *et al.*, 1989). Unless the channel is protonated, the rotor is bound to a stator unit and is unable to move between the two types of channel. In order to prevent the motor from diffusing in the backward direction, a

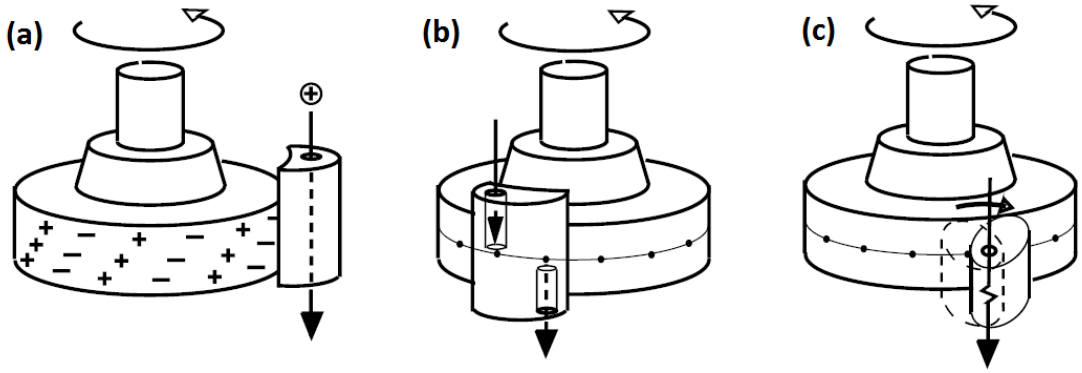

Figure 1.13. The three categories of models for the flagellar motor. **(a)** Ion-turbine. **(b)** Ion-turnstile. **(c)** Ion-binding with conformational change. The figure above was taken from Berry (2000).

potential barrier to backward rotation is required. As such models that fall under this category follow the mechanism of a thermal-ratchet, in that the role of the free energy supplied by the influx of protons is to save thermal fluctuations in a certain direction than to directly create a torque-generating state (Berry, 2000). There is currently no plausible candidate for the residue where the ion-binding site directly couples to the rotation of the rotor. Recent findings from the work of Lo *et al.* (2013) have established that ion transit in the flagellar motor is channel-like, rather than carrier-like, thus providing further indirect evidence against this category of models. Furthermore, experiments carried out using optical tweezers by (Berry & Berg, 1997) have shown that there is no barrier to backward rotation.

The final model of interest is the model incorporating ion-binding with conformational change. In this model, ion transit through a stator is coupled to a cycle of conformational changes of the stator. This in turn exerts torque on the rotor, either by long-rage electrostatic or short-range steric interactions (Läuger, 1988). Earlier mention of an indirect physical evidence in the form of conformational changes observed in MotA linked to the proposed ion-binding site in MotB hint towards this model (Kojima & Blair, 2001). Most models developed in the past decade are derivatives of this category of models where a power-stroke mechanism and tight-coupling between

ion transit and rotation are assumed. Early models developed employed a multi-step kinetic model due to its simplicity Berry & Berg (1999) but more recent models developed make use of differential equations, in the form of Langevin's equations, relating the coordinates of the stators and its relative position to the rotor. These models were used to generate torque-speed relationships which have been compared to averaged torque-speed measurements measured for a population of motors.

Torque-speed relationships measured from single motors will greatly refine the model incorporating ion-binding with conformational change. Furthermore, we can extend this study to motors having stator variants containing various site-directed mutations to regions where conformational change is hypothesised to take place. Such studies will help refine the conformational change models which will contribute massively to our understanding of the finer details of the torque-generating mechanism.

1.4 Summary

In this chapter, I began with a discussion on why bacteria swim and how they achieve motility using the flagellar motor. This was followed by an overview of the general structure of the flagellar motor. Even though the overall architectures vary between species, a symmetric core consisting of the MS ring, the C ring, the rod, and the export apparatus is conserved.

The second section dealt with the energetics of the motor. An overview of various techniques to energise the motor was presented along with the most recent estimate of ion-flux through the motor. The importance of torque-speed relationships was emphasised in the same section as it is a useful test of conformational-change models which describe the torque-generating mechanism. Most torque-speed measurements obtained to date are taken in bulk and we are currently lacking torque-speed measurements from single motors obtained under various external conditions.

The latest findings from torque-speed curves obtained for Na^+-driven motors showed that there are several candidates for the internal rate-limiting processes at low load. In addition, stators engaged in torque generation exhibit some degree of mechanosensitivity. It has been shown that the stator number depends on external load. As such, interpretation of torque-speed curves in which stator numbers are not known must be treated with care. This motivates the need for combined fluorescence and torque-speed measurements where intensity of the GFP-tagged stator can be used to count the numbers present at the motor.

The last section in this chapter dealt with details of the torque-generating mechanism of the motor. Possible conformational changes in the stator related to ion transit and its stability were discussed. Careful choice of stator variants having site-directed mutagenesis at regions where conformational changes are known to take place can help resolve the internal rate-limiting step at work. Following this, the chapter ended with a short overview of the different types of models developed to describe the torque-generating mechanism. The conformational-change model is currently the most plausible model to describe this mechanism.

There is a strong need for a mechanical method capable of delivering external torque to the flagellar motor. Such a tool will greatly facilitate measurements of torque-speed relationships from single motors in the near future. Combining this method with the ability to measure ion-flux will allow us to investigate how ion transit couples to rotation in greater detail. This will also allow us to distinguish more carefully the rate-limiting processes that take place at low load. Finally, we intend to use this technique to study stator dynamics, in particular, their on/off rates at different rotational speeds of the motor. Stators are mechanosensitive and we are interested to find out the rates at which they drop out at low loads.

Chapter 2

Methods to Apply External Torque

Recent developments of various methods to deliver torque at the single-molecule level have led us to consider the possibility of exploring them for use on the bacterial flagellar motor. There are three known methods to deliver torque at the single-molecule level: electrorotation, optical trapping and magnetic tweezers. In the first section, I will discuss the use of electrorotation in studies previously carried out on the bacterial flagellar motor. In the following section, I will describe how optical trapping can be used to deliver torque to the bacterial flagellar motor. The chapter ends with an overview of existing magnetic tweezers. Both the theory behind the behaviour of superparamagnetic beads in a rotating magnetic field and an estimate for the magnetic field strength required for studies involving the bacterial flagellar motor are presented here.

2.1 Electrorotation

Electrorotation was the first direct application of external torque on the bacterial flagellar motor (Washizu *et al.*, 1993; Berg & Turner, 1993). A megahertz rotating electric field induces a dipole moment in the cell body which will lag or lead the electric field. The phase lag produces a constant torque on the particle and the

torque exerted depends on the field intensity, rotational rate and conductivity of the cell and the solution. The relationship between these quantities is complex and can be non-intuitive as noted by the possibility of a particle rotating in the opposite direction to the field rotation (Jones, 2003).

Experiments carried out using electrorotation on the bacterial flagellar motor were capable of rotating the cells backwards at speeds up to -400 Hz and forward up to 400 Hz. Early experiments appeared to show that the motor behaved as a thermal ratchet in which the data obtained showed a barrier against backwards rotation (Berg & Turner, 1993). This was later shown to be an artefact of the electrorotation method (Berry *et al.*, 1995; Berry & Berg, 1996, 1999), confirmed using optical trapping experiments (Berry & Berg, 1997).

The field intensities used were often very high leading to heating problems. Also, imperfections in the shape of the field led to various lateral forces which pulled the cells and broke the motor. In an attempt to minimise the field intensity used, the drag of the load was decreased (Saxl, 2007). This involved the design of a bead assay in which highly polarisable 0.83 μm-diameter carboxy-modified polystyrene beads decorated with 0.2 μm-diameter plain polystyrene beads were attached to motors on fixed cells. The yields of such an assay were however extremely low and it was very difficult to reproduce the experiments with high efficiency. Due to the reasons given above, I did not consider the use of electrorotation to apply external torque to the bacterial flagellar motor.

2.2 Optical traps

Optical trapping, first demonstrated by Ashkin *et al.* (1986), has long been used to study the movement and force produced by linear molecular motors such as kinesin and myosin (Svoboda *et al.*, 1993; Molloy *et al.*, 1995). Even though light-induced

rotation of macroscopic objects have been reported back in the mid-1930s by Beth (1936), it was not until the seminal work carried out by Friese *et al.* (1998) that it was conclusively shown that optical traps could be used to both align and rotate microscopic particles. Optical traps capable of rotating microscopic particles are formally called angular optical traps (Forth *et al.*, 2013) and are also known either as optical torque wrenches (La Porta & Wang, 2004) or optical spanners (Simpson *et al.*, 1997). Such traps have been used extensively in microrhelogy (Bishop *et al.*, 2004) and the study of torsional stiffness and supercoiling of DNA (Oroszi *et al.*, 2006; Deufel *et al.*, 2007).

Even though angular optical traps have not been used to deliver torque to bacterial flagellar motors, optical traps have been previously used to exert torque on single motors (Pilizota *et al.*, 2007). Pairs of polystyrene beads were stuck to motors and a fast moving trap was used to deliver a force and rotate the outer bead in the pair. Using this method, the authors were able to rotate the outer bead at speeds up to 425 Hz. The speed-time trace of this experiment is shown in Figure 2.1 in which stators were observed to drop out when rotated at increasingly high speeds. This result was previously attributed to motor damage but it is now believed that this can be attributed to stators dropping out at low load.

There were several difficulties that arose from this method, the first of which was related to the difficulty in calibrating the stiffness of the bead-pairs to obtain absolute torque values. The torque exerted by the trap was recognised to depend on three factors: the combined effect of the linear force on the bead-pair and the reaction force at the motor, the alignment of a non-spherical trap on a non-spherical particle, and the polarisation of the trap. The combination of all these factors led to considerable angular variation in the torque which was not predictable. The second issue is the use of relatively high laser powers at about 65 mW. It was argued that the laser power used did not pose considerable photodamage to the motor as the power

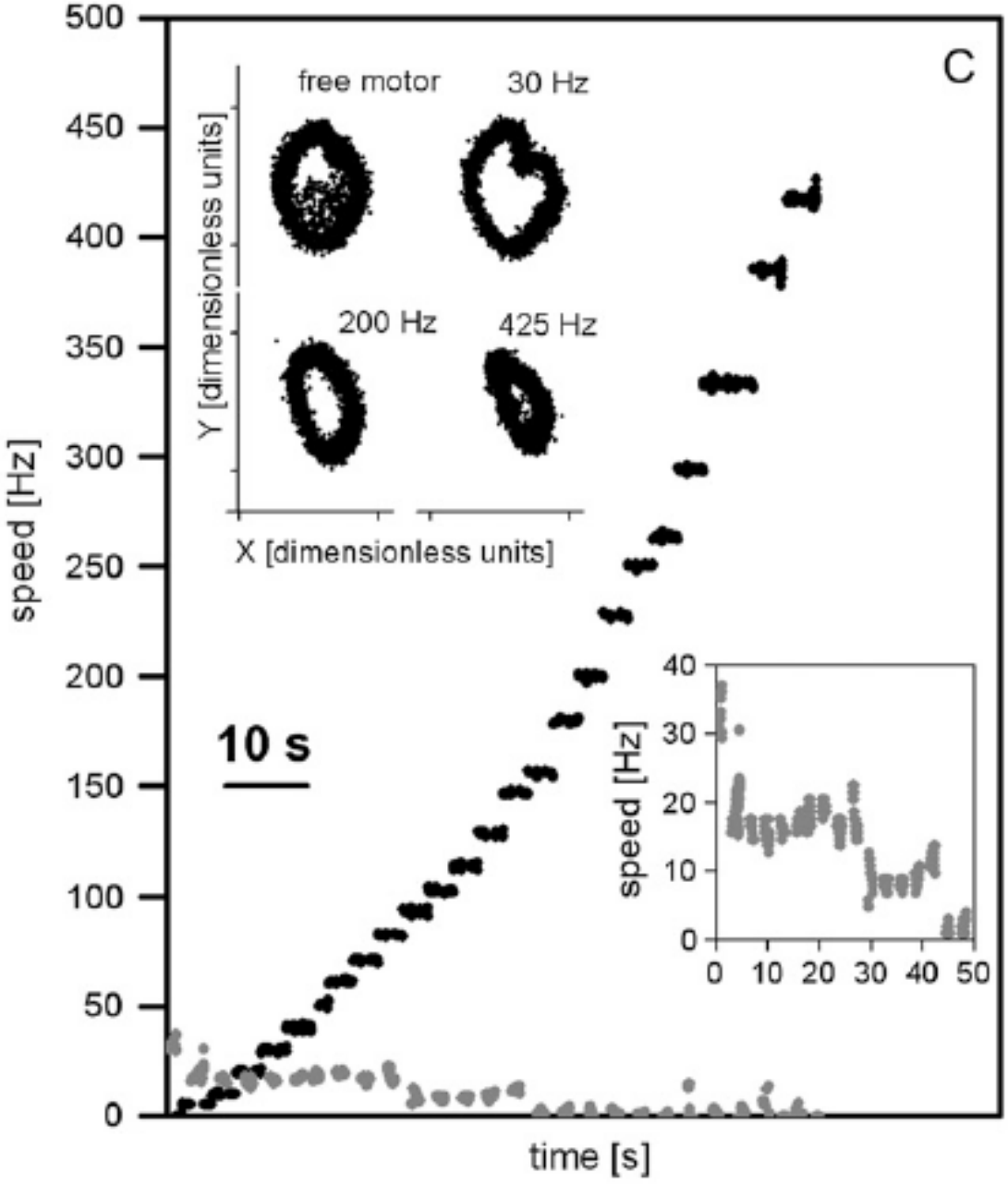

Figure 2.1. Speed-time trace of a 500-nm bead-pair in which the bead followed the rotating optical trap at speeds up to 425 Hz (black). At regular intervals the trap was shuttered and the bead pair was allowed to rotate freely (gray, expanded in lower insert). Stepwise reduction in freely rotating speed was observed. X-Y signal of the bead at different speeds is shown in the upper insert. The laser power used was 65 mW and the figure above was taken from Pilizota *et al.* (2007).

used was considerably less than the amount that would lead to photodamage (Neuman *et al.*, 1999). Nonetheless, I am interested in a method that uses considerable less laser power, on the order of a few mW. For the reasons given above, I did not consider the use of fast moving optical traps to deliver torque to the motor.

2.2.1 Principles behind angular optical trapping

Early examples of angular optical trapping involved breaking the rotational symmetry of either the microscopic particle, the input trapping beam or both (Friese *et al.*, 1998; Higurashi *et al.*, 1999; O'Neil & Padgett, 2002; Galajda & Ormos, 2003; Bishop *et al.*, 2003). The torque imparted to the particle was determined using the rotational drag equation for torque, $\tau = \gamma\omega$ where τ is the torque, γ is the rotational drag coefficient and ω is the angular frequency. Both the rotational drag equation for torque and video microscopy of the particle's shape anisotropy as a marker for particle angle were used by Galajda & Ormos (2003) to obtain an empirical relationship between torque and the particle angle.

Bishop *et al.* (2003) employed a different method to measure the torque imparted to the particle by decomposing the exit beam into its left- and right-circular polarised components using a quarter-wave plate and a polarising beam-splitter. Torque is usually defined as the rate of change in angular momentum, $\tau = dL/dt$. A change in variable yields $\tau = (dL/dN_p) \times (dN_p/dt)$ which allows one to calculate torque simply from the change in the angular momentum per photon dL/dN_p and photon-flux dN_p/dt. From the quantum theory of light, left- and right-circularly polarised photons carry spin angular momentum of $+\hbar$ and $-\hbar$ respectively where $\hbar = h/2\pi$ and h is Planck's constant. Meanwhile, the photon-flux can be determined from the total intensity of the transmitted beam.

Shape anisotropy of the microscopic transparent particles was widely exploited in these early studies as the particle angle could be determined using video microscopy

of this shape anisotropy. The use of birefringent particles soon took precedence, motivated strongly by the development of an active angular optical trap by La Porta & Wang (2004). The authors were able to obtain a direct relationship between torque and a parameter unique to the orientation of the birefringent particle. The theory behind this relationship can be formulated as follows:

- An electric polarisation $\mathbf{P}$ will be induced in a dielectric particle subject to an external field $\mathbf{E}$ as follows:

$$\mathbf{P} = \boldsymbol{\chi} \cdot \mathbf{E} \tag{2.1}$$

  where $\boldsymbol{\chi}$ is the electric susceptibility tensor.

- For a birefringent particle, this susceptibility tensor can be diagonalised as follows

$$\mathbf{P} = \chi_x E_x \hat{\mathbf{x}} + \chi_y E_y \hat{\mathbf{y}} + \chi_z E_z \hat{\mathbf{z}} \tag{2.2}$$

  where the unit vectors denoted by $\hat{\mathbf{x}}$, $\hat{\mathbf{y}}$ and $\hat{\mathbf{z}}$, coincide with the principal axes of the crystal. The corresponding electrical susceptibilities are given by χ_x, χ_y and χ_z. Uniaxial birefringent particles such as quartz or calcite have two equal susceptibility components called the ordinary axes (χ_o) and one different component, the extraordinary axis (χ_e). The extraordinary axis is also known as the optic axis of the crystal and light travelling in the direction of this axis will experience no birefringence.

- The equation above can be further simplified if the extraordinary axis is more easily polarisable than the ordinary axis, as found in quartz. The extraordinary axis will align with the direction of the electric field and so a linearly polarised trap can be used to align this particle. An actively rotating linearly polarised

trap can thus deliver torque to the quartz particle. This torque is given by

$$\boldsymbol{\tau}_{\text{optical}} = \int \mathbf{E} \times \mathbf{P}\, d^3x = -\tau_o \sin(2(\theta_e - \theta_o))\hat{\mathbf{z}} \tag{2.3}$$

where θ_e and θ_o are the angles the extraordinary axis χ_e and the electric field $\mathbf{E}$ make with the x-axis respectively. τ_o is the maximum permissible torque and can be explicitly expressed as (Pedaci *et al.*, 2011),

$$\tau_o = \frac{S\epsilon}{2\pi\nu} E_o^2 \sin(kL\Delta n)\ . \tag{2.4}$$

where S is the particle cross-sectional area, ϵ is the electric permittivity, ν is the optical frequency, E_o is the amplitude of the electric field, k is the wave vector, L is the length of the particle and $\Delta n = n_e - n_o$ is the amount of birefringence in the material which is the difference between the refractive index in the extraordinary axis (n_e) and that in the ordinary axis (n_o). For quartz, $\Delta n_{\text{quartz}} = 0.009$.

The two equations given above assume that both the extraordinary axis and the polarisation of the input beam are on the same plane, resulting in one component in $\hat{\mathbf{z}}$. If the extraordinary axis is not in the same plane as the polarisation, other components will contribute to the torque and the angular dependence of the torque delivered may not follow $\sin(2(\theta_e - \theta))$. As such, it is important to fabricate these quartz particles such that the optic axis of the cylinder is in the same plane as the input polarisation when the particle is optically trapped.

These traps are known as active angular optical traps because they involve actively rotating the linear polarisation of the input beam. Active rotation of the input polarisation was first achieved by means of using acousto-optic modulators (AOMs) (La Porta & Wang, 2004). These devices have recently been replaced by electro-optic modulators (EOMs) for better performance (Gutierrez-Medina *et al.*,

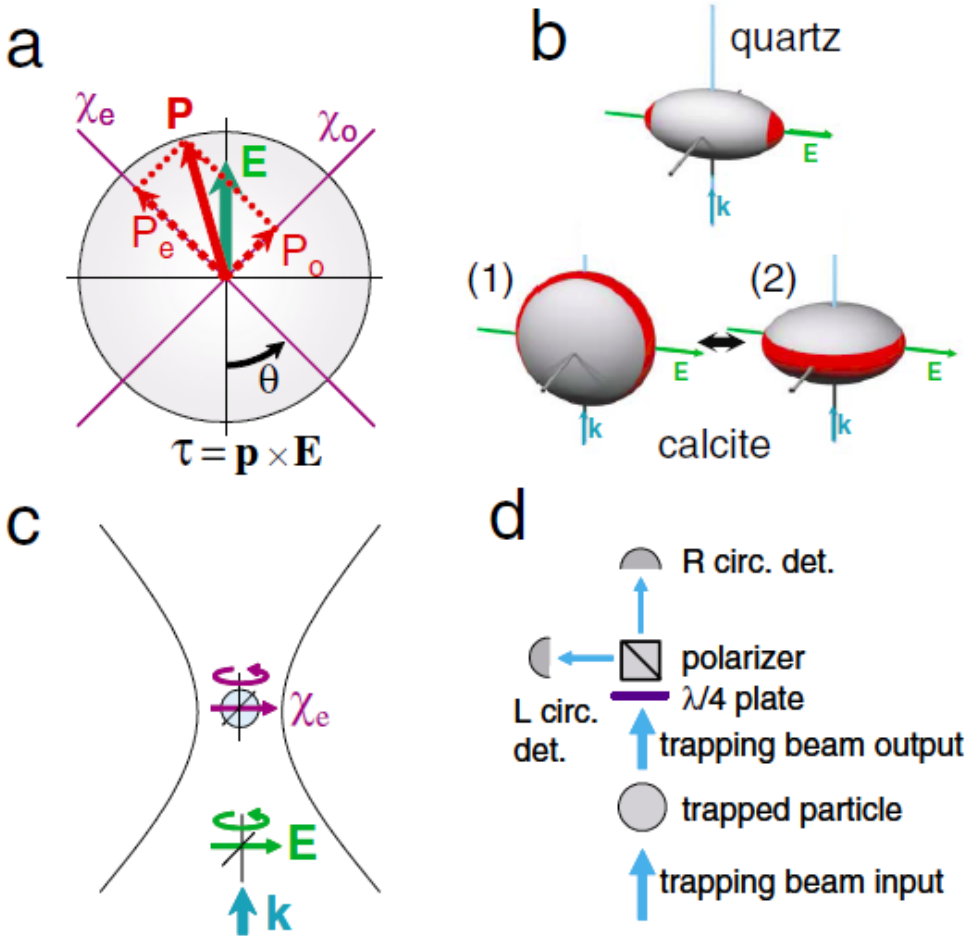

Figure 2.2. Principles behind active angular optical trapping **(a)** A polarisation vector **P** is induced in a dielectric particle by an external electric field **E**. θ shown here is the same as $(\theta_e - \theta)$ found in Equation (2.3). **(b)** Representation of the electric susceptibility ellipsoid of quartz and calcite where the maximum susceptibility is marked in red. This sub-figure motivates the use of quartz as the red regions will naturally align with the electric field. (1) and (2) shows the possible final configurations of a calcite particle with respect to the electric field. Case (1) would require further constraint usually in the form of some shape anisotropy while the light field experiences no birefringence in case (2). As such, it is more tricky to use calcite in an active angular optical trap. **(c)** Illustration of the particle's alignment with the trap's polarisation. **(d)** Schematic of the apparatus to measure torque using the difference in intensities of the left- and right-circularly polarised components of the transmitted beam. This apparatus is the same as that previously developed in Bishop *et al.* (2003). The figure above was taken from La Porta & Wang (2004).

2010; Pedaci *et al.*, 2011). Active feedback on the input polarization angle can be implemented to maintain constant torque delivered to the trapped particle.

Equation (2.3) predicts that the maximum torque is attained when the angle between the extraordinary axis and the electric field is equal to 45°, after which the particle starts to slip as the torque is insufficient to overcome rotational drag. The critical frequency at which this takes place is given by $f_c = \tau_o/\gamma$ and this quantity can be raised by increasing the power of the input beam.

Shape effects have not been taken into account but are known to play a strong role in how the particle is trapped. For instance, the long axis of a cylindrical particle will align in the direction of the input trapping beam which will help confine two rotational degrees of freedom (Deufel *et al.*, 2007). The ability to nano-fabricate quartz particles of varying length in which the optic axis is perpendicular to the long axis of the cylinder has been made possible using optical lithography (Deufel *et al.*, 2007; Gutierrez-Medina *et al.*, 2010) and electron-beam lithography (Huang *et al.*, 2011). Furthermore, this cylindrical particles can be end-functionalised for attachment to biological molecules. As such, these cylindrical quartz particles have become suitable handles for the application of optical torque at the single-molecule level.

These active angular optical traps can operate in a "passive" mode whereby an averaged constant torque is achieved from rotating the polarisation at a rate much faster than the particle is able to respond (Inman *et al.*, 2010). This results in a constant torque imparted to the particle, a similar observation to that seen using the electrorotation method.

Passive angular optical traps operate differently in that circularly polarised light is preferred and modulation of the beam intensity is used to control the amount of torque delivered (Friese *et al.*, 1998; Bishop *et al.*, 2003, 2004; Funk *et al.*, 2009). Microscopic particles having higher birefringence such as calcite ($\Delta n_{\text{calcite}} = -0.172$)

and vaterite ($\Delta n_{\text{vaterite}} = 0.100$) are preferred handles in these traps. The reasons for using circularly polarised light with particles having high birefringence is as follows.

When the incident light is linearly polarised, the magnitude of torque generated per photon is given by (Nieminen *et al.*, 2001)

$$\tau_{\text{linear}} = \sin(2(\theta_e - \theta)) \sin(kL\Delta n)\hbar \tag{2.5}$$

while the maximum torque generated per photon if the input beam is right-circularly polarised is given by

$$\tau_{\text{right}} = (1 - \cos(kL\Delta n))\hbar \, . \tag{2.6}$$

A plot of the two equations is shown in Figure 2.3 which shows that the maximum torque permissible is higher for right-circularly polarised light than linearly polarised light. The maximum torque is achieved for linearly polarised light if the particle behaves like a quarter-wave plate while the maximum torque is achieved for circularly polarised light if the particle behaves like a half-wave plate. The use of materials with high birefringence will result in smaller particles with less rotational drag.

There is plenty of room at the micron-scale to fabricate highly birefringent particles which behave close to quarter-wave plates and half-wave plates. This is because infra-red lasers having of 1.064 μm are often the choice of lasers used for trapping due to the size of its beam waist. Also, lasers operating at this wavelength are known to cause minimal photodamage to biological specimens (Neuman *et al.*, 1999).

Vaterite has become the main choice of particles for passive angular optical traps because of the ease in fabricating and functionalising them compared to calcite (Vogel *et al.*, 2009; Parkin *et al.*, 2009). In addition, its positive birefringence means that it can be aligned in the trap easily if the rotational symmetry of the input beam is broken, for instance by using an elliptical polarisation. Nonetheless, there is still promise for calcite if there is a method to fabricate cylindrical particles with one of

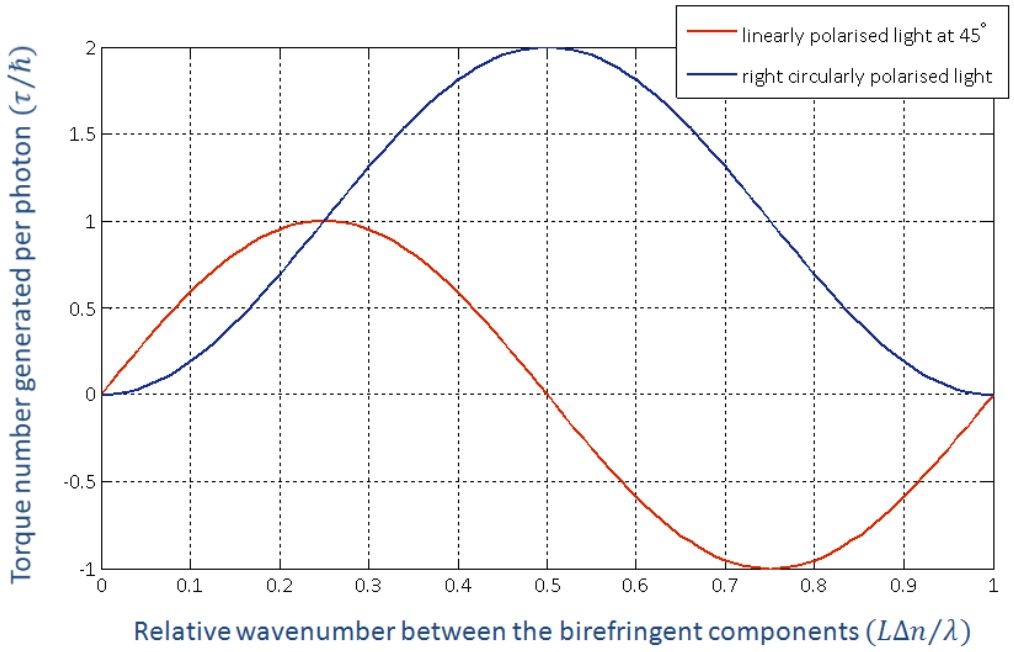

Figure 2.3. Torque number generated per photon for incident beam having (i) linearly polarisation at 45° with respect to the extraordinary axis and (ii) right-circularly polarisation. λ is the wavelength of the incident beam. It can be observed that the maximum torque that can be generated per photon using circularly polarised light is $2\hbar$ as compared to $\hbar$ for linearly polarised light. Linearly polarised light consists two equal components of left- and right-circularly polarised light. As such, only half of its original intensity is converted to one of the two circular polarised after traversing through a quarter-wave plate. The maximum torque attainable using a 1 mW laser having a wavelength of 1064 nm is 1130 pNnm. This is on the same order of magnitude at which the bacterial flagellar motor can be stalled which is about 1260 pNnm measured in Reid *et al.* (2006).

the more easily polarisable axes normal to the long axis of the cylinder.

Recently, rutile particles (TiO_2) have become candidate handles for such traps. These particles have a high refractive index ($n_e = 2.909$ and $n_o = 2.613$) and a birefringence of 0.296. Due to their relatively high refractive index compared to water, rutile particles scatter very strongly making them difficult to trap. A counter-propagating dual trap has been suggested to trap these particles.

It is also possible to exploit the overall profile of a beam's intensity and polarisation to exert torque on microscopic objects whereby the source of angular momentum is often called orbital angular momentum (Allen *et al.*, 1992). This method of exerting torque is not considered as the cross-sectional area of the beam profile is often a lot larger than the cross-sectional area of trapped optical torque handles I intend to use.

2.2.2 Assay design

I explored several designs for assays proposed by Dr Richard Berry for the application of optical torque on the bacterial flagellar motor. We recognised that the rotational axis of the optical handle must coincide with the rotational axis of the flagellar motor in order to minimise possible unexpected rotational couplings between the handle and the motor.

In principle, the location and the rotational axis of the motor can be determined using a polystyrene bead assay. The bead assay used is a major improvement from that developed previously (Ryu *et al.*, 2000; Sowa *et al.*, 2005; Reid *et al.*, 2006). This is because hydrophobic filaments (sticky filaments) required for attachment with the polystyrene bead are expressed from the genome rather than plasmids. Various regions in the *FliC* gene have been truncated so that hydrophobic regions are exposed when the filaments are formed. These filaments have a high affinity with microscopic plain polystyrene beads of different diameters (Polysciences) and I was able to obtain high yields of rotating bead assay using this strain.

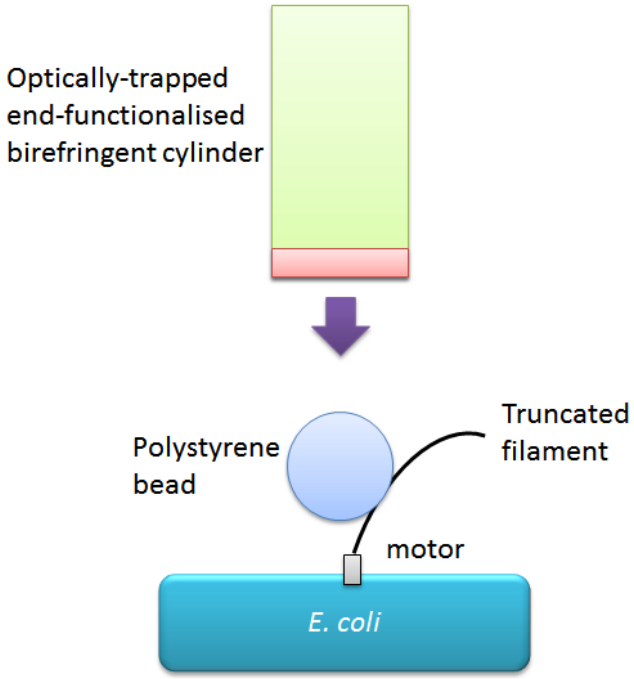

Figure 2.4. Schematic of an assay for application of optical torque. Optically-trapped birefringent cylinders are aligned with the rotational axis of the motor, determined using a bead assay. Appropriate end-functionalisation must be selected for attachment to the bead.

An optically-trapped birefringent particle with hydrophobic ends can be lined up with the rotational centre of the bead assay and brought close to the assay for attachment. Cylindrical-shape particles were chosen due to the ease of aligning them in an optical trap. A schematic of this assay is shown in Figure 2.4.

In an attempt to find out whether rutile particles can be suitable candidates for this assay, I carried out a numerical simulation to determine how much laser power is required to generate enough torque in which the bacterial flagellar motor could be stalled and spun at 350 Hz using one of these particles. The optical torque imparted to the rutile particle must be able to overcome the rotational drag of both a polystyrene bead having a diameter of 1 μm.

In this simulation, the shape of particle was assumed to be cylindrical where the optic axis is perpendicular to the long axis of the cylinder. The incident beam was assumed to be right-circularly polarised and had a wavelength of 1064 nm. The

torque imparted to the particle per unit area was determined by multiplying the torque number generated per photon using Equation 2.6 and the photon-flux. The photon-flux was obtained by dividing the intensity of the beam at a given point by the energy of each photon. A two-dimensional Gaussian function was assumed for the intensity profile of the incident beam and the width of this function, equivalent to the beam's waist, was assumed to be 1000 nm. The optical torque imparted to the particle was then obtained by integrating the torque imparted to the particle per unit area over the cross-sectional area of the particle. The total drag of the particle was the sum of the rotational drag due to the rutile cylinder and the 1 μm polystyrene bead. The stall torque was assumed to be 1260 pNnm (Reid *et al.*, 2006).

The results of this simulation for cylinders having various diameters and lengths are shown in Figure 2.5. The colour scale indicates the intensity required at the centre of a right-circularly polarised Gaussian beam required to spin this particle attached to a 1 μm polystyrene bead at 350 Hz and to overcome stall torque of the bacterial flagellar motor. The results obtained showed that a cylindrical rutile particle having a diameter of 0.5 μm and length 1 μm attached to the polystyrene bead will only require a few mW of beam power to spin at 350 Hz and to stall the motor.

Due to the lack of available rutile cylinders, I carried out preliminary experiments to design the optical torque assay using cylindrical quartz particles obtained from Nynke Dekker Lab. They are able to etch cylinders from crystal wafers by means of electron beam lithography and apply a hydrophobic coating to the ends of the cylinder Huang *et al.* (2011). Electron-beam lithography has added advantages over conventional optical lithography in that smaller features such as protrusions can be etched as well as being able to achieve high uniformity in the volume and cylinder shape from a given wafer. Scanning electron microscopy (SEM) images of quartz particles that can be fabricated using their facilities at TU Delft are shown in Figure 2.6. This figure shows that these particles are tapered at one end, usually at the

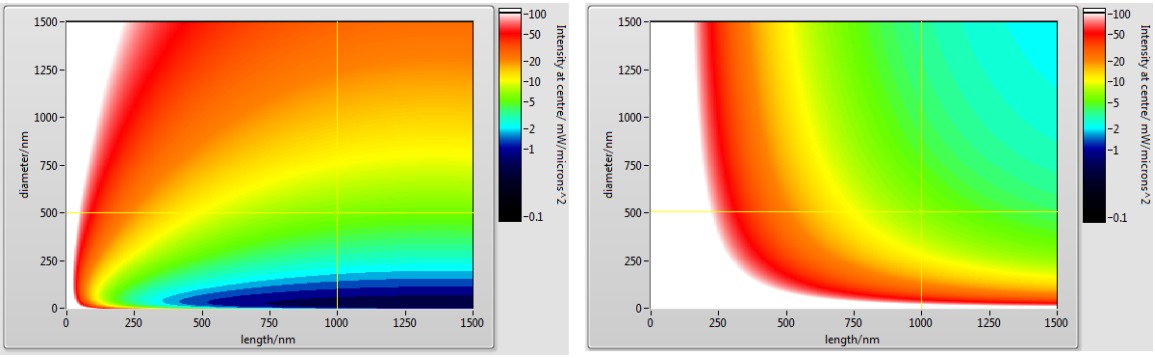

Figure 2.5. Intensity required at the centre of a right-circularly polarised Gaussian beam (mW/μm^2) to **(left)** rotate a rutile cylinder attached to a 1 μm polystyrene bead at 350 Hz, and **(right)** generate enough torque to stall the motor (1260 pNnm) for different cylinder lengths and diameters. The cursor indicates that a few mW of beam power is sufficient to stall the motor as well as to stall the bacterial flagellar motor and to rotate the cylinder having a diameter of 0.5 μm and length 1 μm attached to a bead at a speed of 350 Hz.

end where the particle is functionalised.

Experiments to trap and attach these tapered cylindrical particles were carried out using an inverted optical trapping microscope inherited from Rowe (2005) in which I fully reassembled and realigned the optical components on this set-up. I also installed a digital camera (GC1280, Prosilica) and wrote custom programs in LabVIEW to control the acquisition properties of this camera.

Video microscopy of optical trapping experiments using these tapered cylindrical particles revealed that these cylinders prefer to trap with the tapered end facing away from the input beam. This can be observed in a series of images shown in Figure 2.7. This was a useful observation as it meant that there was full control over the cylinder end in the trap.

Even with this level of control I was not able to reliably stick plain polystyrene beads to hydrophobic-coated cylindrical quartz particles. The use of different salt concentrations to shield possible ionic repulsions did not resolve this issue. To date, I have only observed two instances where these cylinders were stuck to a polystyrene bead.

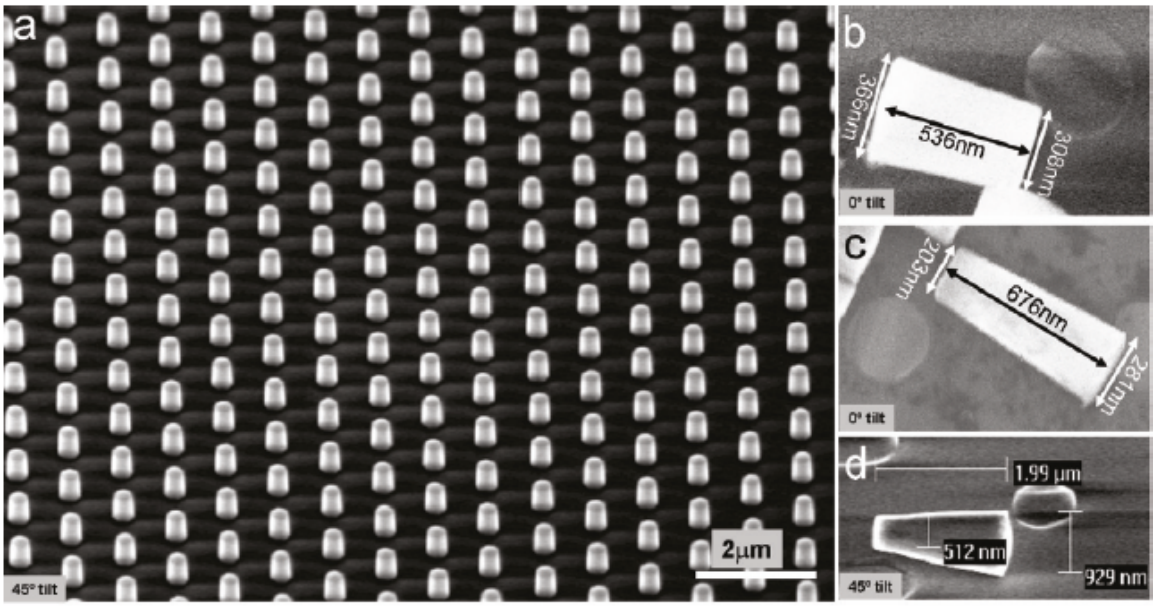

Figure 2.6. SEM images of quartz cylinders fabricated at TU Delft. **(a)** Cylinders arranged on the wafer. **(b)**, **(c)**, and **(d)** Cylinders having different diameters, aspect ratios and conical shapes. The figure above is taken from Huang *et al.* (2011).

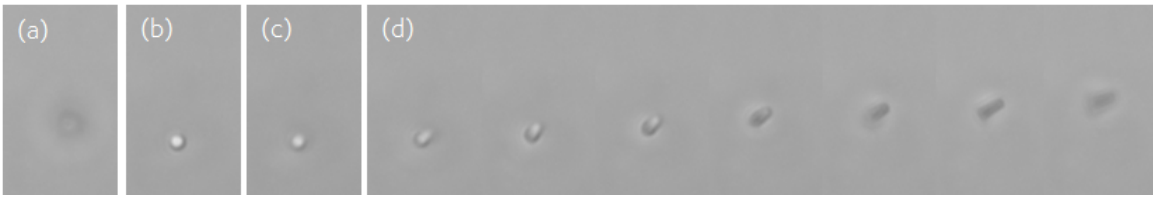

Figure 2.7. Video microscopy images of optical traping experiments using hydrophobic tapered cylindrical quartz particles fabricated at TU Delft. These images were taken on an inverted bright-field microscope. The diameter of this cylindrical particle was about 800 nm at the tapered end. **(a)** A quartz cylinder just before entering the trap. Objects that look darker denote that the object is just upstream from the focal point, i.e. in the direction towards the microscope objective. **(b)** The particle was trapped and had a whitish appearance. This is associated with the particle being trapped just downstream from the focal point of the beam, i.e. in the direction away from the microscope objective. **(c)** The image of the particle just when the trapped is turned off. **(d)** Time-course series of images taken at intervals of 0.2 s in which the first image is taken 1/30 s after the image shown in (c). The time-course series show that the particle slowly diffuses towards the objective and the tapered end is clearly the furthest end of the particle, away from the objective.

The preliminary experiments carried out showed that hydrophobic attachment is not a reliable method for attaching these hydrophobic quartz particles to polystyrene bead assays. An alternative method using streptavidin-biotin attachment is strongly encouraged in future experiments. One possible construct for this assay will be to use a bead assay in which streptavidin-coated polystyrene beads are attached to biotinylated filaments. There are bacterial strains capable of endogenously expressing biotinylated hooks (Brown *et al.*, 2012). The use of such strains will can help minimise the drag of the overall assay due to the direct attachment to the hook.

2.3 Magnetic tweezers

2.3.1 Overview of existing methods

The use of magnetic tweezers is the most well-known method to apply torque to biological molecules at the single-molecule level. The first demonstration of magnetic tweezers used to study the biophysics of biological molecules was carried out by Strick *et al.* (1996). The authors stuck a magnetic bead to the DNA molecule fixed to the coverslip and the bead was rotated using a pair of permanent magnets oriented transverse to the DNA molecule. Using this technique, the authors were able to investigate the supercoiling elasticity of single-stranded DNA molecules.

Magnetic tweezers fall generally into three categories: tweezers that make use of permanent magnets, pairs of Helmholtz coils and electromagnets. An illustration of the different types of magnetic tweezers that have been reported is shown in Figure 2.8.

The design of magnetic tweezers that employ permanent magnets has evolved dramatically over many years. For instance, permanent magnets are now orientated axially relative to the microscope stage in order to minimise torsional stiffness (Celedon *et al.*, 2009, 2010). Various ingenious tricks have been implemented in order to align the torque handles while measuring torque and rotation simultaneously (Lipfert

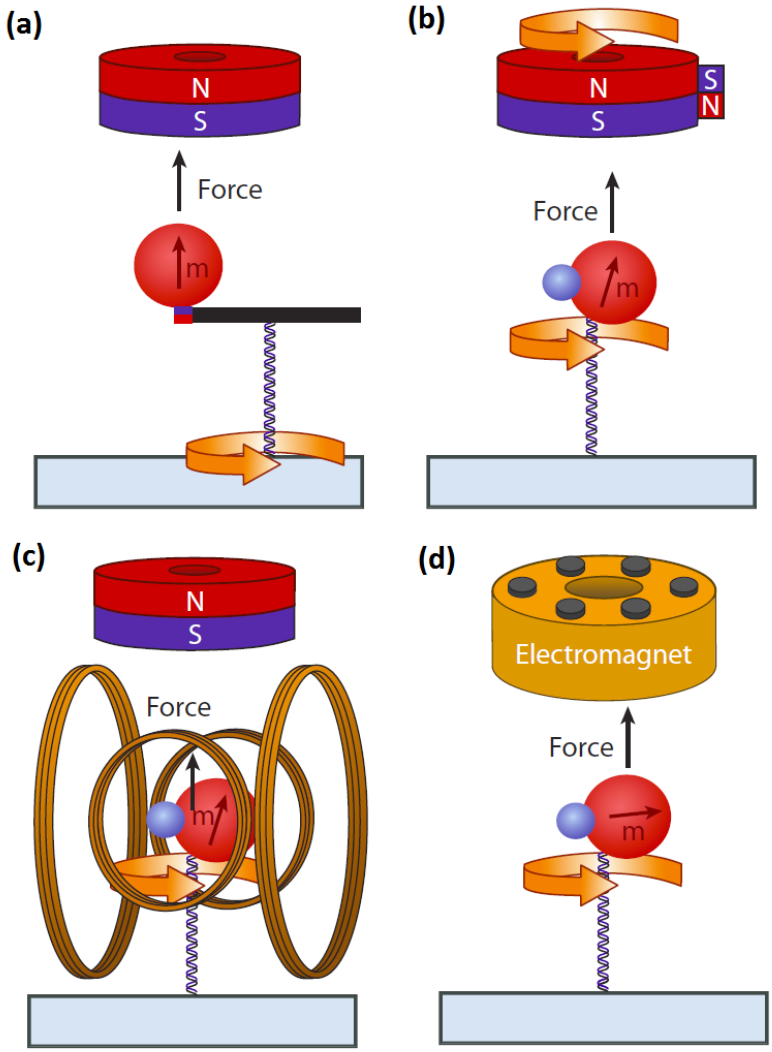

Figure 2.8. Experimental configurations for magnetic tweezers used for single-molecule experiments (figure above is taken from Forth *et al.* (2013)). **(a)** Set-up by Celedon *et al.* (2009) consisting of a magnetic bead and a nanorod torque arm to align one end of the double-stranded DNA tether. The permanent magnets are fixed and twist is introduced by rotating the stage. **(b)** Lipfert *et al.* (2010) added an additional side magnet to introduce a small horizontal perturbation to the vertical magnetic field created by the main cylindrical magnet. This produces an angular trap with low-stiffness to align the bead. The smaller bead (coloured in blue) is used an angular marker. **(c)** Electromagnetic torque tweezers developed by Janssen *et al.* (2012) which uses two pairs of Helmholtz coils to control the horizontal magnetic field. **(d)** Tweezers set-up that make use of a six-pole electromagnet developed by Gosse & Croquette (2002). A rapidly rotating horizontal magnetic field of varying intensity can be generated to produce either a constant torque or a magnetic angular trap of tunable stiffness.

et al., 2010, 2011; Kauert *et al.*, 2011; Lebel *et al.*, 2014). Pairs of Helmholtz coils configured correctly can also be introduced in order to achieve full control of the transverse magnetic field (Janssen *et al.*, 2012).

Magnetic tweezers that make use of electromagnets have been previously used to study ATP synthesis of F1-ATPases (Rondelez *et al.*, 2005; Adachi *et al.*, 2007). The tweezers were only used to rotate the torque handles in these experiments and simultaneous torque measurements were not reported. Attempts to obtain measurements of the torque using such tweezers were carried out by Mosconi *et al.* (2011).

Existing methods to determine torque using the above tweezers follow the same principle. Torque is determined by multiplying the calibrated angular trap stiffness, and the angle between the magnetic particle and the magnetic field (Normanno *et al.*, 2004). Such measurement techniques assume that the angle between the particle and the field is small and the angular stiffness of such tweezers, usually on the order of 50 pNnm/rad (Janssen *et al.*, 2012), is suitable for twisting and studying torque effects on DNA strands.

The maximum magnetic field reported from magnetic tweezers that employ pairs of Helmholtz coils is 16 mT (Janssen *et al.*, 2012). This is insufficient to stall the bacterial flagellar motor in stalling experiments which I carried out in Tipping *et al.* (2013a). The experiments carried out revealed that at least 20 mT was required to stall the motor. Magnetic tweezers that employ rotating permanent magnets were also considered. However, the difficulty with rotating them at high speeds and the potential huge vibrational noises they may introduced led me to consider the option of using electromagnets.

2.3.2 Principles behind magnetic torque

The magnetic torque generated as a result of the interaction of a magnetic particle having magnetic dipole moment $\boldsymbol{\mu}$ and the magnetic field $\mathbf{B}$ is given by

$$\boldsymbol{\tau}_{magnetic} = \boldsymbol{\mu} \times \mathbf{B}, \tag{2.7}$$

an equation similar in form to Equation (2.3) except that the volume integral is now embedded inside $\boldsymbol{\mu}$. Particles with permanent dipoles are understood to obey a sin $\Delta\theta$ behaviour when following a rotating magnetic field where $\Delta\theta$ is angle between the dipole moment and the magnetic field. Such particles follow the rotating field at one given angle and the maximum torque is attained when $\Delta\theta = 90°$.

Superparamagnetic beads are the main choice of torque handles in magnetic tweezers and if they were perfectly symmetric, the magnetisation would tightly follow the magnetic field. As a result, no torque would be exerted on the bead. However, this is not the case as superparamagnetic beads consist of aggregates of very small (5 nm to 10 nm) crystals of iron oxide with random orientation (Normanno *et al.*, 2004; Klaue & Seidel, 2009). These particles thus contain some degree of crystalline anisotropy and shape anisotropy, which contribute to the small inhomogeneity in the magnetic susceptibility. There is currently no further knowledge about the microscopic details of these beads but Mosconi *et al.* (2011) claims that these beads are positively uniaxial and the anisotropy associated with the susceptibility of these beads is on the order of a few percent in the easy direction. They also noted that the bead magnetisation will increase slightly when the magnetic field is aligned with the bead's easy axis.

From the observations above, the physics behind the rotation of such anisotropic particles in the presence of a rotating magnetic-field is thus similar to that of birefringent particles in a rotating linearly polarised electric field. The magnetic torque

delivered to superparamagnetic beads is (Mosconi *et al.*, 2011)

$$\tau_{\text{magnetic}} = \frac{\alpha M_{\text{sat}} B}{2} \sin(2\Delta\theta) \tag{2.8}$$

where α is the anisotropy of the beads, M_{sat} is the saturating magnetisation of the superparamagnetic bead, B is the magnetic field strength and $\Delta\theta$ is the angle between the bead's easy axis and the magnetic field angle. Superparamagnetic beads thus obey a $\sin(2\Delta\theta)$ behaviour when following a rotating magnetic field. Such beads can follow the rotating field at two angles and the maximum torque is attained when $\Delta\theta = 45°$.

The preferred superparamagnetic bead for use in most magnetic tweezers experiment is the Dynabeads MyOne which has a diameter of 1.0 μm. The magnetisation per unit volume of these beads is equal to 43.3 kA/m and the saturating magnetic field for these beads is 12 mT (Lipfert *et al.*, 2009). For these beads, $M_{\text{sat}} = 2.27 \times 10^{-23}$ Am^2.

I calculated the maximum angular frequency at which the particle can rotate for a given field strength using the equation

$$\frac{\alpha M_{\text{sat}} B}{2} = \gamma\omega \tag{2.9}$$

where $\gamma = 8\pi\eta r^3$ is the rotational drag of the spherical superparamagnetic bead and ω is the angular frequency. Assuming the parameters above, a magnetic field strength of 60 mT and an anisotropy of 1% for the beads, the maximum angular frequency is about 2166 rad/s which is equivalent to 345 revolutions per second.

From the back-of-the-envelope calculation above, 60 mT of magnetic field should in principle allow me to spin the beads fast enough to study the zero-torque speed behaviour of wild-type bacterial strains. This value is recognised to be very sensitive to any changes in the bead's anisotropy of which there is no experimental estimate. Nonetheless, the estimate above provides a useful ballpark figure of the magnetic field

strength required to rotate the beads at this speed. As such, I went on to explore the possibility of building electromagnets capable of generating rotating magnetic fields having field strengths near this order of magnitude.

Chapter 3

Development of a System to Deliver Magnetic Torque

The potential ability of magnetic tweezers that employ electromagnets to rotate superparamagnetic beads at high speeds has led me to consider them as the main candidates to deliver external torque to the bacterial flagellar motor. Magnetic tweezers that employ permanent magnets and pairs of Helmholtz coils are not suitable for this experiment. Tweezers that employ permanent magnets will introduce a huge amount of physical vibrations when rotated too quickly where ones that employ pairs of Helmholtz coils do generate sufficient magnetic field strengths.

In this chapter, I will provide details of the development of a system to deliver magnetic torque to the motor. The development of this system can be broken down into two stages. The first stage involves developing an assay in which a magnetic bead is attached to the flagellar motor. The second stage involves developing electromagnets capable of generating rotating magnetic field at sufficiently high field strengths. Back-of-the-envelope calculations revealed that the minimum field strength required is on the order of tens of mT.

In the first section of this chapter, I will describe the development of a magnetic

bead assay. Following this, I will describe the optical technique deployed to determine the rotational speed and the angle of the bead orientation. The following section describes the development and operating principles behind the electromagnets. A three-pole electromagnet was developed to generate fast-rotating magnetic fields with large enough field intensities. In the final section, I will describe the characterisation of the amplifier driving the current through each coil of the electromagnet.

3.1 The magnetic bead assay

(***Declaration of contributions for this section:*** *Experiments to develop a magnetic bead assay by attaching hydrophobic and COOH-coated superparamagnetic beads to sticky filaments were carried out in collaboration with Dr Kousuke Nogawa from the University of Nagoya when he was a visiting academic at Berry Lab between September 2012 and February 2013. One of the two variants of the magnetic bead-filament assay was developed in collaboration with Dr Kousuke Nogawa during his visit using a gift strain from Berg Lab. I designed and made another variant of the magnetic bead-filament assay for use in fluorescent stator experiments using a strain developed by both Dr Nicolas Delalez and Dr Murray Tipping from Armitage Lab. Finally, I designed and made the magnetic bead-hook assay using a strain which was developed by Dr Mostyn Brown from Armitage Lab.*)

The bead assay, first developed by Ryu *et al.* (2000) has been extensively used to study the torque-generating mechanism of the bacterial flagellar motor. Hydrophobic polystyrene beads of various diameters ranging from 200 nm until to 1 μm are attached to filaments made "sticky" by exposing hydrophobic regions. The drag of this assay was later reduced using gold beads whose diameters are less than 100 nm attached directly to hook using antibodies (Yuan & Berg, 2008).

Two approaches to attach superparamagnetic beads to motors were explored. The

Bead Name	Diameter	Manufacturer
Dynabeads MyOne COOH	1.0 μm	Invitrogen
ProMag 1 Series COOH	0.97 μm	Bang Laboratories
SiMAG-Methyl (C1)	1.0 μm	Chemicell
SiMAG-Propyl (C3)	1.0 μm	Chemicell
SiMAG-Octyl (C8)	1.0 μm	Chemicell
SiMAG-Octadecyl (C18)	1.0 μm	Chemicell
Plain magnetic polystyrene beads	1.0 μm	Sigma-Aldrich

Table 3.1. List of hydrophobic and COOH-coated superparamagnetic polystyrene beads used in experiments to investigate whether they would attach hydrophobically to sticky filaments expressed by bacterial cells MT03. SiMAG beads are known to be hydrophobic and the hydrophobicity of these beads increase with increasing number of Carbon atoms. None of the beads listed above attached successfully to sticky filaments.

first approach involved establishing a method to attach these beads hydrophobically to sticky filaments while the second approach involved establishing a method based on streptavidin-biotin attachment.

For the first approach, Dr Kousuke and I investigated a range of hydrophobic and COOH-coated superparamagnetic polystyrene beads. We tried to attach them to sticky filaments expressed by bacterial cells MT03 under various salt conditions to minimise possible ionic repulsions. The sticky filaments are known to have a high affinity with hydrophobic plain polystyrene beads. The beads tried are listed in Table 3.1 and none of them attached successfully to sticky filaments.

Successful attempts to attach superparamagnetic beads to flagellar motors were achieved using the second approach. Two versions of this magnetic bead assay were developed and are shown schematically in Figure 3.1.

The first version of the magnetic bead assay involves directly attaching micron-sized streptavidin-coated superparamagnetic polystyrene beads onto hooks. In order to achieve this, bacterial cells (strain name: MTB32) capable of expressing biotiny-

Figure 3.1. Schematic diagram showing two versions of the magnetic bead assay developed using streptavidin-biotion attachment. **(a)** The first version involves attaching a streptavidin-coated superparamagnetic polystyrene bead onto the biotinylated hook while **(b)** the second assay involves attaching the streptavidin-coated bead onto the biotinylated truncated filament. The *E. coli* cells are permanently immobilised on the glass coverslip using poly-L-lysine.

lated hooks endogenously were used (Brown *et al.*, 2012). These cells do not express filaments and are able to switch. This version of the magnetic bead assay is called the magnetic bead-hook assay.

The second version of the magnetic bead assay involves attaching superparamagnetic beads onto biotinylated filaments and is called the magnetic bead-filament assay. Two variants of this bead assay were developed. The first variant, designed and constructed in collaboration with Dr Kousuke Nogawa, makes use of the bacterial strain HCB1737, a gift strain from Berg Lab, which carried a single-site cysteine mutation (S219C) in the filament or *FliC* gene (Turner *et al.*, 2012). The cysteine residues expressed on the filaments can be easily biotinylated using maleimide-PEG2-biotin (Thermo Scientific). Apart from this single-site mutation in the filament gene, this strain shares similar phenotypes with the wild-type strain. The other variant involves the use of the bacterial strain JPA808, developed by both Dr Nicolas Delalez and Dr Murray Tipping. This strain was derived from HCB1737 and is able to express GFP-tagged stators.

Both MTB32 and HCB1737 are derivatives of the *E. coli* K-12 strain. Their

genealogy can be traced all the way back to a wild-type strain, AW405, developed by Armstrong *et al.* (1967). HCB1737 was derived directly from AW405 (Turner *et al.*, 2012) whereas MTB32 follows a longer genealogy path. MTB32 was derived from RP437 (Brown *et al.*, 2012) which was a derivative of RP461 (Parkinson, 1978). RP461 was derived from AW574 (Parkinson, 1976) and AW574 was derived from AW405 (Larsen *et al.*, 1974b), the parent strain of HCB1737.

Frozen stocks of each of the two strains above were prepared and kept in a chest freezer at $-80°$C. 100 μl of each strain was grown in 5 ml of tryptone broth (1% Bacto-tryptone, BD; 0.5% NaCl) without antibiotics at 30°C until an optical density between 0.5 and 0.7 was attained. HCB1737 cells take about 4 hours while MTB32 take about 5 hours to reach this optical density.

Preparation of MTB32 cells for use in a tunnel slide was more straightfoward than HCB1737 due to the lack of filaments. 1 ml of MTB32 cells was spun down and washed with a motility buffer (10 mM potassium phosphate, 0.1 mM EDTA, pH 7.0) twice before diluting them in 200 μl of the same buffer.

Preparation of HCB1737 was more complicated as these cells had to pass through a shearing device, usually about 50 times, to truncate the filaments, before the biotinylating step. The shearing device forces 1 ml of the cell suspension through two syringes with 26-gauge needles connected by a piece of polyethylene tubing having an inner diameter of 0.58 mm. The turbulent flow which occurs inside the needle is sufficient to shear the flagella at a random point along the filament (Rowe, 2005). The cells were washed with motility buffer twice and diluted in 20 μl of the same buffer. Following this, 10 μl containing 20 mM of maleimide-PEG2-biotin (Thermo Scientific) diluted in motility buffer was added to the cells and allowed to mix for 1 min. Four washing steps were carried out consequently to remove any excess maleimide-PEG2-biotin before diluting the cells in 200 μl of the motility medium.

A tunnel slide was set up by sandwiching two glass coverslips together separated

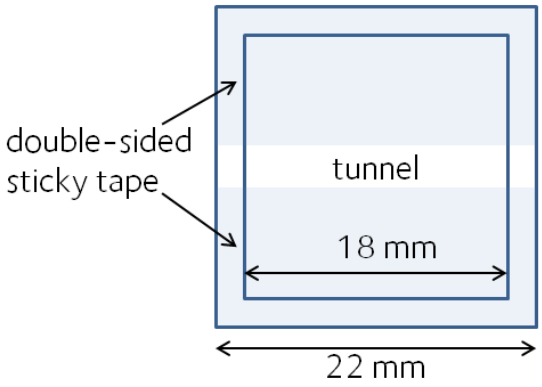

Figure 3.2. Schematic of the tunnel slide. The double-sided sticky tape is shaded in light blue and the spacing between the tape and the glass coverslips form the tunnel through which cells and various media can flow through.

by double-sided sticky tapes as shown in Figure 3.2. One of the coverslips is usually bigger (22 mm × 22 mm) than the other (18 mm × 18 mm) for ease of flushing liquid volumes into the tunnel slide.

Poly-L-lysine (0.1% w/v in H_2O, Sigma-Aldrich), a positively-charged chain of amino acids sticky to cell membranes, is flushed into the slide for 20 s and is rinsed using motility buffer. Cells diluted in the motility medium as described previously are then flushed in and allowed to sediment onto the coverslip between eight and ten minutes. The cells are incubated in the tunnel slide with the smaller glass coverslip on the bottom. Unstuck cells are rinsed out before the appropriate beads are added and allowed to sediment to the coverslip for at least two minutes. The period in which the beads were incubated with the cells was carried out in the middle of a pair of Helmholtz Coils (TEL 2502, TEL-Atomic). The input current used for each coil is 1.5 A which gave rise to a magnetic field of strength 3 mT in the middle of the coils measured using a Gaussmeter (GM04, Hirst). The magnetic field generated by the coils would help preferentially align the easy axis of the beads so that they were in-plane with the glass coverslips.

Finally, unstuck beads were rinsed out using the motility medium. Superparam-

Strain	Bead Name	Diameter	Manufacturer
HCB1737	Dynabeads MyOne Streptavidin T1	1.0 μm	Invitrogen
	Dynabeads MyOne Streptavidin C1	1.0 μm	Invitrogen
	ProMag 1 Series Streptavidin	0.97 μm	Bang Laboratories
	PS-MAG-SA	0.540 μm	Microparticles GmbH
MTB32	Dynabeads MyOne Streptavidin T1	1.0 μm	Invitrogen
	PS-MAG-SA	0.540 μm	Microparticles GmbH
JPA808	SiO_2-MAG-SA	1.0 μm	Microparticles GmbH
	Dynabeads MyOne Streptavidin T1	1.0 μm	Invitrogen
	ProMag 1 Series Streptavidin	0.97 μm	Bang Laboratories
	PS-MAG-SA	0.630 μm	Microparticles GmbH
	PS-MAG-SA	0.540 μm	Microparticles GmbH

Table 3.2. List of all streptavidin-coated superparamagnetic polystyrene beads investiaged during sticking experiments to either bacterial strains HCB1737, MTB32 and JPA808. All the beads attached successfully.

agnetic beads whose diameters range from 500 nm to 1 μm were used and Table 3.2 summarises the different streptavidin-coated beads which have been successfully attached to either biotinylated filaments or hooks. The assay above is highly reproducible and the yields obtained were very good. It is useful to note that better yields were obtained for micron-sized beads compared to half-micron ones. This can be attributed to differences in sedimentation times, bead concentrations and clumping properties.

3.2 Rotational measurements

The aim of this section is to establish a method to measure X-Y position of the bead attached to a motor with time. This measurement will allow me to obtain speed-time traces for the motor and the angle of the bead orientation. The speed-time traces will

reveal potential speed changes in the motor in the presence and absence of a rotating magnetic field. I am interested to keep track of speed changes in order to find out if stators do drop out at low load. On the other hand, the ability to determine the bead orientation will allow me to measure the angle between the easy axis of the bead and the magnetic field, $\Delta\theta$, which is a measure of the magnetic torque delivered to the particle.

The X-Y position of the magnetic bead assay can be determined using back-focal-plane (BFP) interferometry (Gittes & Schmidt, 1998). The method of detecting the position was considered due to its high sensitivity, low electronic noise and simplicity due to the low number of sensors. Also, the laser power used is often on the order of a few mW which should pose no photodamage to the cells.

This technique was implemented on the same inverted bright-field microscope used in Chapter 2 in which an additional optical trap was introduced. BFP interferometry involves focusing a weak infra-red laser spot on the bead and imaging the scattered light at back-focal-plane onto a quadrant photo-diode (QPD). The four quadrants are schematically shown in Figure 3.3.

Most of the electronics required to operate the quadrant photo-diode were inherited from the previous set-up by Rowe (2005). I upgraded the data acquisition boards and programs in order to make use of more recent LabVIEW data acquisition functions (NI BNC-2110 & NI PCI-6221, National Instruments). The four signals are manipulated as given in Equation (3.1) in order to obtain X- and Y-signals of the bead.

$$X = \frac{(C+D)-(A+B)}{A+B+C+D} \qquad Y = \frac{(A+D)-(B+C)}{A+B+C+D} \tag{3.1}$$

Examples of rotational signals that can be obtained with the electromagnet installed in this microscope system are shown on the left end of Figure 3.4. The 1 micron data was taken using Dynabeads MyOne Streptavidin T1 superparamagnetic

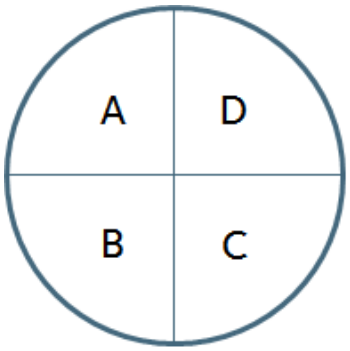

Figure 3.3. The four quadrants of the quadrant photo-diode (QPD).

beads while the half micron data was taken using 0.540 μm superparamagnetic beads (PS-MAG-SA, Microparticles GmbH).

In order to obtain a measure for rotational speed of the assay, the signals obtained were passed through an ellipse-fitting program written by Dr Richard Berry. This program first determines the centroid of the orbit and obtains a simple fit in which the two axes for the orbit is determined. The major axis is the one that passes through the centroid and minimises the moment of inertia of the data while the minor axis is orthogonal to the major axis. Scaling factors for each axis are determined from the moment of inertia calculation. This is followed by a simplex minimising program to further optimise the fit. The simplex-optimised elliptical fit is then re-transformed onto a circle and the original data points are rescaled and rotated accordingly. Following this ellipse fit, the data is passed through a spectral analysis program to determine the dominant frequency present in the signal. The spectral analyser converts the transformed x- and y-signals into polar form. A Fourier transform is carried out on the polar signals to obtain a power spectrum for the signal. The dominant frequency present is then taken to be the average rotational speed of the assay in that window of data points.

The time resolution for the speed-time trace depends on the number of samples used from the actual data and the speed resolution depends on the sampling rate and the total size of the block of samples passed into the spectral analysis program. A

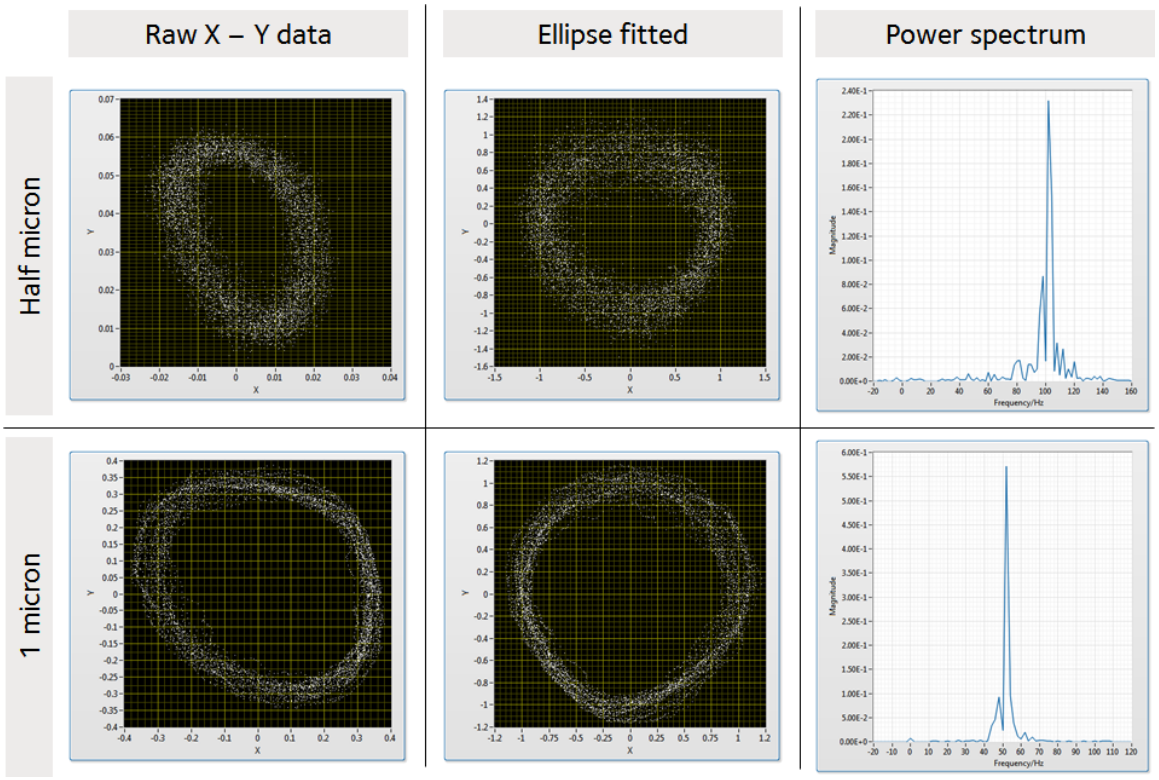

Figure 3.4. (Left) Raw rotational signals obtained from two rotating bead assays, 1 micron and half micron, in the absence of a rotating magnetic field. The signals span 0.5 s. **(Middle)** Transformation of the raw rotational signal after ellipse fitting. **(Right)** Power spectrum obtained from transformed elliptically fitted data. The dominant peak in the power spectrum is taken to be the average rotational speed for the given time window.

rectangular window is used and zero paddings are added to the ends of this window to increase the total block size. The method of beefing up the block with zero paddings is valid because there is *a priori* knowledge that only a single frequency is present in the signal. This approach is analogous to the localisation method used in photo-activated localisation microscopy (PALM). In this localisation method, there is *a priori* knowledge that only one molecule is emitting at any one time. The combined ability of choosing small time windows and large block sizes allow me to obtain highly resolved speed-time traces at short time-scales.

The subfigures shown in the middle of Figure 3.4 show how the rotational signals presented previously transformed after the ellipse fit. The transformed signals were then passed through a spectral-analysis program to obtain a power spectrum for the frequency components present in the signal shown on the right of Figure 3.4. The power spectrum for the half-micron magnetic bead-hook assay displays a dominant peak at 102 Hz which is taken as the average rotational speed of the assay in this window containing 0.5 s of data. Similarly, the power spectrum for the micron magnetic bead-hook assay shows a dominant peak at 52 Hz. Smaller peaks are present in both spectra and they can be attributed to imperfections in the rotational signals passed into the spectral analyser.

In order to find out whether I could use any angular data, raw or ellipse-fitted, I would have to obtain an estimate for the linear regime of this signal. In an attempt to characterise this regime, I stuck a single 1 μm superparamagnetic bead (Dynabeads MyOne Streptavidin T1, Invitrogen) to poly-l-lysine-coated coverslips and the stuck bead was made to trace out circles and crosses using a 3-axis piezo-controlled stage (P517, PI). The stage is able to travel a maximum distance of 100 μm in either x- and y-direction at a maximum input of 10 V. As such, a 50 nm travel only requires an input of 0.005 V. A dry Nikon condenser of numerical aperture 0.85 was used in the following experiments.

Figure 3.5 shows the X- and Y-signals obtained when the piezo is made to travel a distance of 1.2 μm in each of the two directions at a specific z-input. The range for the X-signal spans near 0.7 while the range for the Y signal is larger at 0.8. For the X-signal, the signal is approximately proportional to distance travelled by the piezo between -400 nm up to 200 nm, spanning a range of 600 nm. The gradient of the linear regime is approximately 0.15 a.u. per 100 nm where a.u. stands for arbitrary units. The Y-signal is approximately proportional to distance travelled by the piezo between -400 nm up to 100 nm, spanning a range of 500 nm. The gradient of the linear regime for the Y-signal is approximately 0.168 a.u. per 100 nm. The mismatch between the linear regime between the X- and Y-signals is likely due to slight optical misalignment and shape anisotropy of the bead.

The general factors that affect the range of this linear regime include the diameter of the bead, the size of the image of the back-focal plane, the detector size, the radius of the input beam. The radius of the input beam entering the objective will determine the size of the focal spot. Decreasing the radius of the input beam will increase the width of the focal spot and the range of the linear regime. The use of a larger bead diameters will decrease the range of the linear regime (Gittes & Schmidt, 1998). Finally, decreasing the ratio of the image of the back-focal-plane to the detector size increases the linear range of the linear regime. Should the radius of trajectory of the bead assay be near the extreme of the linear regime, the ellipse-fitting method described earlier can be used to linearise the detector signal.

I also investigated cross-talk effects near the extreme by making the fixed bead trace a cross 600 nm wide and 600 nm tall. The X-Y trace for this motion is shown in Figure 3.6. Distortion to the signal can be seen near the top and left of the cross. Otherwise, the cross-talk effects are fairly minimal near the centre of the cross. The subfigure on the right of Figure 3.6 shows the X-Y trace of a fixed 1 μm superparamagnetic bead tracing out a circle of radius 600 nm in which the circle

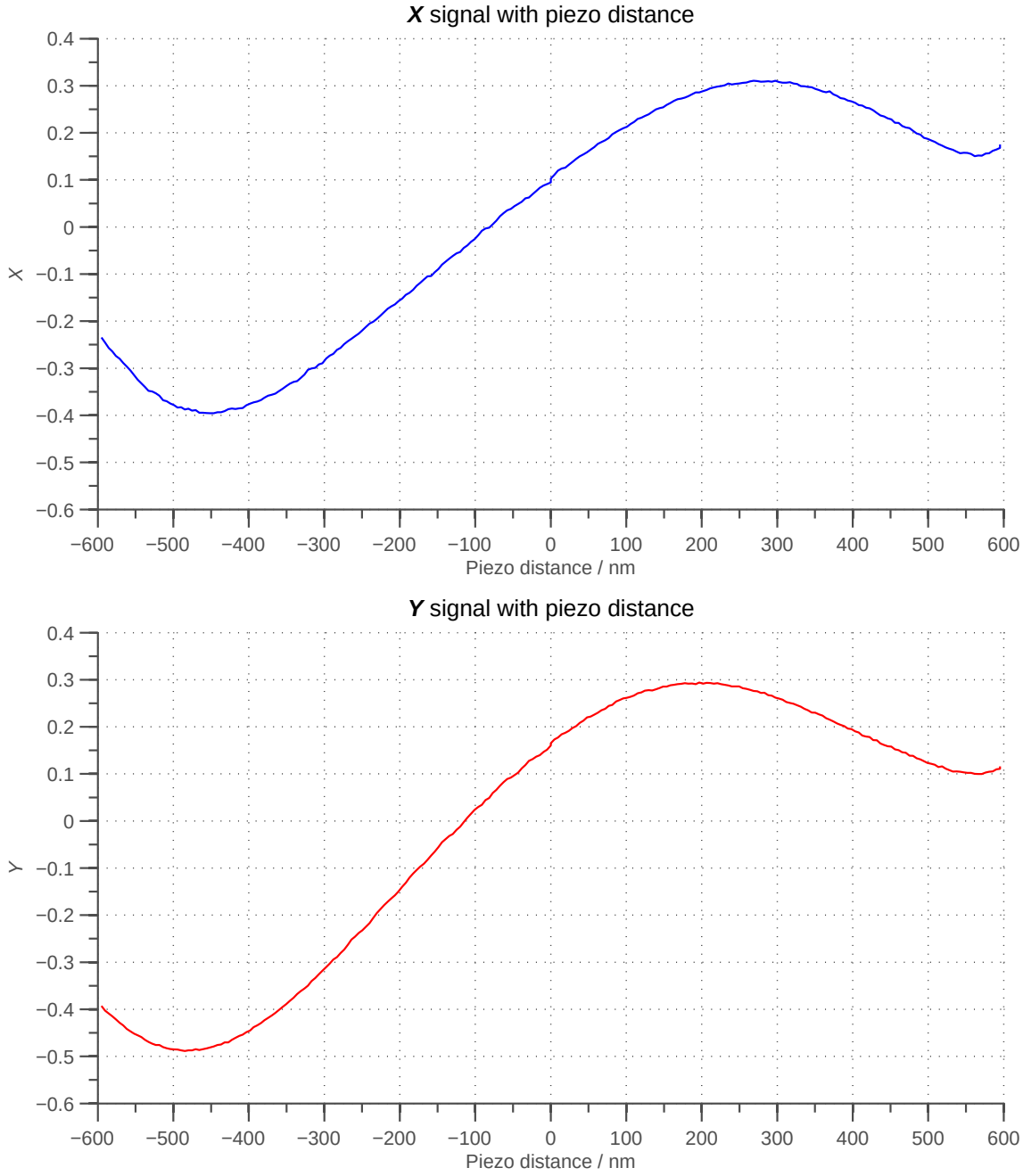

Figure 3.5. (Top) X-signal **(bottom)** Y-signal with piezo distance travelled. The linear regime for the X-signal spans about 600 nm while the linear regime for the Y-signal spans about 500 nm.

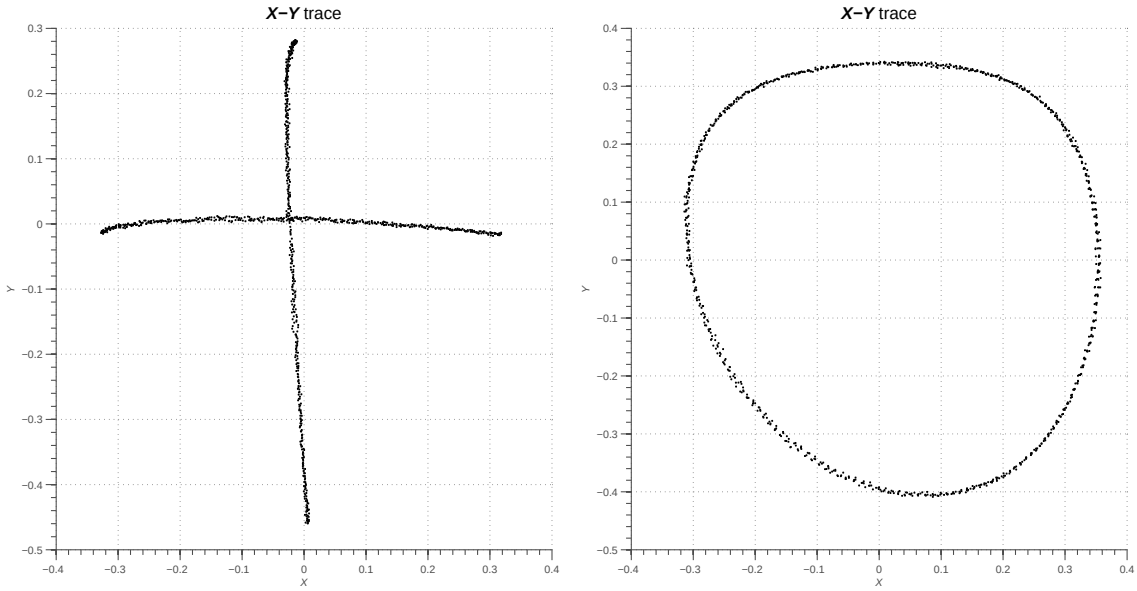

Figure 3.6. (Left) X-Y trace of a fixed 1 μm superparamagnetic bead tracing out a cross 600 nm wide and 600 nm tall. Distortions can be seen near the top and the left end of the cross. **(Right)** X-Y trace of a fixed 1 μm superparamagnetic bead tracing out a circle of radius 600 nm. The shape of the circle is slightly distorted.

looks slightly distorted. The results obtained for both Figures 3.5 and 3.6 reveal that angular data obtained from orbital trajectories having diameters above 500 nm have to be treated with care. This would mean that the angular data obtained from the 1 micron data shown in Figure 3.4 is not reliable. On the other hand, it is reliable to use the angular data from the ellipse fit for the half micron data. The angular data is shown in Figure 3.7.

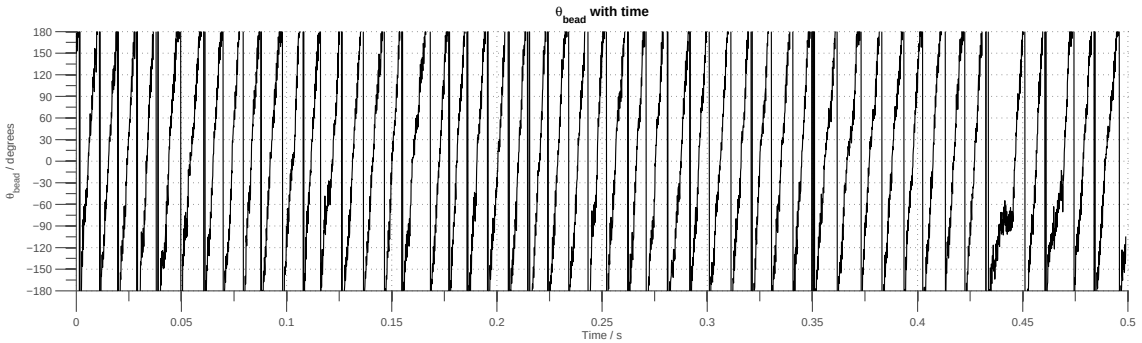

Figure 3.7. θ_{bead} of the half-micron data with time. There are regions where the cell slows down which may contribute to the side peaks present in the power spectrum.

It has to be noted that the characterisation of the above linear regime and cross-talk effects were carried out in the absence of a electromagnet and this characterisation was not carried out at the start of all the rotation experiments. It is very much possible that the linear regime varies from bead to bead. One possible solution to this problem is to increase the range of the linear regime by constricting the beam size into the objective (Pilizota *et al.*, 2007). The increase in the range of the linear regimes comes at the expense of X-Y sensitivity. Finally, I would like to note that X-Y cross talk was minimised manually by fine-adjustment of the piezo stage. The stage is fine-adjusted such that the best possible orbital trajectory was obtained when the assay is rotating in the absence of any magnetic field.

3.3 The magnetic tweezers

(***Declaration of contributions for this section:*** *The main principles behind the electromagnet were established by Dr Alexy Karenowska. Dr Richard Berry and I designed the three-pole electromagnets where the soft iron blocks and pole pieces were fabricated by members of the Clarendon Research Workshop. The amplifier to drive the electromagnet was inherited from Dr Alexy Karenowska. I was responsible for putting all the elements of the electromagnets together. I also calibrated and wrote the programs to control the electromagnets.*)

The main component of the magnetic tweezers developed consists of a three-pole electromagnet. This electromagnet is a variant on the six-pole electromagnet developed by Gosse & Croquette (2002) and a four-pole electromagnet developed by Dr Alexy Karenowska. The three-pole electromagnet was chosen due to the simplicity in its design and its use of minimal material in the optical path. Two electromagnets were made, named Mk IIa and Mk IIb (the model name Mk I has been reserved for the four-pole electromagnet designed and built by Dr Alexy Karenowska). Figure 3.8

shows a top-down schematic of the electromagnet, a photograph of the electromagnet MK IIa and an oblique view of the electromagnet Mk IIb. Both electromagnets were made from two materials: a highly magnetic-permeable ferrite core (magnetic permeability ≈ 10000, W material, Magnetics) and soft iron. The soft iron was used as material for the block pieces and removable pole pieces, coloured red and green respectively in Figure 3.8.

The width and height of the cross-section of the ferrite core are 21.0 mm by 18.0 mm respectively. The dimensions of the soft iron block are 10.0 mm wide by 29.5 mm long by 4.0 mm high. This block is epoxy-glued to the ferrite core around the edges of the block and not in between the ferrite core and the block. The slots present in the blocks allow the pole pieces to be bolted to electromagnet. In addition, these slots can be used to vary the spacing of the gap between the pole pieces. The actual dimensions of the pole piece used are shown in Figure 3.9. It is important to install the blocks such that they obey a three-fold symmetry.

An enamelled 20 SWG magnetic wire (1 mm in diameter) was used to wind three separate coils around the electromagnet. A polyimide film known as Kapton was used for electrical and thermal insulation between wire layers and at the ends of each coil. There are 103 turns in each coil of Mk IIa while Mk IIb has 108 turns in each coil. Two different sets of pole pieces were made for each electromagnet having similar dimensions as that shown in Figure 3.9 except that the first set, used for Mk IIa, had a flat bottom and the tips were manually bent.

In order to understand how a rotating magnetic field can be generated using this electromagnet, it is useful to find out what happens when one of the three coils is powered. When a DC current is delivered into one coil, three possible magnetic loops can occur which pass through the pole pieces. These loops are shown in Figure 3.10. Each loop will give rise to a magnetic vector in the centre of the pole pieces and the superposition of the vectors from each loop will give rise to a resultant vector shown in

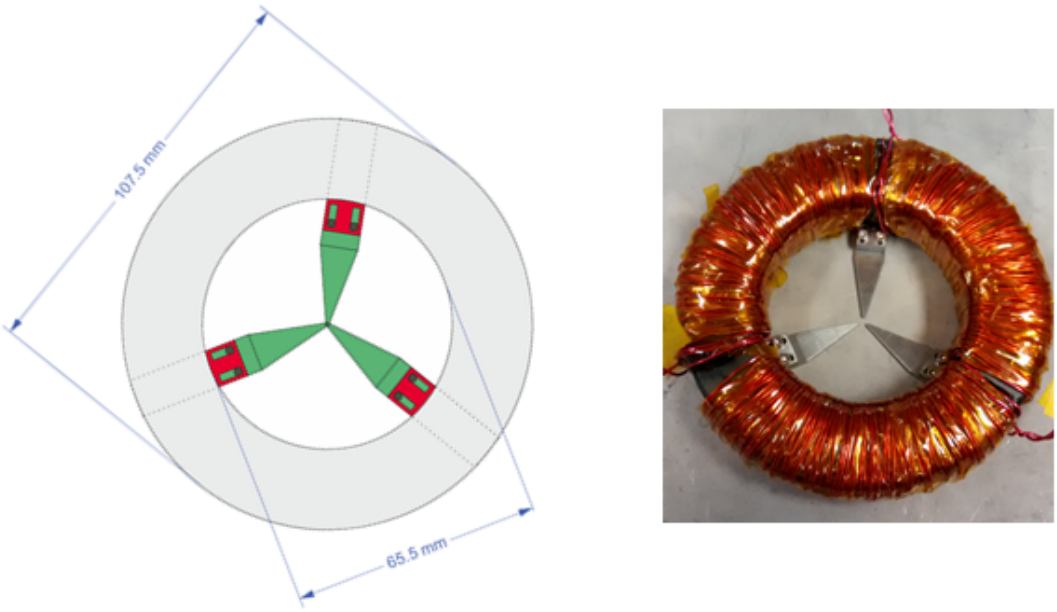

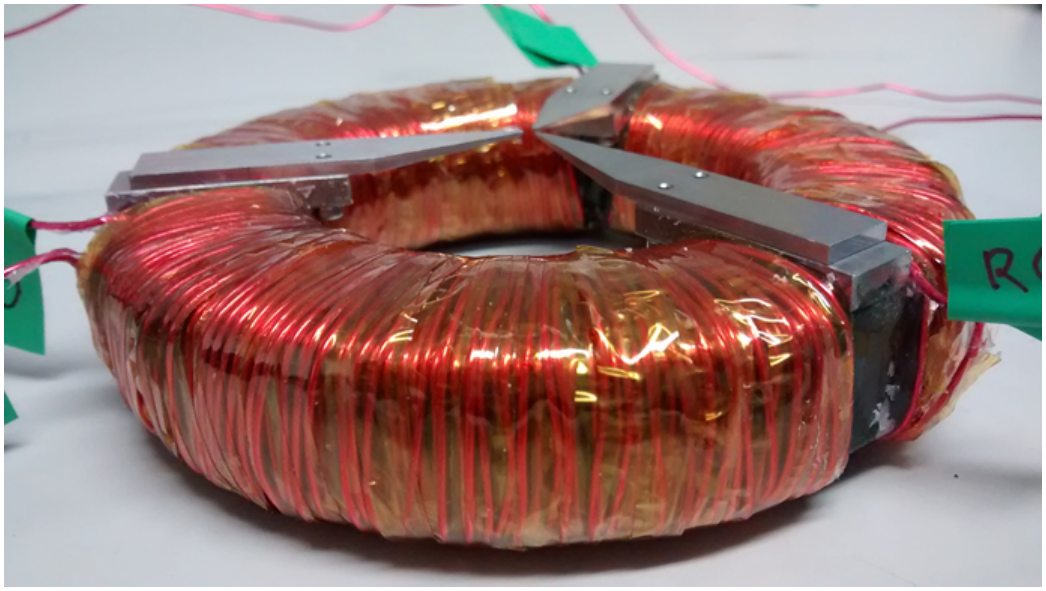

Figure 3.8. **(Top left)** Top-down schematic of the three-pole electromagnet. The grey region is made up of a highly magnetic-permeable ferrite core (0W-49718-TC, Magnetics). The parts coloured in red and green are made from soft iron. The red block of soft iron is epoxy-glued and fixed to the ferrite core while the pole pieces coloured in green is bolted to the soft iron block. These pole pieces are removable and the slots present in the soft iron block allow the gap-spacing between the pole pieces to be varied. **(Top right)** Photograph of the electromagnet Mk IIa. **(Bottom)** Oblique view of the electromagnet Mk IIb.

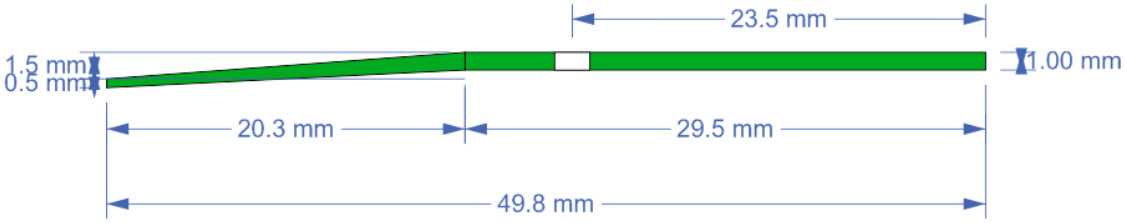

Figure 3.9. Actual dimensions of a single soft iron pole piece.

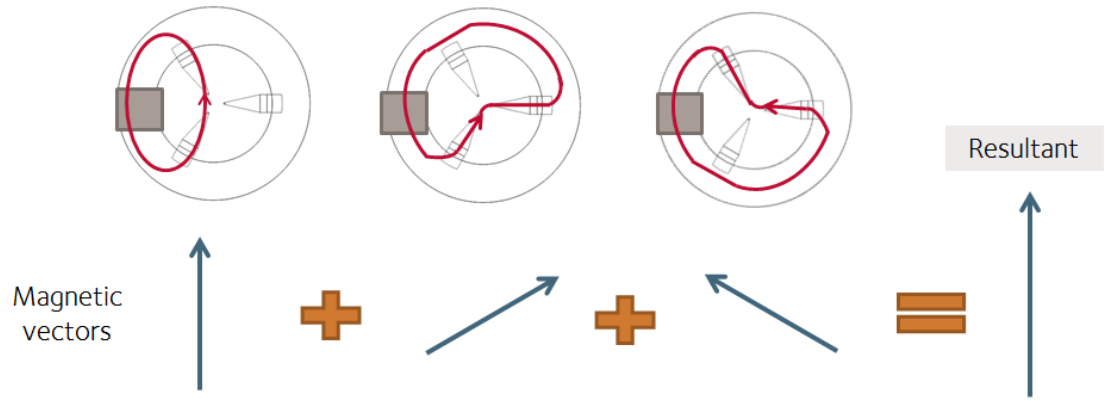

Figure 3.10. The three magnetic loops which pass through the pole pieces when a single coil is powered. The magnetic vector associated with each loop is shown below. Superposition of these three vectors give rise to a resultant vector shown.

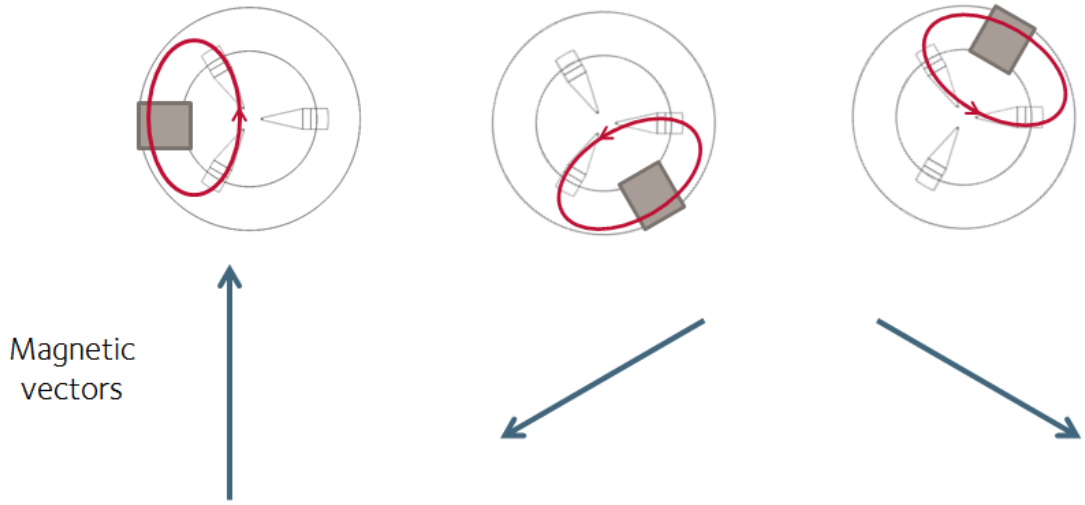

Figure 3.11. Resultant magnetic vectors obtained from the three different coils. Each of these vectors form a basis vector for the magnetic field in the middle of the gap.

the same figure. From the considerations above, we can conclude that the remaining coils will generate resultant magnetic vectors in directions shown in Figure 3.11.

Another loop which does not pass through the pole pieces can exist. This other loop is one that runs around the ferrite core and it is recognised that a residual static field can exist in this core. The static field inside the core can be set equal to zero if the 120° out-of-phase sinusoidal signals centred around zero are sent to all three coils.

The magnetic vectors form a set of basis vectors for the magnetic field present in the middle of the gap. Assuming that there is no imperfection in the symmetry of the electromagnet, the magnetic field can be written as the sum of 3 basis vectors as shown

$$\boldsymbol{B} = \beta\left(\boldsymbol{B_1} + \boldsymbol{B_2} + \boldsymbol{B_3}\right) \tag{3.2}$$

where

$$\boldsymbol{B_1} = I_1 \begin{pmatrix} 1 \\ 0 \end{pmatrix} \qquad \boldsymbol{B_2} = I_2 \begin{pmatrix} -1/2 \\ \sqrt{3}/2 \end{pmatrix} \qquad \boldsymbol{B_3} = I_3 \begin{pmatrix} -1/2 \\ -\sqrt{3}/2 \end{pmatrix} \tag{3.3}$$

where β is a constant of proportionality, assumed to be the same for all the coils by symmetry; and $\boldsymbol{B_n}$ and I_n represent the magnetic vector and current measured for coil n respectively. The coils and vectors are defined in a counter-clockwise direction to reflect the actual top-down view of the orientation of the coils for the electromagnets. The orientation of the coils is the same for both Mk IIa and Mk IIb. It is thus possible to control the magnitude and direction of the magnetic field in the gap by varying the current and phase through each of the three coils. A rotating magnetic field can be easily attained by sending three input sinusoidal currents, each 120° out-of-phase with its neighbouring current.

Attempts were made to determine the magnitude of the magnetic field vector in the middle of the gap. When a DC current of 3.15 A was delivered to a single coil, the magnitude of the field obtained was 28.19 mT using a Gaussmeter (GM04, Hirst) in a gap-spacing of radius 1 mm. A magnitude of 12.53 mT was obtained for a gap-spacing of radius 2 mm. We were not able to measure the rotational behaviour of this vector due the lack of AC capability for the Gaussmeter used. Also, we recognised that the field magnitude measure is an averaged value across the cross-sectional area of the Hall probe sensor of the Gaussmeter. The radius and thickness of this sensor are 2 mm and 1 mm respectively. The overall dimension of the probe also hinders the orientation of the sensor in smaller gaps.

The magnitude of the magnetic field obtained here is less than 60 mT quoted in the previous chapter to rotate micron-sized superparamagnetic bead at speeds above 350 Hz. However, I expect more field to be present especially when sinusoidal inputs are delivered to all three coils. The mutual inductive effect of all three coils can also

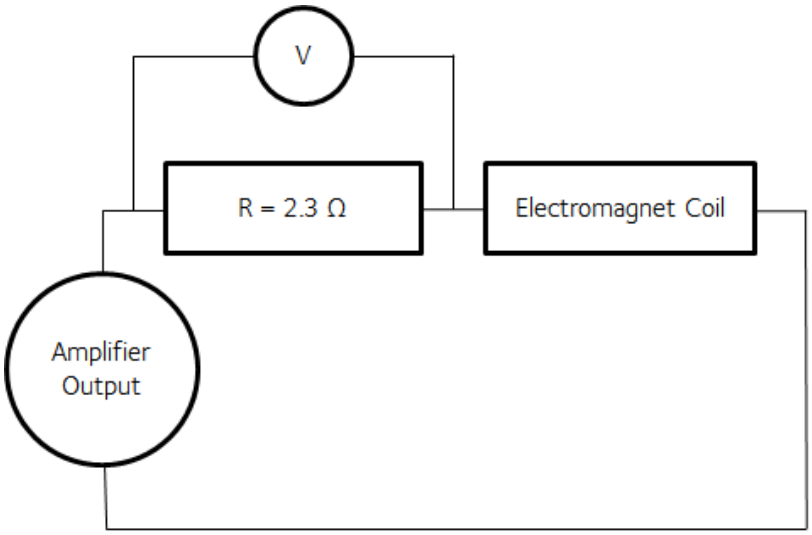

Figure 3.12. Circuit diagram for a single electromagnet coil. The current in the circuit is determined from the voltage drop across the load resistor.

lead to a larger magnetic field at the centre of the gap.

3.4 Amplifier characterisation

Three outputs from a car audio amplifier (EAPA450, Nikkai) were used to drive the currents through each coil separately as shown in Figure 3.12. A load resistor of resistance 2.3 Ω with a power rating of 150 W (HS150 2R2 J, ARCOL) was used to dictate the current through the circuit and also functioned as a heat dump. The resistances were measured manually using a hand-held digital multimeter (FL175, Fluke). In order to determine the current flowing in each coil at any given time, a data acquisition device (NI 9215, National Instruments) was used to measure the voltage drop across the load resistor.

The two electromagnets were calibrated differently. Electromagnet Mk IIa is calibrated as follows:

- A voltage-output module (NI 9263, National Instruments) was used as a signal generator to modulate the inputs into the amplifier. Three sinusoidal signals,

centred around zero and 120°-out-of-phase with each other, were delivered to the amplifier.

- Amplitudes for all three coils were varied simultaneously in order to obtain the same current amplitude values for each coil.
- The individual amplitudes for each of three coil were recorded to file.

The voltage inputs required to achieve specific currents at different frequencies for Coil 1 of the electromagnet Mk IIa is shown in Figure 3.13. The figure shows that larger inputs are required at frequencies less than 50 Hz indicating the presence of a low-pass filter in the amplifier. Beyond 50 Hz, the voltage input was observed to increase steadily. This could be a property of the amplifier or the increasing impedance in the coil at higher frequencies. Similarly shaped curves were obtained for the remaining two coils which are shown in Figure 3.14.

Electromagnet Mk IIb was calibrated in a different way. Instead of simultaneously varying the three amplitudes to obtain the same peak-to-peak current values for all three coils, the amplitudes were varied based on the magnetic vector in the middle of the gap determined using Equation (3.3).

The input values for Electromagnet MK IIb were manually modified in order to ensure that the standard deviation in the magnitude of the magnetic vector in the gap was less than 1% of the mean magnitude. The input voltages required to attain specific currents at different frequencies for all three coils of this electromagnet are shown in Figure 3.16. Again, the shape of the curves are broadly similar with that found for electromagnet Mk IIa but the amplitudes required to achieve the same peak-to-peak current is now less. This could be due to the increased number of turns used for each coil in Mk IIb, thereby increasing the effects of mutual inductance.

Best attempts were made during the calibration process to ensure that the magnetic vector has a uniform magnitude across different angles but it was noted that

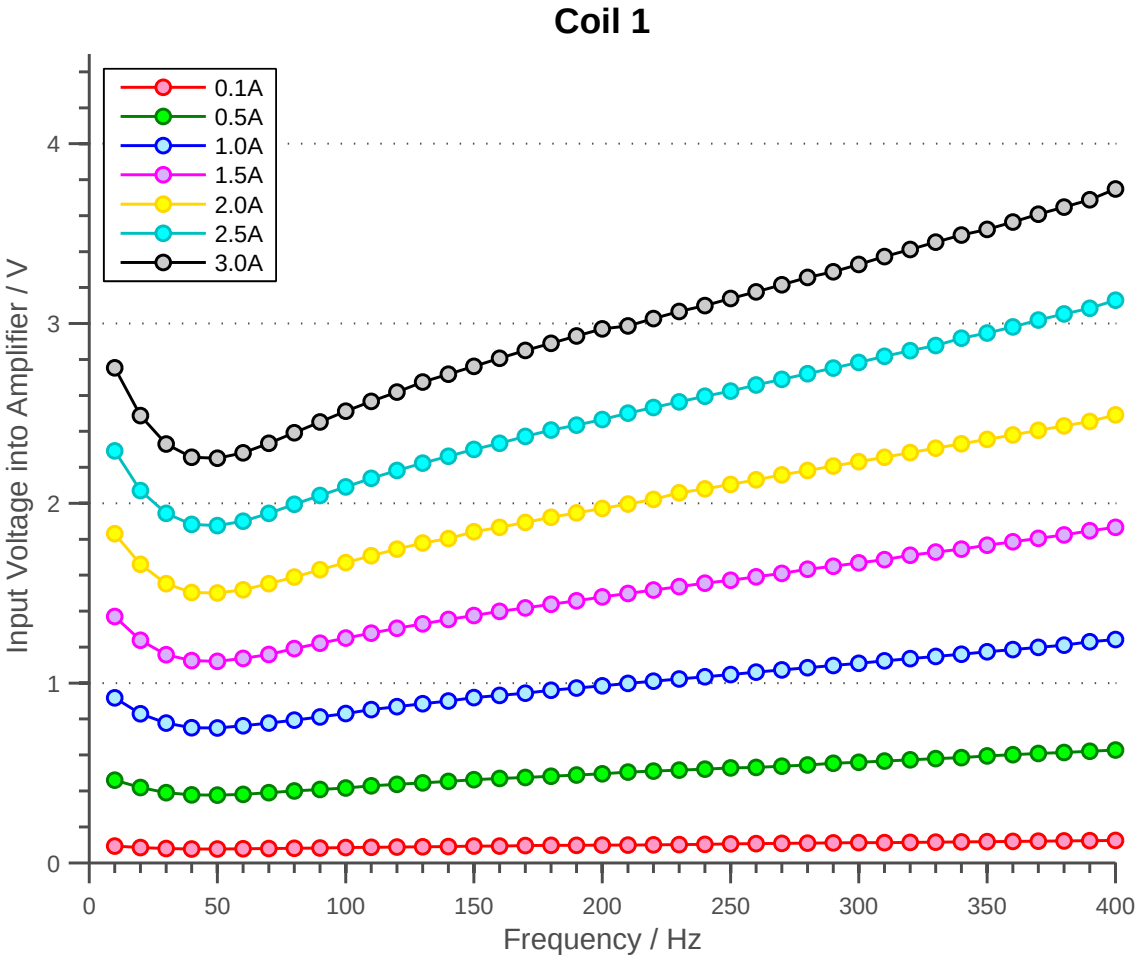

Figure 3.13. Voltage inputs required to achieve specific current amplitude at different frequencies for Coil 1 of the electromagnet Mk IIa.

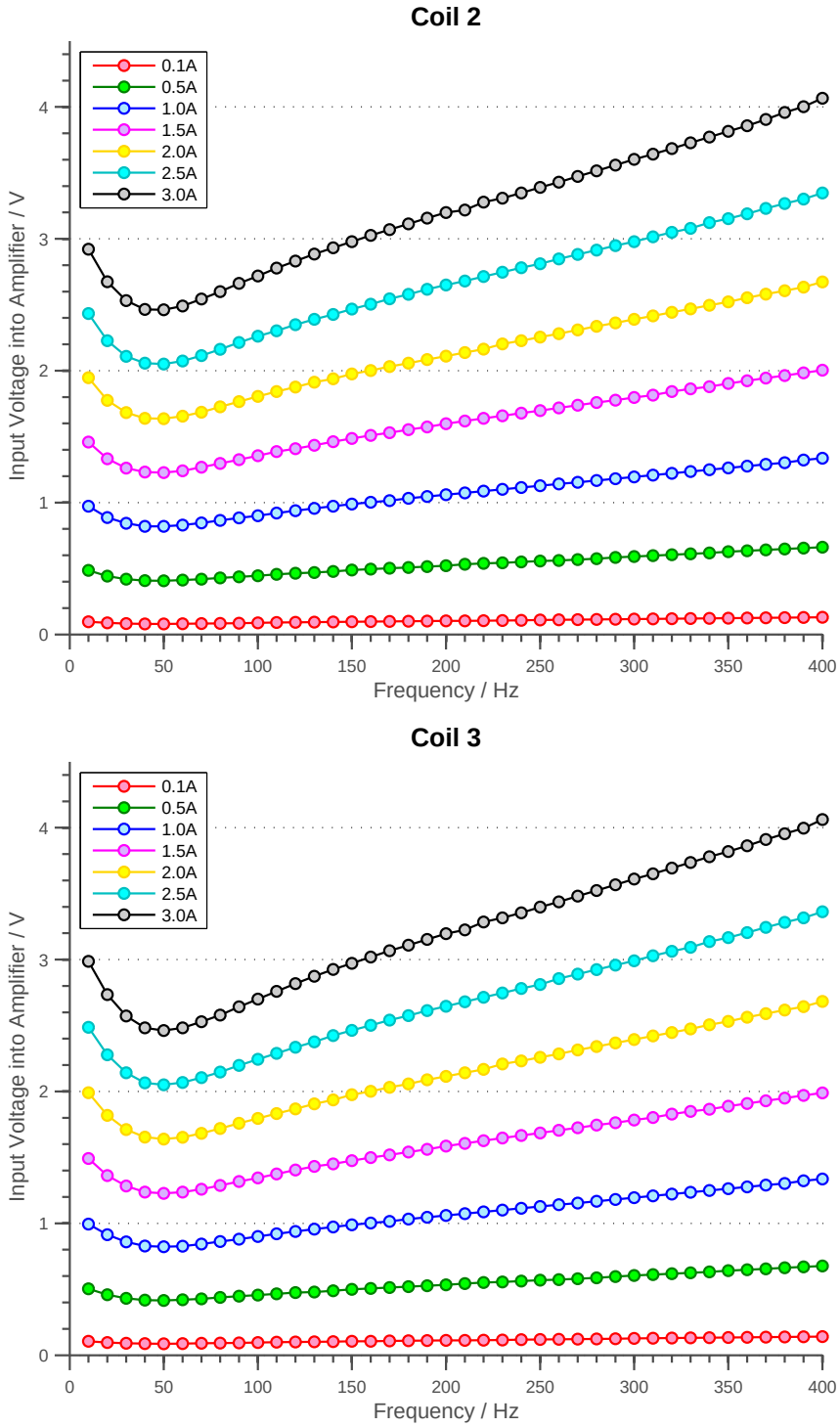

Figure 3.14. Voltage inputs required to achieve specific current amplitude at different frequencies for the remaining two coils of the electromagnet Mk IIa.

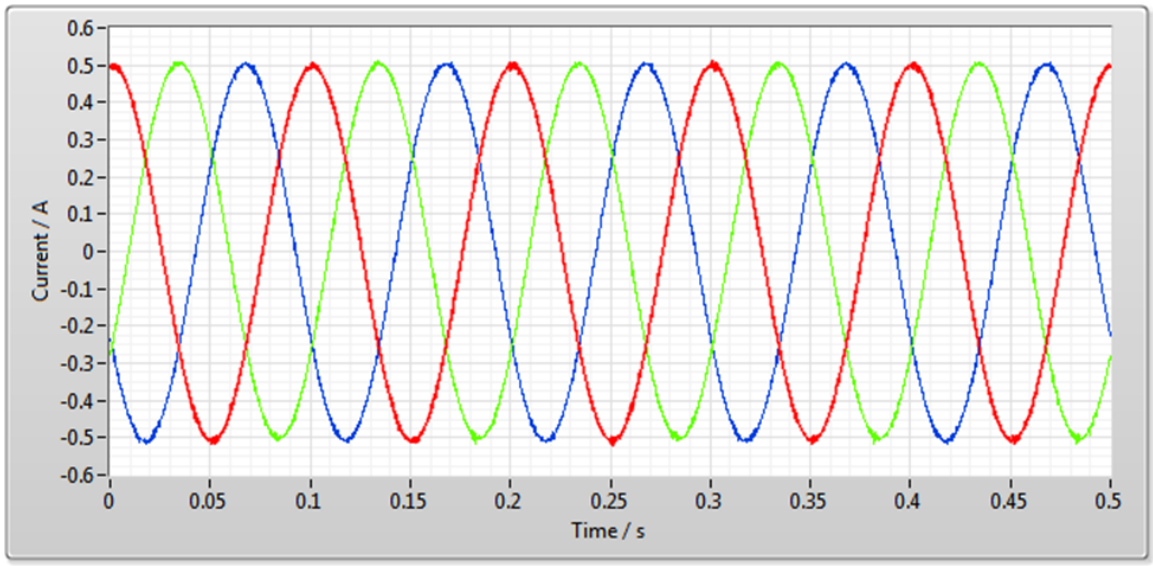

Figure 3.15. Measured currents through each coil (red for coil 1, green for coil 2, blue for coil 3) from three 10 Hz sinusoidal signals.

the input values were sensitive to any movements of the magnetic wiring and also any distinct frequency change.

Figure 3.17 shows the magnitude of the magnetic vector determined using Equations (3.2) and (3.3) with time. The frequency of this input block is 10 Hz and the previous input block consisted of ten revolutions of a 5 Hz input train. There is a huge variation in the magnitude on the first cycle which is due to the abrupt change going from 5 Hz signals to 10 Hz signals. The overall standard deviation in this signal is 0.297 which is about 4% of the measured mean magnitude (7.009). The remaining cycles were observed to settle to a steady magnitude and if one is to exclude magnitude measurements in the first 0.15 s, the standard deviation of the magnitude decreases to 0.053.

The following input blocks sent to the amplifier consisted of ten revolutions at different frequencies from 5 Hz up to 200 Hz at 5 Hz intervals. The mean magnitude at higher frequencies were observed to settle much quicker than that going from a 5 Hz input to 10 Hz. Figure 3.18 demonstrates this observation for a block containing 100 Hz input. The mean magnitude at this frequency is 6.942 and the standard

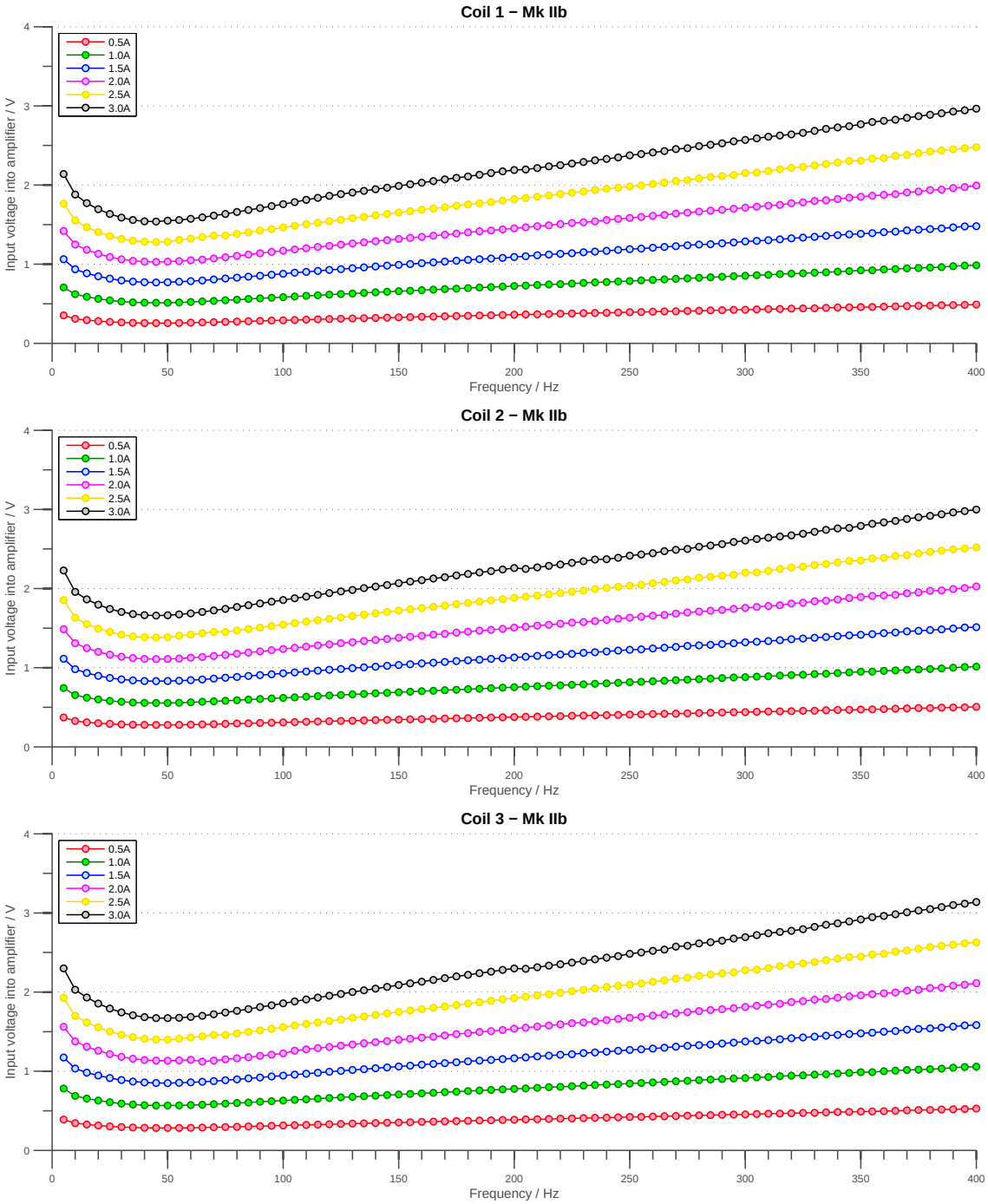

Figure 3.16. Voltage inputs required to achieve specific current amplitude at different frequencies for all three coils of the electromagnet Mk IIb.

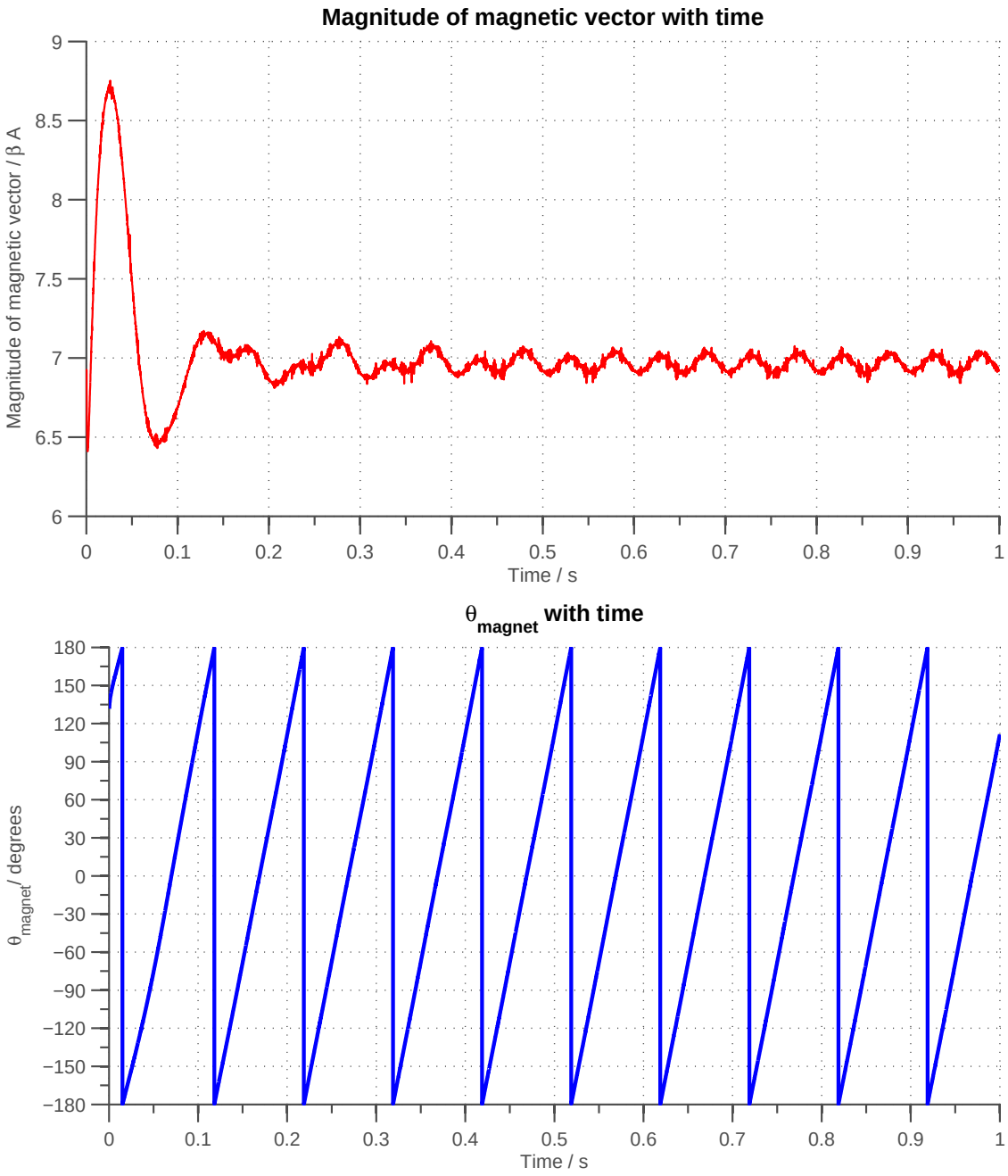

Figure 3.17. Polar components, magnitude and theta, of the magnetic vector with time for 10 revolutions at 10 Hz. The magnetic vector is determined using Equation (3.2). A transient is observed when going from a 5 Hz input at 10 revolutions to a 10 Hz input at 10 revolutions.

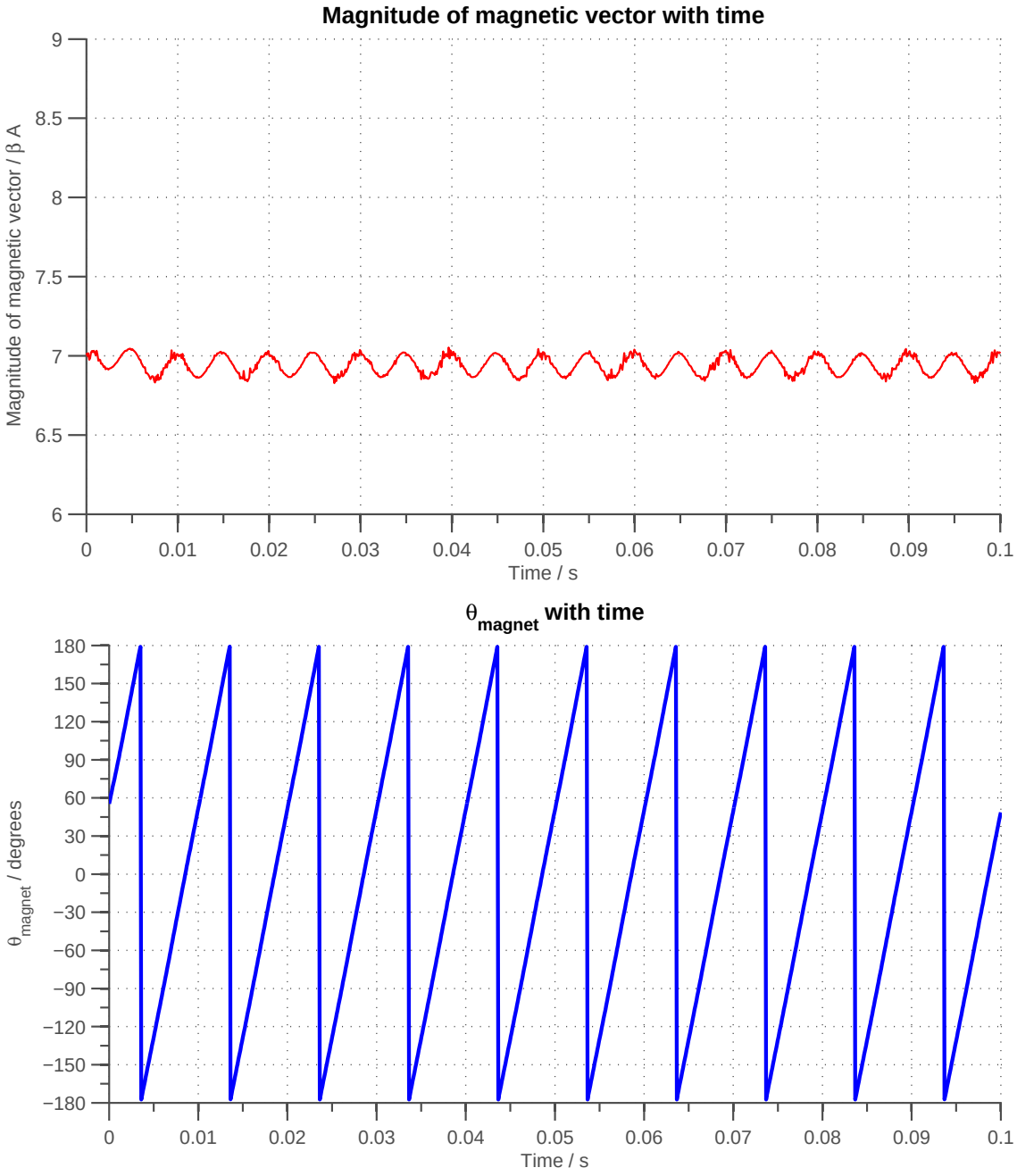

Figure 3.18. Polar components of magnetic vector for 10 revolutions at 100 Hz. The transient appears less going from 10 revolutions at 95 Hz to 10 revolutions at 100 Hz.

deviation is 0.057.

The input blocks consisting of ten revolutions at different frequencies ranging from 5 Hz to 200 Hz at 5 Hz intervals can be used to generate a plot of the mean magnitude of the magnetic vector at different frequencies. This plot is shown in Figure 3.19 where the total size of the error bar is taken to be two times the standard deviation of the data in the block containing the specified frequency. This figure shows that first cycles in each block settle more quickly and the variational behaviour of each block remained fairly steady at frequencies greater than 20 Hz. There is a slight downward trend in the mean magnitude but this effect is not greater than the overall variational behaviour of the whole train.

During the calibration process, it was noted that the temperature, measured using a thermocouple (AH-50A, RS), of both the amplifier and the load resistors were capable for reaching 55°C especially after high currents were continuously driven through the circuit for more than 20 min. The resistance of each load was measured at the peak temperature reached and no notable difference was recorded. No notable temperature increase was recorded on the surface of the coil.

Following the observed temperature change in the amplifier and the resistor, an attempt to investigate temperature dependence of the magnetic wire at different currents was carried out. Obviously, it was not possible to insert the thermocouple end in between the magnetic wires in the coil due to the presence of the Kapton film for thermal and electrical insulation. As such, an attempt to emulate actual conditions was carried out in the manner shown in Figure 3.20. The end thermocouple (AH-50A, RS) was inserted between two layers of magnetic wire. The first and second layer consisted of fifteen and thirteen turns respectively. A DC power supply (IPS 2303, ISO-TECH) was used to deliver a continuous current to the magnetic wire and the temperature was recorded every 10 s. The temperature change recorded with time up to 3 min is shown in Figure 3.21.

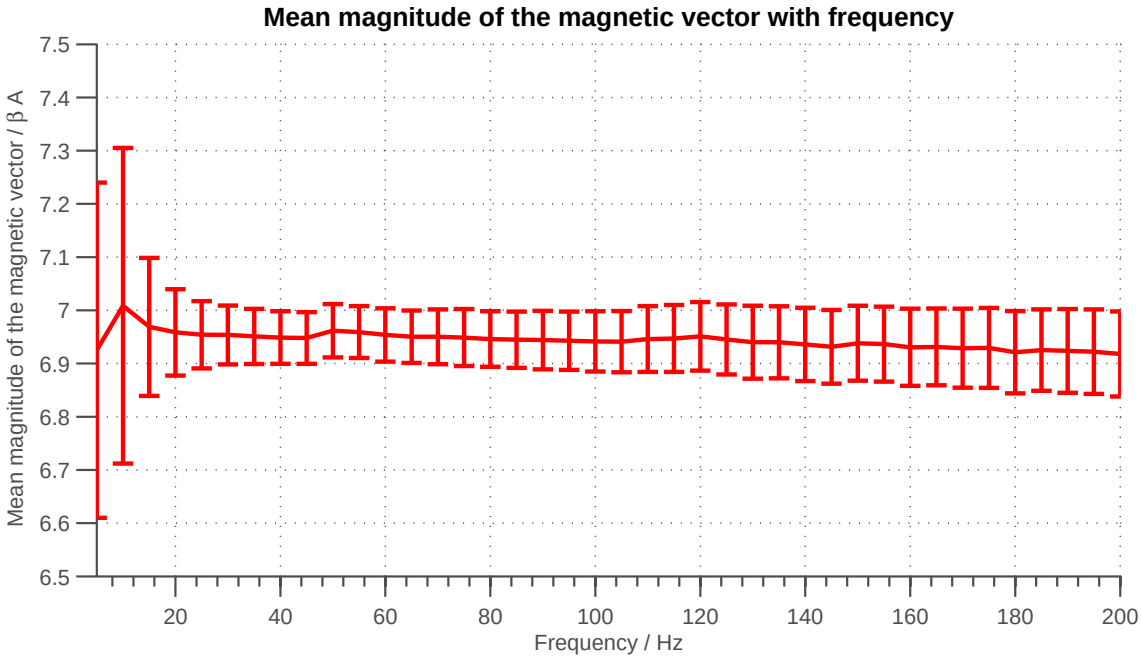

Figure 3.19. Mean magnitude of the magnetic vector with frequency. The total size of the error bar is two times the standard deviation for the block containing that frequency.

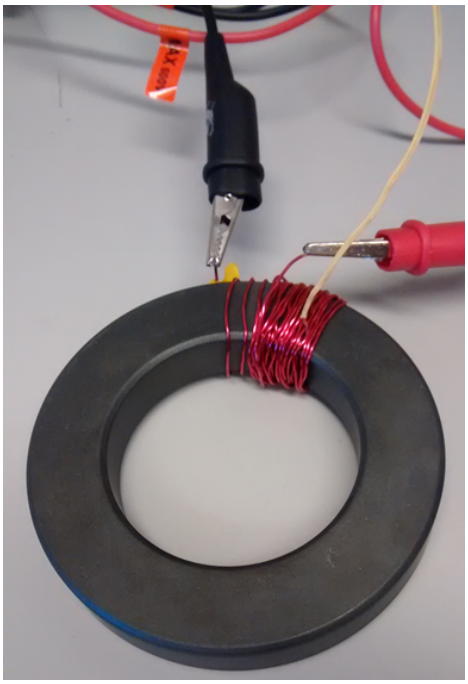

Figure 3.20. Picture showing experimental set-up to investigate temperature dependence of the magnetic wire with input current. The yellow wire is the thermocouple. The ends of the magnetic wire were connected to a DC power supply.

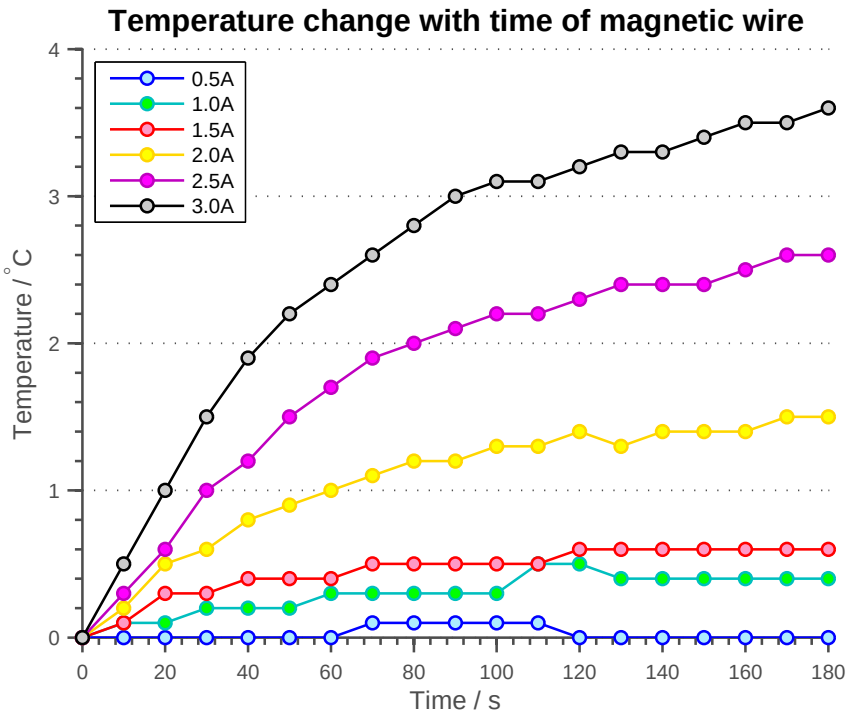

Figure 3.21. Temperature change of the magnetic wire with time at different input currents.

The results obtained showed that there is temperature increase with time for all input currents. For currents less than 2.0 A, a steady-state is reached before the end of the 3 min window. The largest gradient in temperature change is recorded for an input of 3.0 A and the maximum temperature change was about 3.5° for a 3.0 A input after 3 min. Measurements were not taken for a longer time window as the actual experiments carried out involved input blocks no longer than 10 s at any one time to the amplifier. In the same experiment, a temperature decrease of more than 2°C took no longer than 90 s after the current is switched off. This estimate obviously depends on the final temperature attained before the current was switched off but nonetheless still demonstrates the quick cooling nature of the magnetic wires.

3.5 Experimental configuration

In order to deliver magnetic torque to the bacterial flagellar motor, one of the two electromagnets described has to be installed in the inverted bright-field microscope (with BFP interferometric) in such a way that its position is centred relative to the main imaging components of the microscope, the objective and the condenser. At the same time, it is important that the microscope stage holding the sample can move freely relative to the electromagnet. This stage is fixed to the optical bench and is not coupled to the objective and condenser.

I designed and fabricated a perspex holder to mount the electromagnet to a back post which allowed me to centre and fix the position electromagnet relative to the objective and condenser by inspection. Perspex was chosen due to its lack of magnetic inductivity and thermal conductivity. The use of this holder ensures that the position of the electromagnet relative to the objective does not change even when the stage holding the slide is moved. The position of the holder mount on the back post is physically indicated using a fixed block positioned below the holder mount. This allows me to remove the electromagnet and return it to its original position during the change of tunnel slides. Both electromagnets Mk IIa and Mk IIb were installed in the same manner as described above. Figure 3.22 shows a picture of the electromagnet Mk IIa in an experiment to deliver magnetic torque to the bacterial flagellar motor.

A side-view schematic of the experimental configuration around the tunnel slide is shown in Figure 3.23. The reason behind using two coverslips for the tunnel slide, rather than a microscope slide and a coverslip, is evident from this diagram. It allows the pole pieces to get closer to the sample of interest, the rotating magnetic bead assay. This ensures that the assay experiences the largest possible magnetic field strength for given input currents to the electromagnet.

Most of the experimental results shown on the bacterial flagellar motor in the next chapter were carried out with the above configuration, with the exception of the

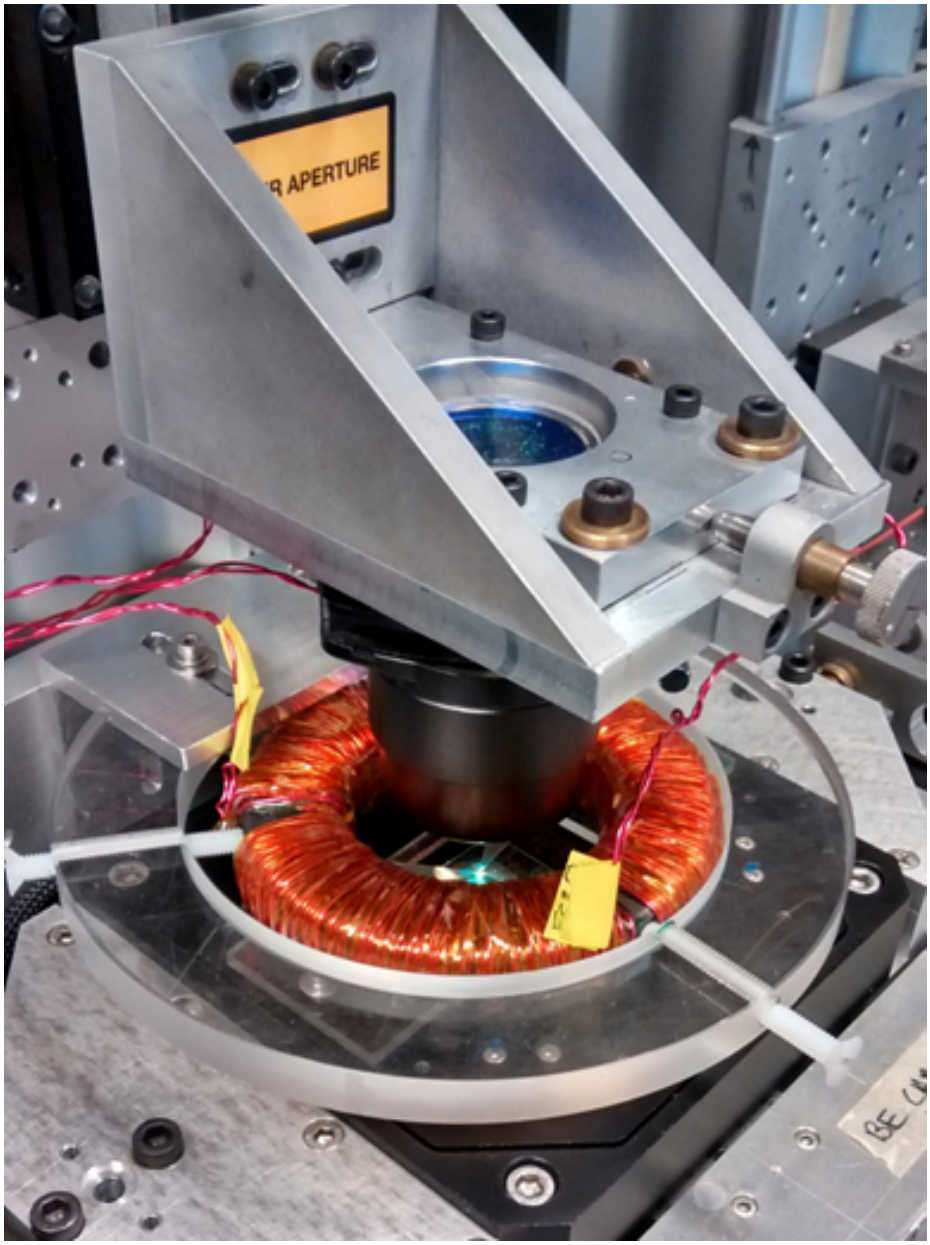

Figure 3.22. The electromagnet Mk IIa held using a perspex holder in an experiment to deliver magnetic torque to the bacterial flagellar motor. The black object above the electromagnet is the condenser and the electromagnet rests very close (less than 1 mm, determined by inspection) to the tunnel slide.

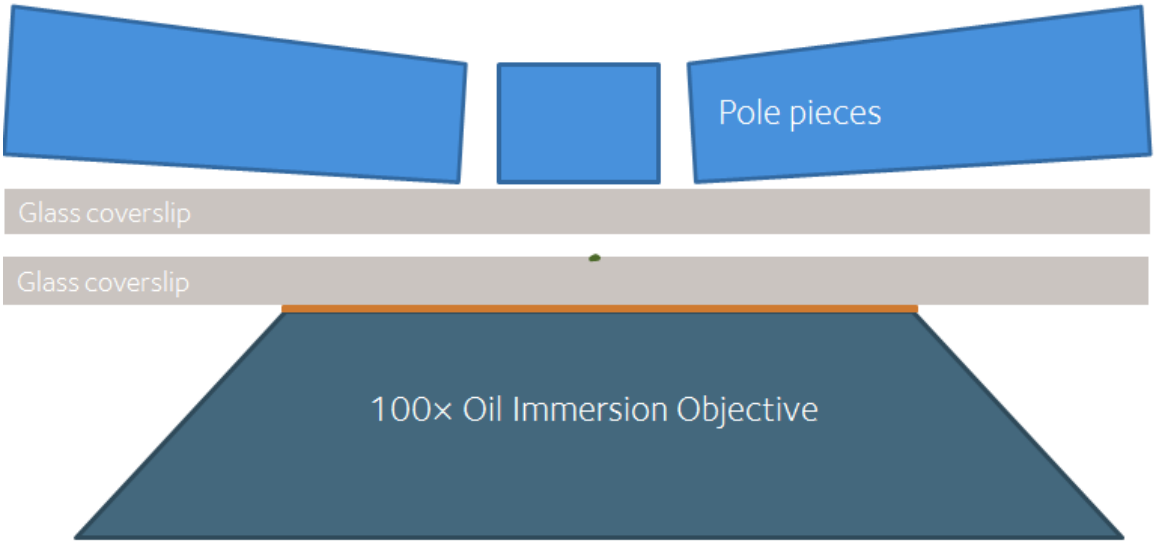

Figure 3.23. Side-view schematic of the experimental configuration close to the tunnel slide, with most elements drawn roughly to scale. The radial spacing of the pole pieces is 1 mm. The glass coverslips used each have a thickness of 170 μm. The height of the tunnel is determined by the thickness of the double-sided sticky tape used which is about 100 μm. The small speck, not drawn to scale, shows the position of one magnetic bead assay in the centre of the field-of-view of the imaging system.

stalling experiments. The stalling experiments were carried out on an epifluorescent microscope. Stalling was induced by bringing a pair of neodymium magnets spaced 4 mm apart mounted on a hard cardboard-holder close to the sample.

Chapter 4

Experimental Results

This chapter contains the main results obtained from experiments in which magnetic torque was delivered to the bacterial flagellar motor. In the first section, I will describe stalling experiments carried out on motors that express GFP-tagged stators. The result obtained contributed to the investigation into the load-dependence assembly behind the flagellar motor published in Tipping *et al.* (2013a).

The following sections contain results from rotation experiments conducted to investigate the effect that a rotating magnetic field on the magnetic bead assay. In these experiments, I was interested in the effects of a rotating magnetic field on the orbital trajectory measured of the bead assay.

These experiments were also conducted to establish a method of measuring the angle between the easy axis of the bead and the magnetic field, $\Delta\theta$. This parameter is required to determine the magnetic torque imparted to the motor. In an attempt to measure this angle, I will describe the experimental procedure used to determine the offset between the angle of the bead measured using BFP interferometry and the easy axis.

The rotation experiments were mostly carried out by driving the magnetic bead-hook assay forwards (CCW direction) and backwards (CW direction). Attempts

to implement a CCW ramp to obtain fast torque-speed measurements will also be described.

The final section presents a key result obtained from rotation experiments carried out on a magnetic bead-filament assay in which stators were observed to drop out at low loads. This result confirms already observed experimental evidence for load dependence on stator dynamics.

4.1 Stall measurements on the bacterial flagellar motor

(***Declaration of contributions for this section:*** *I designed and established the variant of the magnetic bead-filament assay for use in fluorescent stator experiments using a strain developed by Dr Nicolas Delalez and Dr Murray Tipping. Dr Delalez was responsible for culturing the cells while I biotinylated the truncated filaments and attached the streptavidin-coated superparamagnetic beads to them. Both Dr Delalez and I carried the experiments out on an epifluorescent microscope. Dr Delalez carried out the analysis of the intensity spots to determine the number of stators at stall.*)

There are two variants of the magnetic bead-filament assay, one of which expresses fluorescent stators and the other does not. For this experiment, I have used the magnetic bead-filament assay in which the cells are capable for expressing fluorescent stators. This assay will allow me to investigate the number of stators present at the motor during stall. 1 μm streptavidin-coated superparamagnetic SiO_2 beads (Microparticles GmbH) were used due to their relatively low auto-fluorescence compared to the other superparamagnetic polystyrene beads presented in Table 4.1. The bacterial strain used, JPA808, is capable of expressing not only cysteine residues on the filament but also GFP-tagged stators.

The magnetic bead-filament assay was prepared in the same manner as described

in the previous chapter, except that Dr Delalez would set the cells up from fresh stocks, as opposed to frozen stocks. The tunnel slide used was different and was made by sandwiching a 22 mm by 22 mm glass-coverslip with a standard microscope slide and held together using double-sided sticky tape. The tunnel slide was placed on an epifluorescent microscope operated by Dr Delalez. I was responsible for stalling the motors by bringing a pair of neodymium magnets close to the slide. A metre rule was used to measure the distance between the face of the magnets and the specimen which was usually between 15 mm and 20 mm. We used this measure to determine the magnitude of magnetic field required to stall the motor which was between 20 mT and 30 mT. 50 to 100 video frames of the fluorescent spots were recorded and fluorescent spot intensity during stall events were calculated as described in Leake *et al.* (2006) and Tipping *et al.* (2013b).

Figure 4.1 shows a representative time-course image of two flagellar motors driving the magnetic bead. Motors were allowed to rotate freely and were stalled for 300s using a pair of neodymium magnets.

Intensities of the fluorescent spot before and after stall for five motors were then compared and shown in Table 4.1. The results obtained showed that three motors with initial fluorescence intensities close to the maximum observed retained similar values after stall. The remaining two motors which were less bright before stall increased in intensity to a similar maximum level during stall. This observation suggests that those motors lacking a full complement of stators while freely rotating recruited a full complement after stall. This result shows that the rotation of the motor is not required for stators to bind to the motor. This has led us to believe that stator mechanosensing is not a direct function of rotation but of torque output.

This was an important result obtained as it allowed us to complete our investigation into the load-dependence assembly behind the bacterial flagellar motor. One of the key results from this study is the graph of fluorescence spot intensity plotted

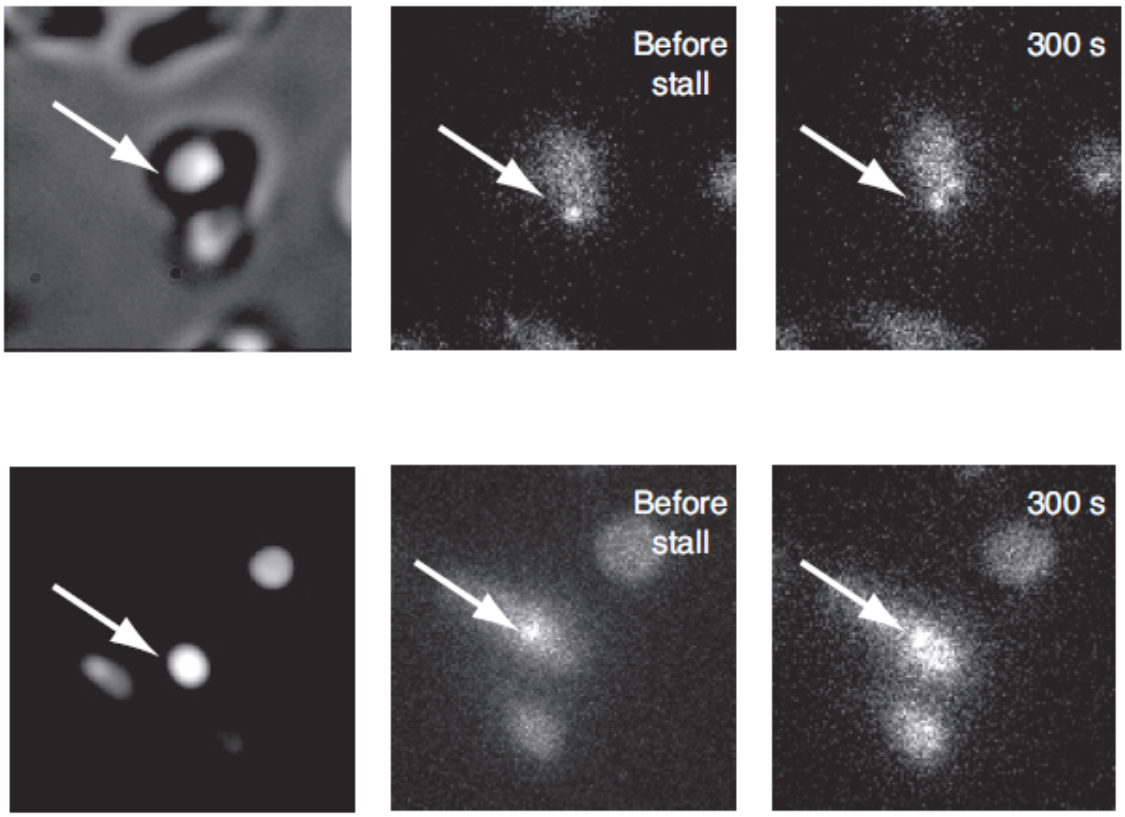

Figure 4.1. Time-course images of two motors driving 1 μm superparamagnetic SiO_2 beads, taken from Tipping *et al.* (2013b). Motors were allowed rotate freely before being subjected to a stall for a duration of 300 s under the application of an external magnetic field. The intensities of the spot measured was used to compare the number of stators before and during stall.

	Brightness (arbitrary units) or % difference				
Parameter	Cell 1	Cell 2	Cell 3	Cell 4	Cell 5
Before stall	12,309	9,830	10,068	6,401	7,770
300 s after stall	12,534	11,343	11,326	10,926	11,148
Difference (%)	+1.8	+15.4	+12.5	+70.7	+43

Table 4.1. Brightness of motor spots in five cells driving 1 μm superparamagnetic SiO_2 beads before stall and 300s after stall using an external magnetic field.

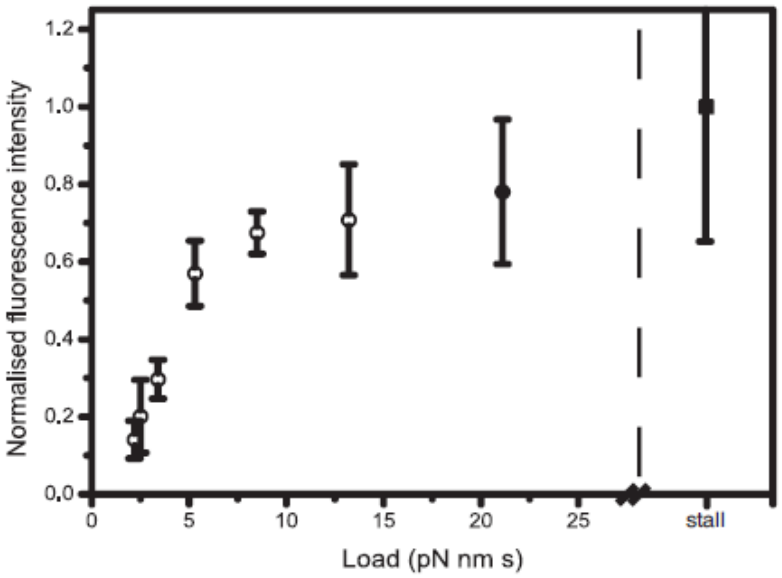

Figure 4.2. Fluorescence spot intensity plotted against external load. All the data points, except that taken at stall, were obtained using fluorescent spot intensities of stators from polystyrene bead assays of different diameters. These experiments were carried out by Dr Murray Tipping.

against external load shown in Figure 4.2. The graph shows that the number of stators bound to the flagellar motor depends on external load. Fewer stators are bound to the motor at lower loads and it can be inferred that the average number of stators near zero load may be close to zero.

The observation of reduced stator number at low load is significant for the interpretation of experiments in which torque-speed curves of the motors were obtained in bulk. Furthermore, this result necessitates the need for fast torque-speed measurements from single motors at a time scale slower than that of stator exchange.

4.2 Magnetic bead-hook assay

There are two main aims for the experiments carried out in this section. The first aim is to investigate the effect that a rotating magnetic field has on the orbital trajectories of the bead assay. The second aim is to find out if it is possible to determine torque

in terms of the angle between the easy axis of the bead and the magnetic field, $\Delta\theta$. In order to determine this angle, the offset between the bead angle measured and the easy axis of the bead must first be estimated.

In this section, magnetic torque was delivered to magnetic bead-hook assays located at the centre of the field-of-view of the imaging system. Each assay consisted of a cell capable of endogenously expressing biotin at the hook (MTB32) to which a streptavidin-coated 1 μm Dynabeads MyOne T1 superparamagnetic beads was attached. These cells are capable of switching the direction of their flagellar motor rotation. The assays were subjected to a magnetic field rotating in the CCW direction and CW directions at different frequencies. The direction the magnetic field is defined in the same handedness as that of the rotating bead assay.

Mk IIb and a dry condenser lens from Nikon having a numerical aperture of 0.85 were the electromagnet and condenser used respectively for experiments carried out on the magnetic bead-hook assay. I also wrote the programs to carry out the different experimental protocols. Preliminary analysis of the data collected was initially done using programs written in LabVIEW and the graphical outputs were generated using scripts written in MATLAB.

4.2.1 Counter-clockwise rotation

All the results presented here were obtained from the application of a rotating magnetic field in the CCW direction at different frequencies on the same magnetic bead-hook assay called Cell A. The angle of the bead was determined from the X-Y signals measured using BFP interferometry and the angle of the magnetic field, θ_{magnet}, was determined from the measurements of the current flowing through each of the load resistor. All these signals were sampled at 10,000 points per second.

An attempt to determine the offset between the angle of the bead and its easy axis was carried out by rotating the magnetic field at a frequency equal to the resting

speed of the motor, i.e. the rotational speed of the motor in the absence of a magnetic field. It is noted that the resting speed is not equivalent to the free-swimming speed of the motor as the attachment of a micron-sized bead attached to the hook introduces a relatively large viscous drag on the motor compared to the drag of freely-rotating filaments. The motor speeds of free-swimming cells from different species have been observed to rotate at speeds between 100 Hz and 400 Hz (Sowa & Berry, 2008).

The magnetic field should impose no torque on the motor and we would expect $\Delta\theta = 0$. The details of this experiment, called resting-CCW experiment, are as follows:

- The electromagnet was switched off between $t = 0.0$ s and $t = 0.5$ s.
- The electromagnet was switched on between $t = 0.5$ s and $t = 1.5$ s at a frequency equal to the resting speed of the motor. An "easy" start-up procedure was implemented for the inputs into the amplifier in which the magnitude of first cycle of the input is increased proportional to time, i.e. the magnitude starts at zero and increases to the specified input current in one cycle. Such a start-up helps minimise high frequency content that is associated with a sudden input into the amplifier.
- A wind-down procedure is carried out in the form of 10 revolutions at 100 Hz in which the magnitude of the currents is decreased exponentially. This helps to remove any magnetic remanence that is present in the pole pieces. The electromagnet remained switched off for the remainder of the experiment.
- Ellipse fitting was carried out on blocks of data 0.10 s long. The transformed signals were then converted into polar form before being passed through a spectral analyser. The time resolution was chosen to be 0.05 s while the spectral resolution was 1 Hz. These parameters were used to obtain fitted angles and the speed-time traces for the remainder of this sub-section.

- The offset between the angle of the bead and its easy axis was estimated such that the mean of $\Delta\theta = \theta_{\text{bead}} - \theta_{\text{magnet}}$ in the window when the electromagnet was switched on is close to zero. θ_{bead} represents the angle of the easy axis of the bead.

We believe that an ideal spinner will trace out a perfect circle when rotating about the axis of the motor and so only spinners with almost perfect circular orbits were selected. This is important as it ensures that the plane of the orbit coincides with both the imaging plane of the microscope and the rotating magnetic field.

Figure 4.3 shows the X-Y trace for the resting-CCW experiment in which the resting speed of the motor was 52 Hz. A positive speed indicates that the motor is rotating in the CCW direction and a negative speed is used for rotations in the CW direction. I would like to note that the X-Y span the full range of the linear regime previously calibrated for the system so angular interpretations of data collected at the extreme of this regime have to be treated with caution. Nonetheless, observations obtained from speed-time traces are still valid.

The full trace in the figure shows two distinct orbital trajectories for the rotating magnetic bead-hook assay and the subfigures show that the orbital trajectory of the assay depended on whether the electromagnet was switched on or off. This observation shows that the presence of a rotating magnetic field affects the orbital trajectory of the assay even when the magnetic field was rotating at a frequency equal to the resting speed of the motor.

Figure 4.4 shows the magnitude of the magnetic vector, the X-Y and the rotational speed of the motor with time for the duration of the resting-CCW experiment. The plot of X-Y with time shows that the X-Y signals drifted when the electromagnet was switched on, further evidence that the rotating magnetic field affects the orbital trajectory of the bead. The trajectory when the electromagnet was switched on is just within the linear regime. The speed-time trace shows that the motor did not

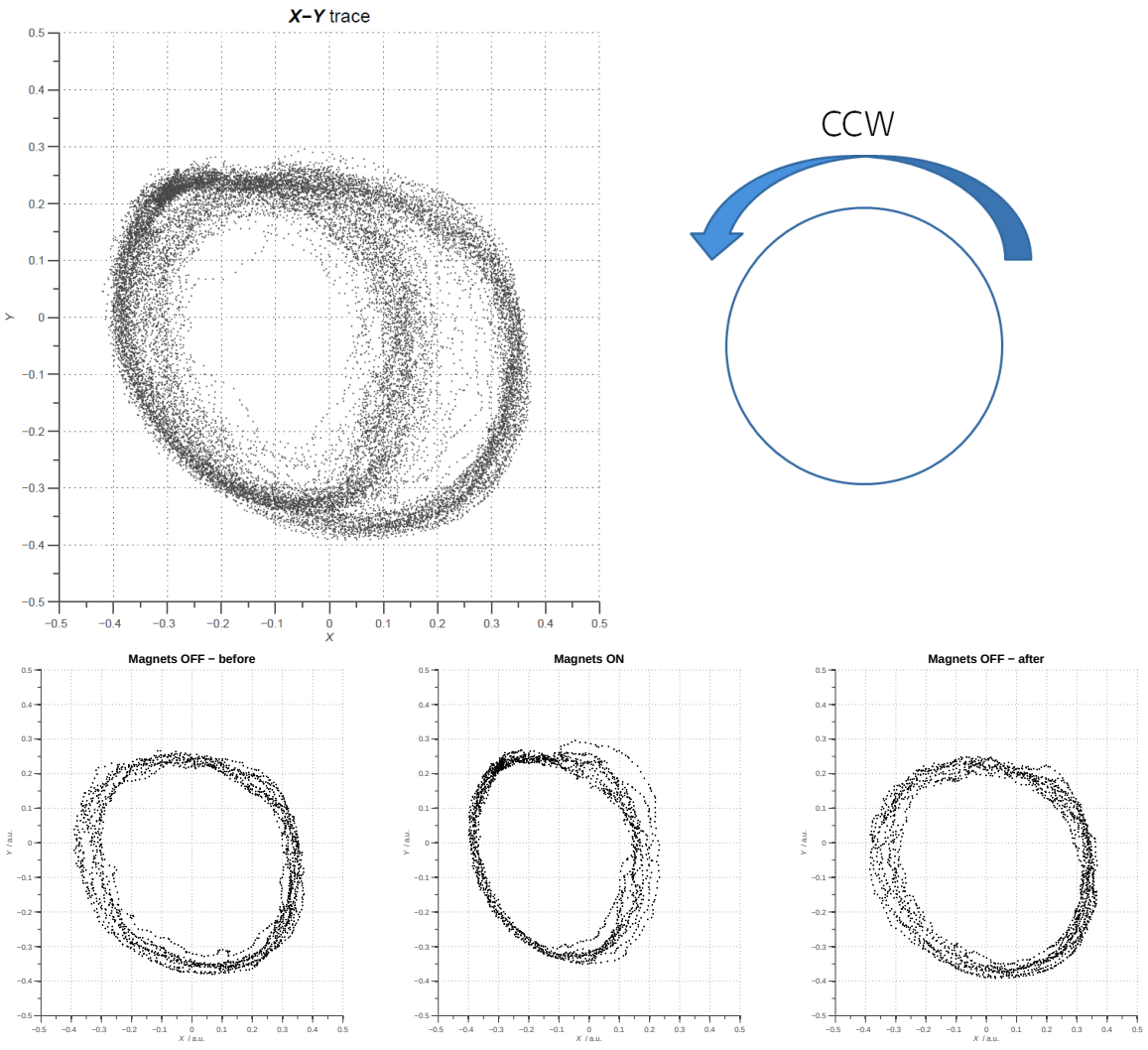

Figure 4.3. *X*-*Y* trace for the resting-CCW experiment carried out on Cell A. The **(top left)** subfigure shows the full trace taken over 2.0 s and *top right* is a schematic of the direction of the trajectory of the trace. The direction of the rotation of the trajectory for the bead is the same as that looking down the flagellum towards the motor. A motor rotating in the CCW direction will trace a CCW path on the QPD. The **(bottom)** subsidiary subfigures show the trace obtained over 0.2 s when the electromagnet was switched on, and when it was switched off before and after it was switched on. The resting speed of the motor was 52 Hz and the motor did not switch at any time during this experiment. The radii of the orbit are approximately between 300 nm and 320 nm, determined using the transfer function measured previously for the y-channel (0.17 a.u. per 100 nm).

switch during the duration of this experiment and the motor followed the magnetic field even during the wind-down procedure.

Plots of the raw angles for θ_{bead}, θ_{magnet} and $\Delta\theta$ with time and are shown in Figure 4.5. The offset estimated using the method outlined above is $-123.4°$. $\Delta\theta$ is observed to follow a large variation, easily spanning about $90°$ in one revolution. This indicates that the magnetic bead experiences varying torque within one revolution and could be due to several reasons. The most plausible reason for this varying torque is the change in relative orientation of the easy axis with the motor as the bead goes around the motor. Even though I have attempted to align the beads in the plane of the glass coverslip using a pair of Helmholtz coils, I have no control on the final orientation of the bead and its point of attachment to the hook. The bead's easy axis may not be following the magnetic field in the same plane of rotation which will result in the delivery of different amounts of torque at different angles. Segmented angular analysis is strongly encouraged for future data analysis. The other possible reason for this varying torque is the inhomogeneity in the rotating magnetic field, a factor which I could not account for due to the inavailability of a Gaussmeter with AC capability at the time these experiments were carried out.

There is a decreasing drift in $\Delta\theta$ during the wind-down procedure showing that the mean $\Delta\theta$ increase in magnitude when the assay is driven faster near 100 Hz. Figure 4.6 shows a close-up of the same dataset spanning a window of 0.1 s. It can be seen that are occasions when θ_{bead} would lead θ_{magnet} and vice versa. In addition, there are slow angles of θ_{bead} between $0°$ and $30°$.

Figure 4.7 shows plots of ellipse-fitted angles for θ_{bead}, θ_{magnet} and $\Delta\theta$ with time. It is assumed that the bead of an ideal spinner will trace out a perfect circle when rotating about the axis of the motor. The piezo-stage was manually moved such that the most circular trajectory was obtained at the resting speed. Even so, an ellipse fitting procedure was carried out on blocks of data 0.10 s long to remove any

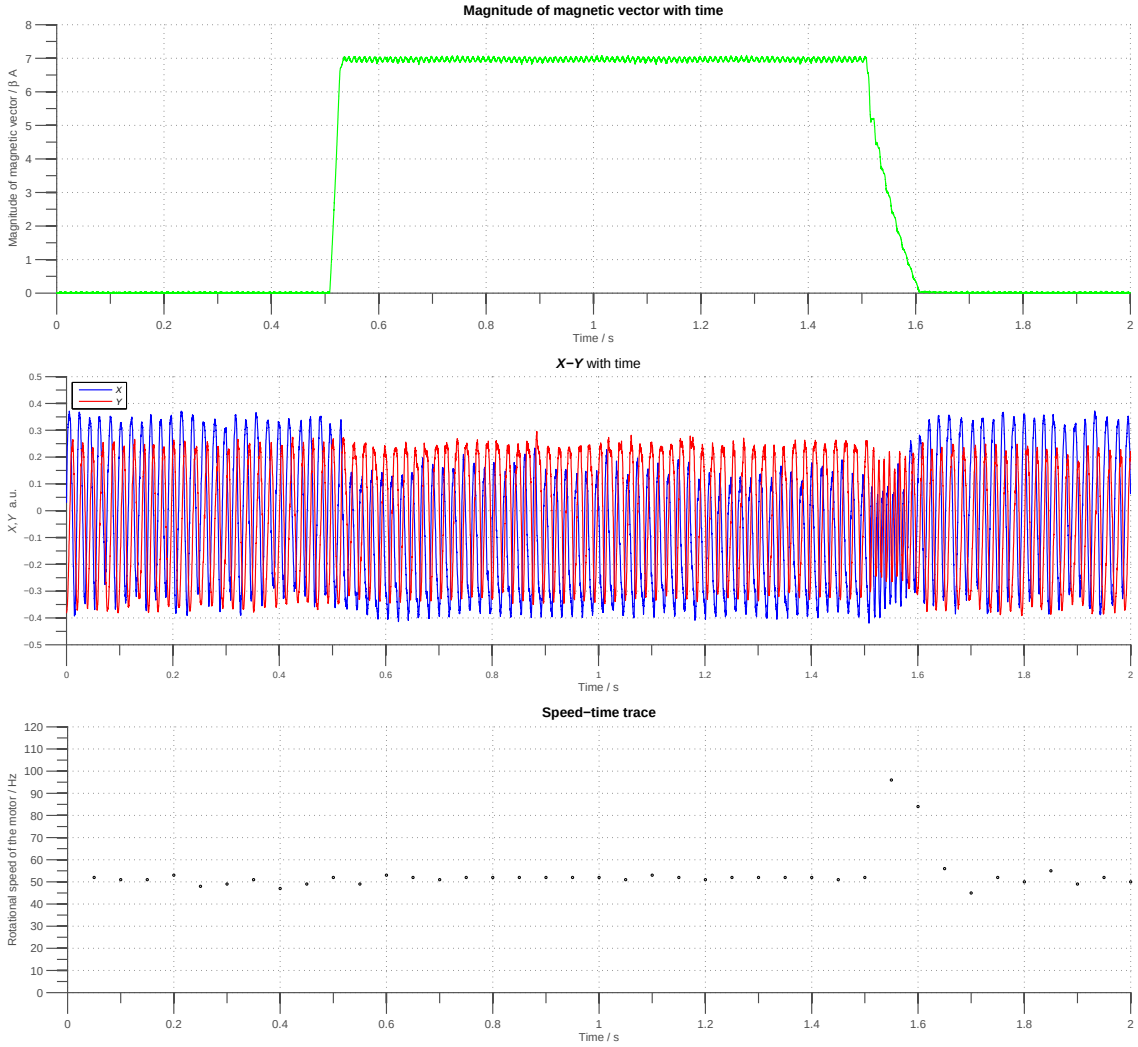

Figure 4.4. Resting-CCW experiment - Cell A. Plots of **(top)** magnitude of the magnetic vector with time, **(middle)** X-Y with time, and **(bottom)** rotational speed of the motor with time. Ellipse fitting was carried out over 0.10 s block of data before feeding the transformed polar signals to a spectral analyser. The time resolution for the speed-time trace was 0.05 s.

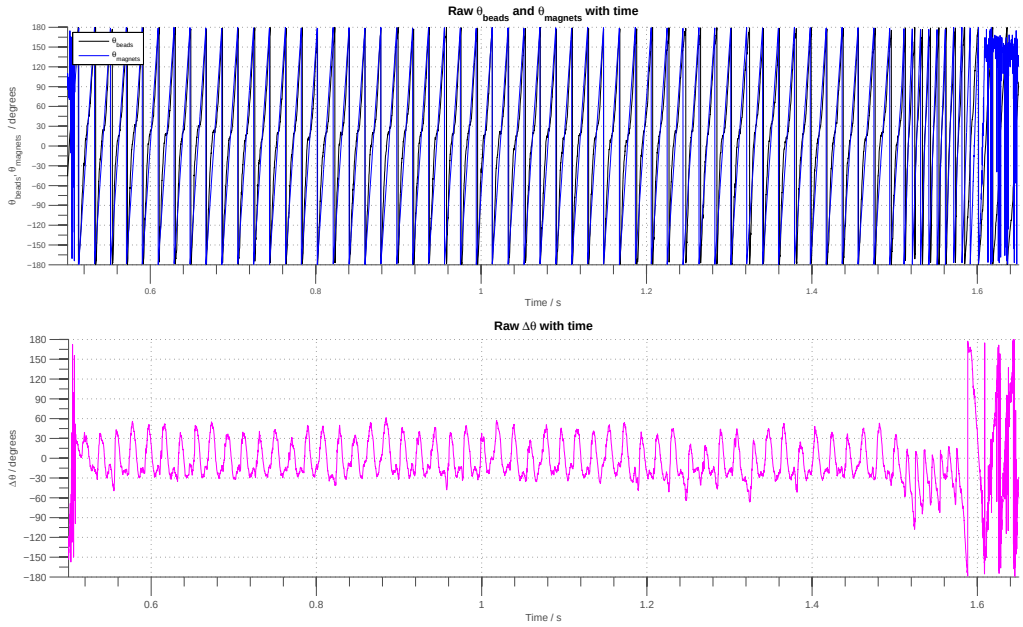

Figure 4.5. Resting-CCW experiment - Cell A - raw angular data. Plots of **(top)** the raw θ_{bead} and θ_{magnet} with time, and **(bottom)** raw $\Delta\theta$ with time. $\Delta\theta = \theta_{\text{bead}} - \theta_{\text{magnet}}$ and the offset between the bead angle measured and its easy axis was adjusted such that the mean of $\Delta\theta$ was close to zero in the window when the electromagnet was switched on. Offset $= -123.4°$.

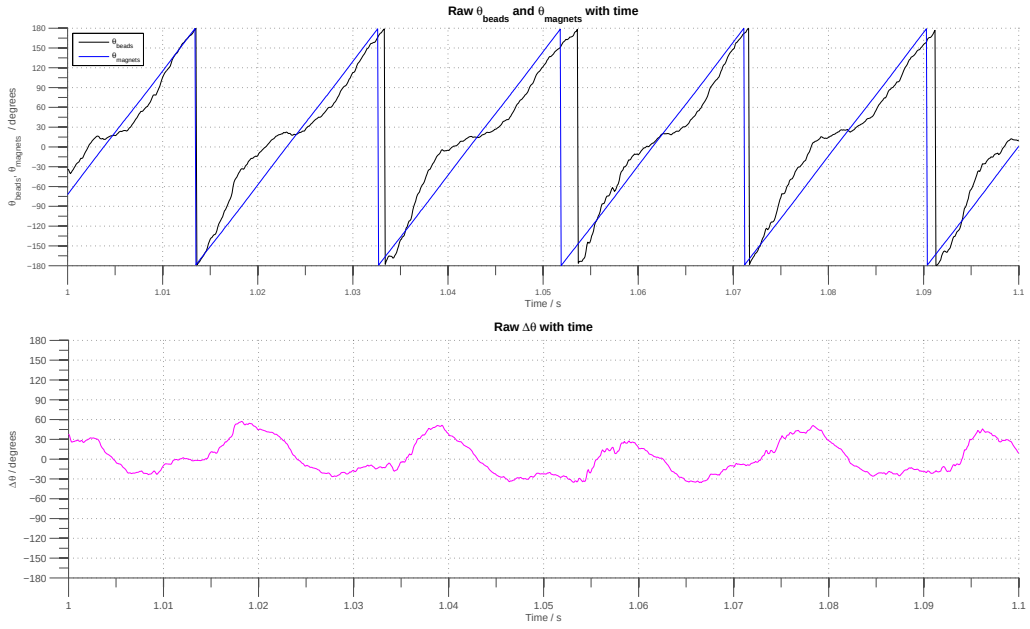

Figure 4.6. Resting-CCW experiment - Cell A - raw angular data. **(Top)** Plot of the raw θ_{bead} and θ_{magnet} with time in a shorter window spanning 0.1 s. **(Bottom)** Plot of the raw $\Delta\theta$ with time in a shorter window spanning 0.1 s. Offset is the same as that quoted in the previous figure and the mean $\Delta\theta = -0.1°$ for this window.

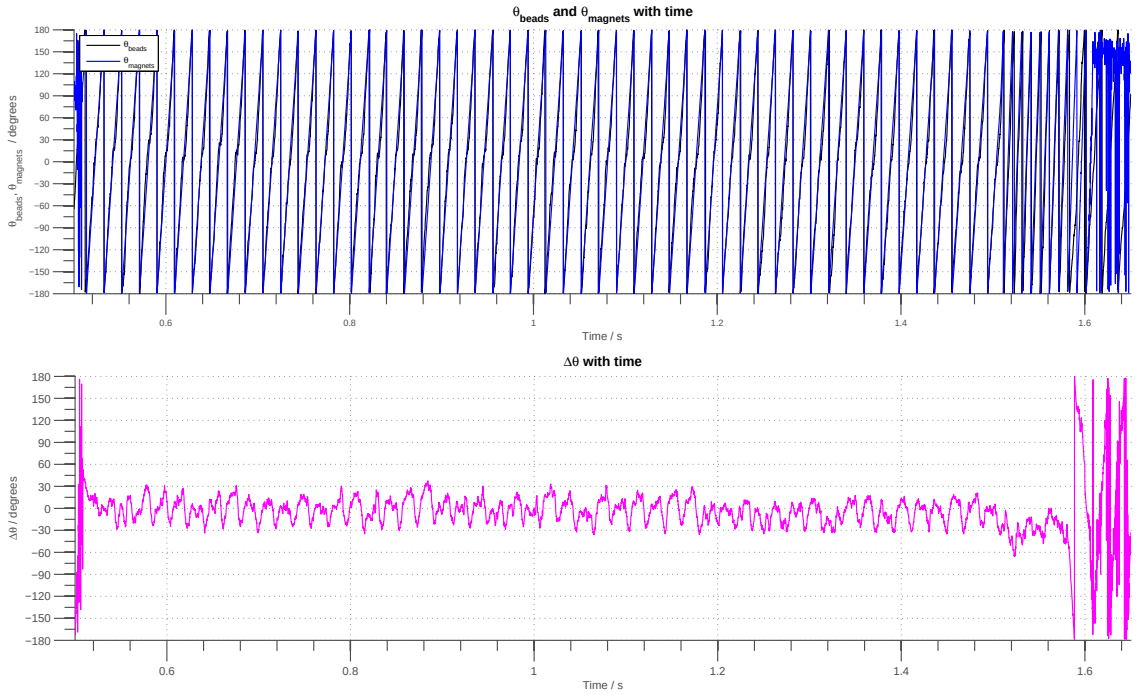

Figure 4.7. Resting-CCW experiment - Cell A - Ellipse-fitted angles. Plots of **(top)** θ_{bead} and θ_{magnet} with time, and **(bottom)** $\Delta\theta$ with time. Offset = $-121.0°$.

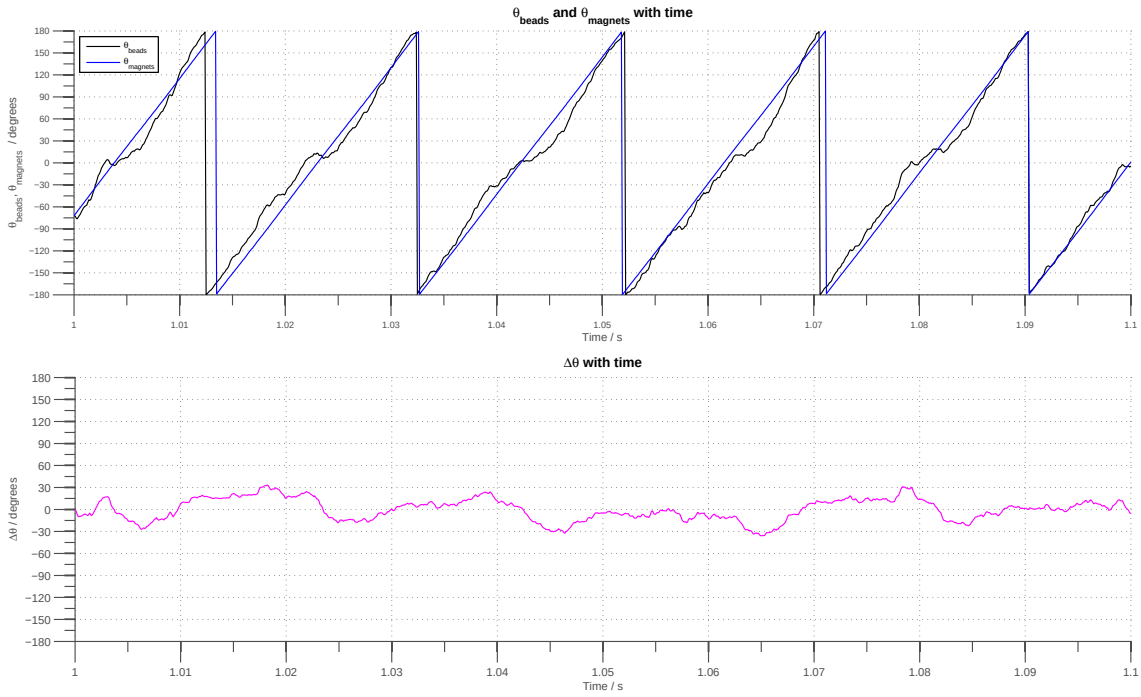

Figure 4.8. Resting-CCW experiment - Cell A - Ellipse-fitted angles. **(Top)** Plot of the θ_{bead} and θ_{magnet} with time in a shorter window spanning 0.1 s. **(Bottom)** Plot of the $\Delta\theta$ with time in a shorter window spanning 0.1 s. Offset is the same as that quoted in the previous figure and the mean $\Delta\theta = 0.1°$ for this window.

eccentricity in the trajectory of the orbit. Beads that trace an elliptical path, such as spinners located near the edges of the bacterial cell confirmed using bright-field microscopy, were rejected as circularising the trajectory of these beads can lead to mis-representation of the angle of the bead. It is unlikely that elliptical trajectories can be obtained from the instrument or detector as the radius of the orbital trajectory is well within the linear regime (usually between 200 nm and 300 nm).

The offset between the angle of the bead and its easy axis, determined in the same manner described previously, has changed to $-121.0°$ which is a 2% change from the previous value. The variation of $\Delta\theta$ within one revolution is less than that determined using raw angles but still indicates that the bead experienced varying torque within one revolution. The drift in $\Delta\theta$ during the wind-down procedure is still observed.

Figure 4.8 shows a close-up of the same dataset spanning the same window as the previous close-up figure obtained for raw angles. It can again be seen that are occasions when θ_{bead} lead θ_{magnet} and vice versa. The slow angles are less obvious but are present between $0°$ and $15°$. The figures generated using ellipse-fitted angles are perceived to be cleaner than those generated using raw angles. As such, all plots of θ_{bead}, θ_{magnet} and $\Delta\theta$ with time will be generated using ellipse-fitted angles.

Following on from the resting-CCW experiment, various experiments were carried out to rotate the same bead assay at different speeds from 10 Hz up to 200 Hz at intervals of 10 Hz. The details of an experiment carried out at 20 Hz, called 20 Hz-CCW experiment, are as follows:

- The electromagnet was switched off between $t = 0.0$ s and $t = 0.5$ s.
- The electromagnet was switched on between $t = 1.0$ s and $t = 2.0$ s at a frequency equal to the resting speed of the motor. This is an important step to determine the offset between the angle of the bead and its easy axis. An "easy" start-up procedure was implemented for the first cycle.

- The electromagnet was switched on between $t = 2.0$ s and $t = 6.0$ s at 20 Hz.
- A wind-down procedure was carried out in the form of 10 revolutions at 100 Hz in which the magnitude of the currents is decreased exponentially. The electromagnet remained switched off for the remainder of the experiment.
- Fitting parameters and the method to determine offset between the angle of the bead and its easy axis were the same as before.

Figure 4.9 shows the X-Y trace for the 20 Hz-CCW experiment in which the resting speed of the motor has increased to 54 Hz. The possible orbital trajectories are not distinctively clear from the full trace. Nonetheless, the subfigures show that the orbital trajectory depended on whether the electromagnet was switched on or off, and the frequency of the magnetic vector when the electromagnet was on.

The speed-time trace of the rotational speed of the motor with time shown in Figure 4.10 reveals that the motor did not switch during the duration of this experiment. The plot of $\Delta\theta$ with time in the same figure showed that there is a distinct change when the rotational frequency of the magnetic field decreased from the resting speed of the motor to 20 Hz.

The offset adjusted was estimated to be equal to 59.0° which is 180° apart from the previous offset for the same bead. This indicates that the particle behaves in a similar manner to birefringent particles in a rotating linearly polarised field. There are two stable angles in which the particle experience the same amount of torque when following a rotating field. This is very different to the $\sin\Delta\theta$ behaviour of ferromagnetic particles in that there is only one stable angle in which the particle can follow a rotating field.

A close-up of the ellipse-fitted angles θ_{bead}, θ_{magnet} and $\Delta\theta$ over a period of 0.2 s is shown in Figure 4.11. The mean $\Delta\theta = 20.0°$ across this period of time, showing that the bead leads the magnetic field when it is rotated slower than the resting speed of

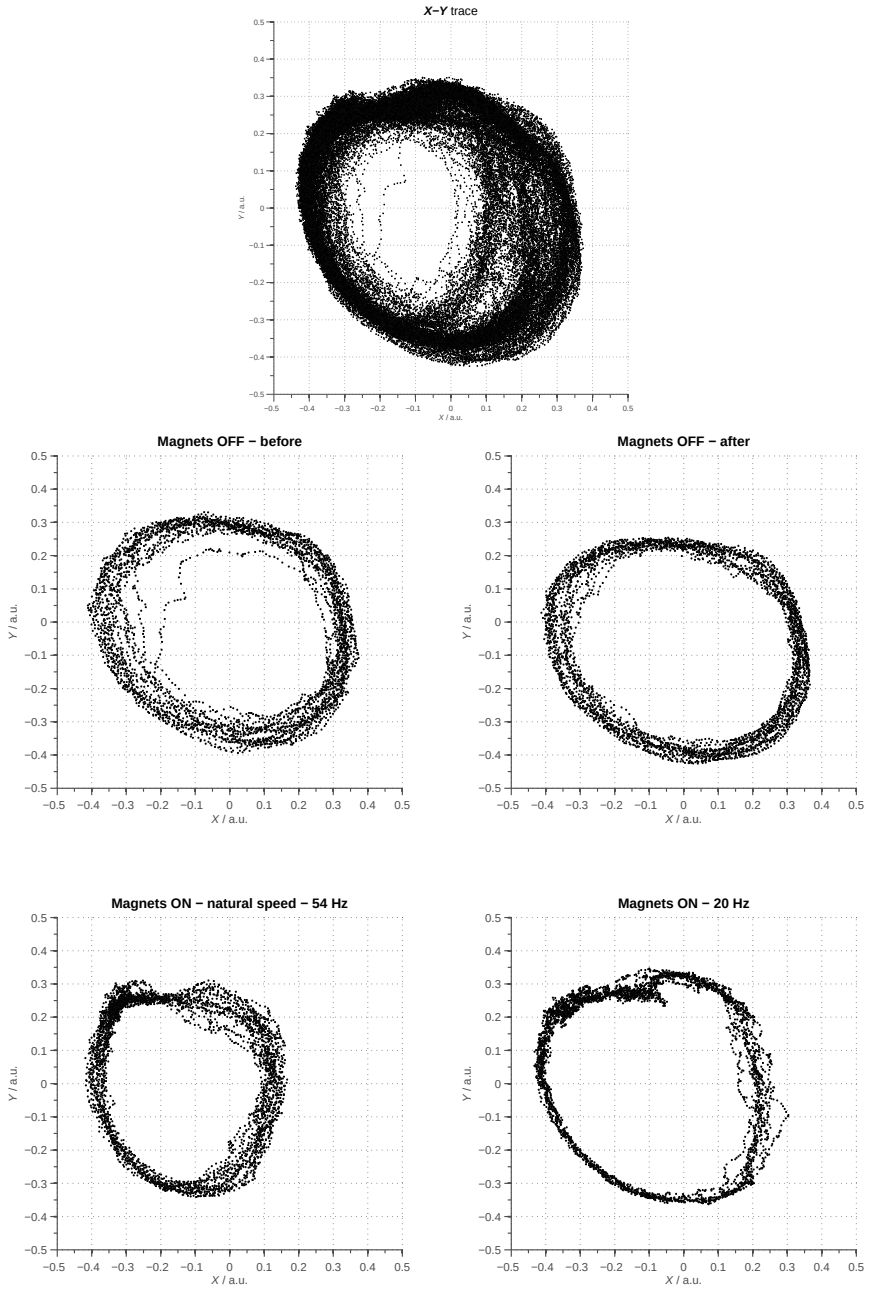

Figure 4.9. *X*-*Y* trace for the 20 Hz-CCW experiment carried out on Cell A. The **(top)** main subfigure shows the full trace taken over 7.0 s while the **(bottom)** subsidiary subfigures show the trace obtained over 0.4 s when the electromagnet was switched off before and after it was switched on, and when it was switched on at a frequency equal to the resting speed of the motor, and at 20 Hz. The resting speed of the motor was 54 Hz. The radii of the orbit are approximately between 300 nm and 320 nm, determined using the transfer function measured previously for the y-channel (0.17 a.u. per 100 nm).

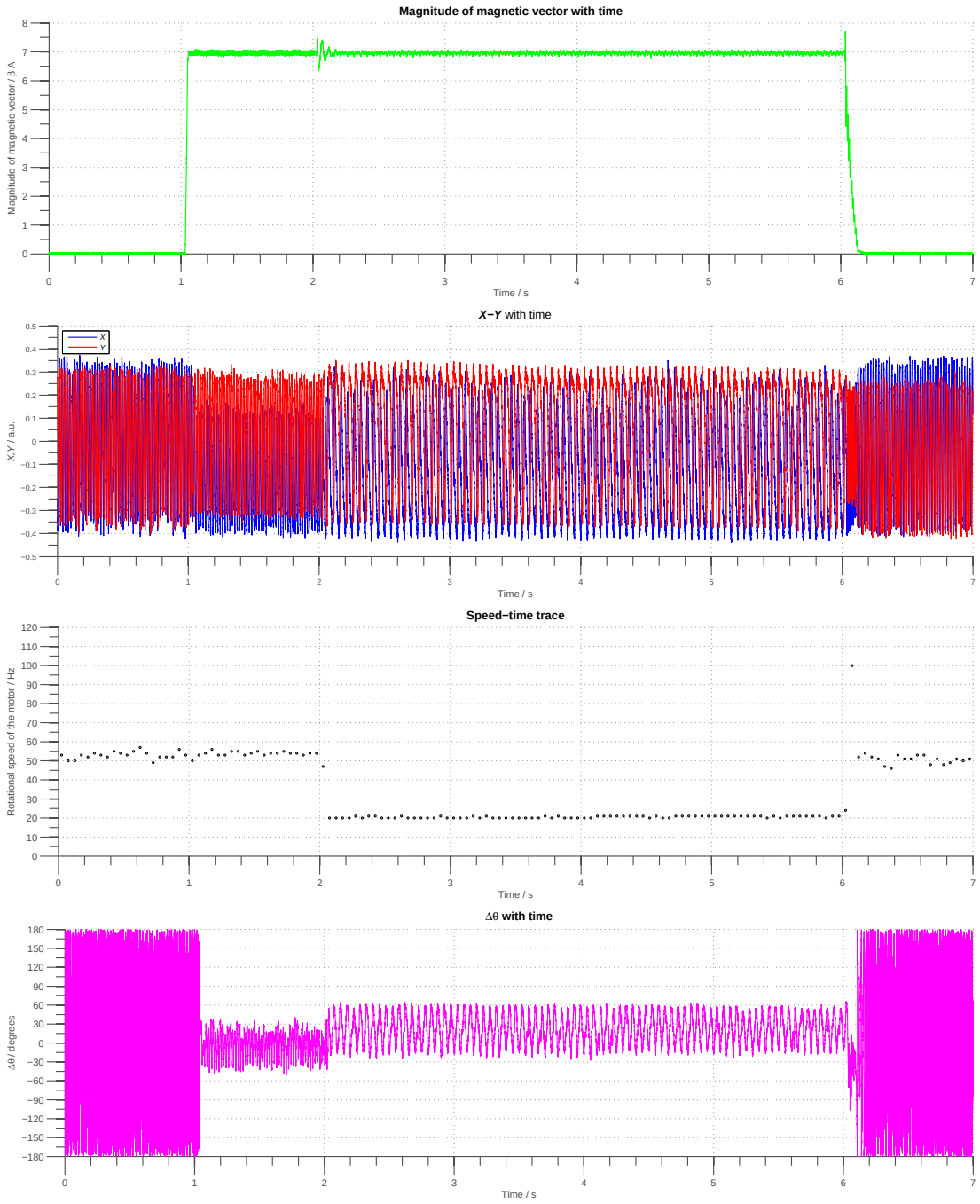

Figure 4.10. 20 Hz-CCW experiment - Cell A. Plots of **(top)** magnitude of the magnetic vector with time, **(middle top)** X-Y with time, **(middle bottom)** speed-time trace, and **(bottom)** $\Delta\theta$ with time where the offset = 59.0°.

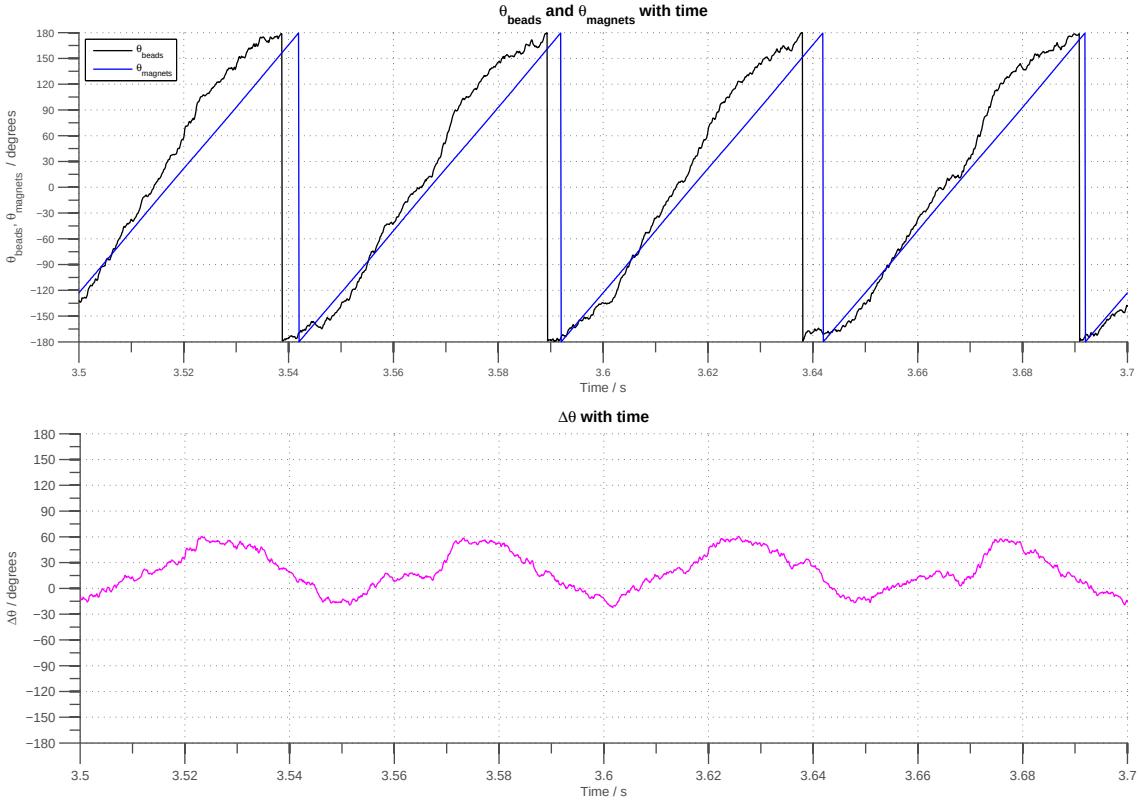

Figure 4.11. 20 Hz-CCW experiment - Cell A. Plots of **(top)** θ_{bead} and θ_{magnet} with time, and **(bottom)** $\Delta\theta$ with time, both shown over the same interval of time. Offset is the same as that quoted in the previous figure and the mean $\Delta\theta = 20.0°$ for this window.

the motor.

The highest frequency at which this assay was able to follow the field without slipping was 140 Hz. This result was shown in an experiment called 140 Hz-CCW whose details are the same as that for 20 Hz except that after the electromagnet was switched on at the resting speed of the motor and then at a frequency of 140 Hz. The results of this experiment are shown in Figures 4.12, 4.13 and 4.14.

The X-Y traces shows that the trajectory followed a smaller orbit when the magnetic field rotated at 140 Hz. This is likely due to a change in the orientation of the bead and height from the bacterial surface so that it can follow the field at that frequency. The speed-time trace shows that the motor did not attempt to switch during the duration of this experiment. When the magnetic field was set to rotate at a frequency of 140 Hz, $\Delta\theta$ shifted and became negative. The mean $\Delta\theta = -79.0^\circ$ in the window of time shown in Figure 4.14.

Slipping signatures began to appear in experiments in which the magnetic field rotated at frequencies above 140 Hz. The X-Y traces shown in Figure 4.15 revealed that the orbital trajectory was very different when the bead slipped when attempting to follow the magnetic field at 150 Hz. This is confirmed in the speed-time trace shown in Figure 4.16. At the slipping points, the speed of the motor decreased to that very close to the resting speed of the motor. Meanwhile the plot of $\Delta\theta$ with time again shows signature of the $\sin(2\Delta\theta)$ behaviour as there are two range of stable angles at which the bead followed the magnetic field. Plots for the angular data with time across 0.1 s in which the bead followed the magnetic field and the bead slipped are shown in Figures 4.17 and 4.18 respectively.

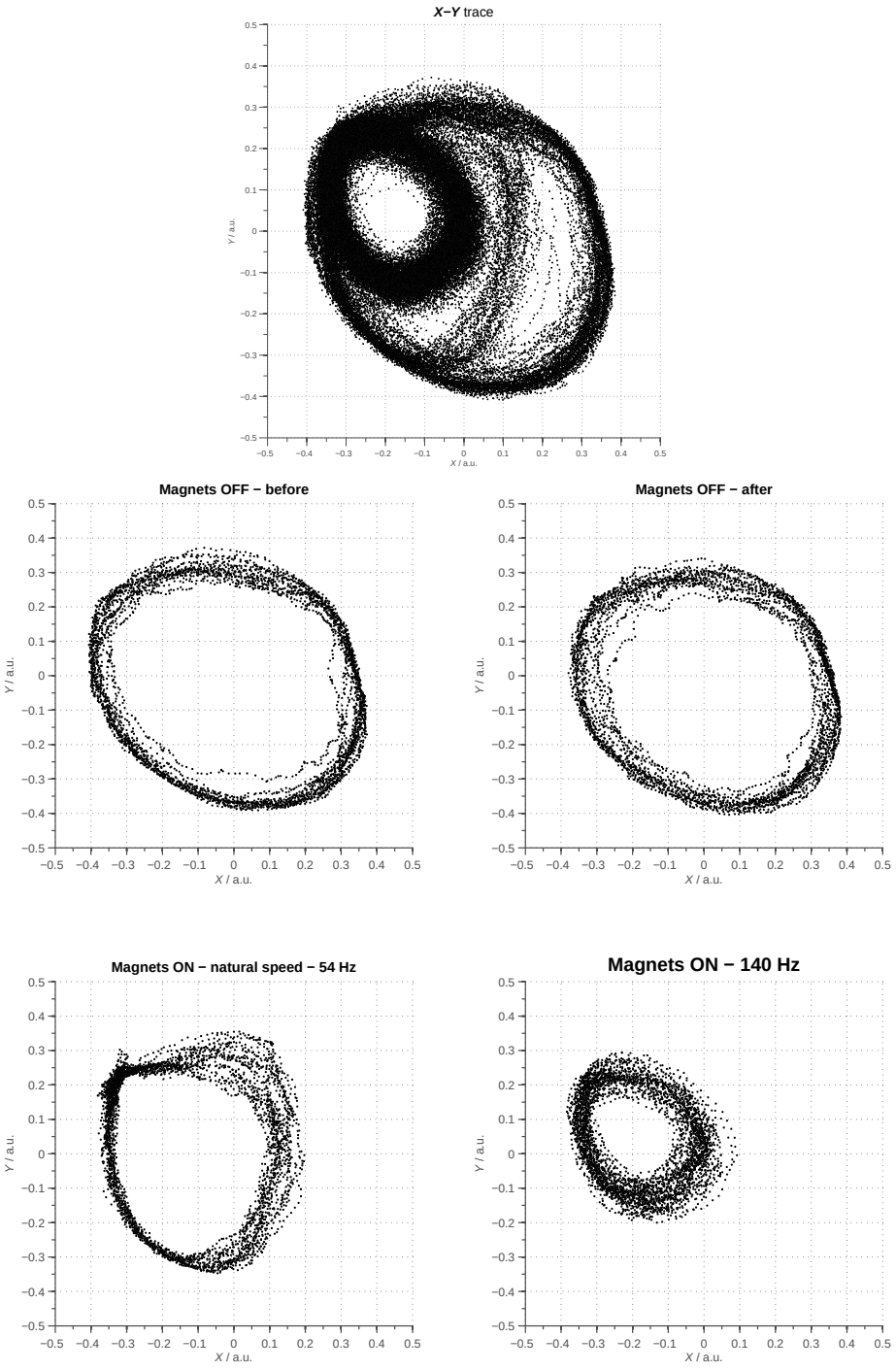

Figure 4.12. *X*-*Y* trace for the 140 Hz-CCW experiment carried out on Cell A. The **(top)** main subfigure shows the full trace taken over 7.0 s while the **(bottom)** subsidiary subfigures show the trace obtained over 0.4 s when the electromagnet was switched off before and after it was switched on, and when it was switched on at a frequency equal to the resting speed of the motor, and at 140 Hz. The resting speed of the motor was 54 Hz. The radius of the orbital trajectory when the bead was spun at 140 Hz is approximately 240 nm.

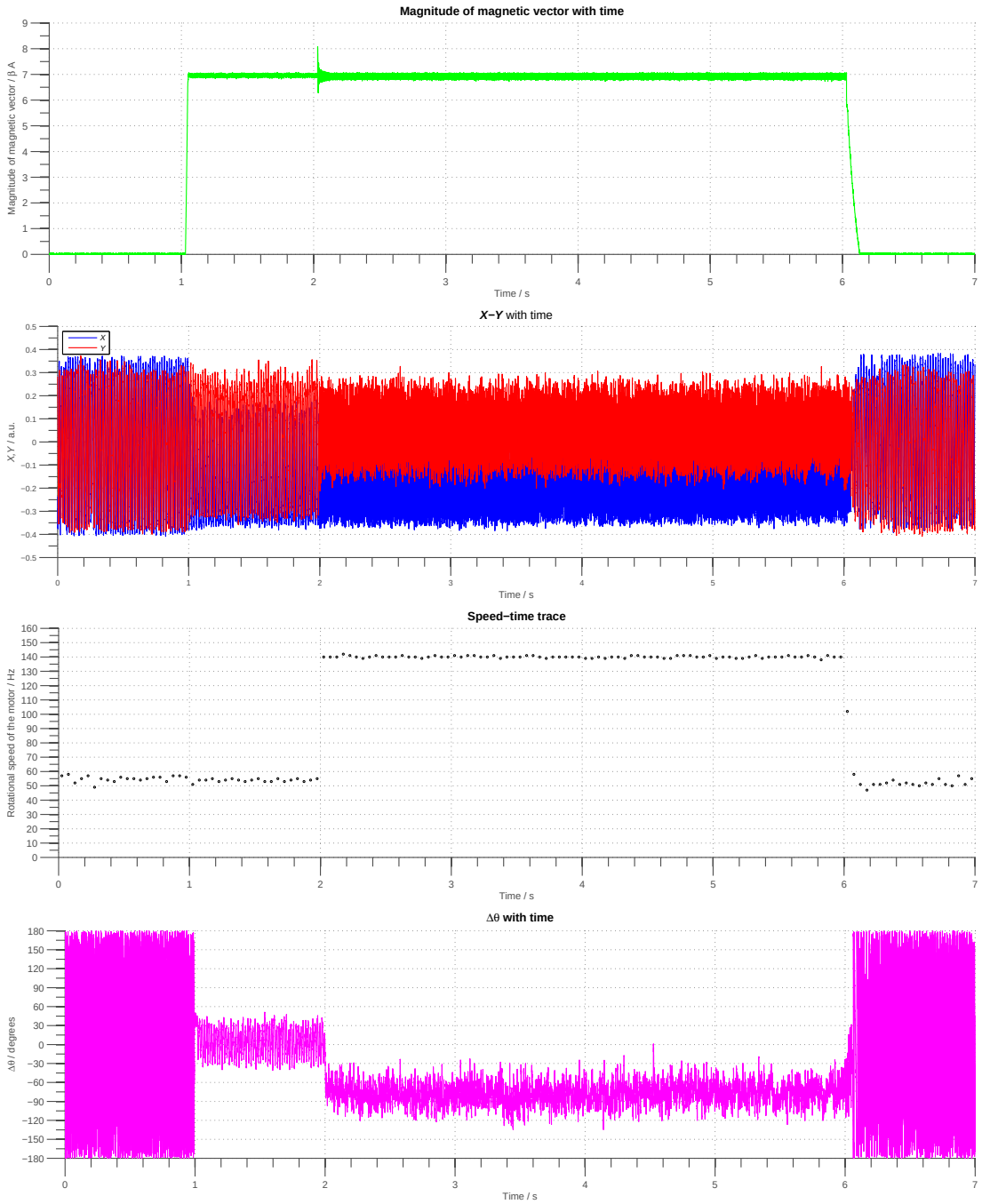

Figure 4.13. 140 Hz-CCW experiment - Cell A. Plots of **(top)** magnitude of the magnetic vector with time, **(middle top)** X-Y with time, **(middle bottom)** speed-time trace, and **(bottom)** $\Delta\theta$ with time where the offset = 59.0°.

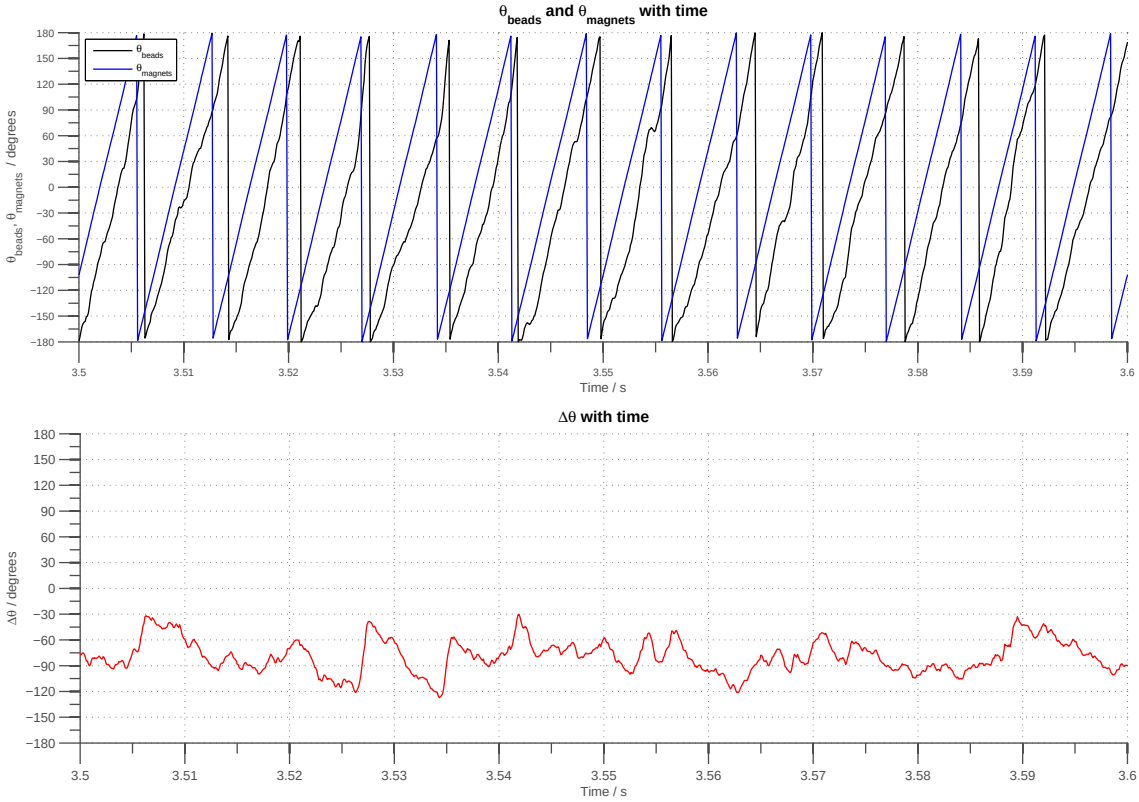

Figure 4.14. 140 Hz-CCW experiment - Cell A. Plots of **(top)** θ_{bead} and θ_{magnet} with time, and **(bottom)** $\Delta\theta$ with time, both shown over the same interval of time. Offset is the same as that quoted in the previous figure and the mean $\Delta\theta = -79.0°$ across this window.

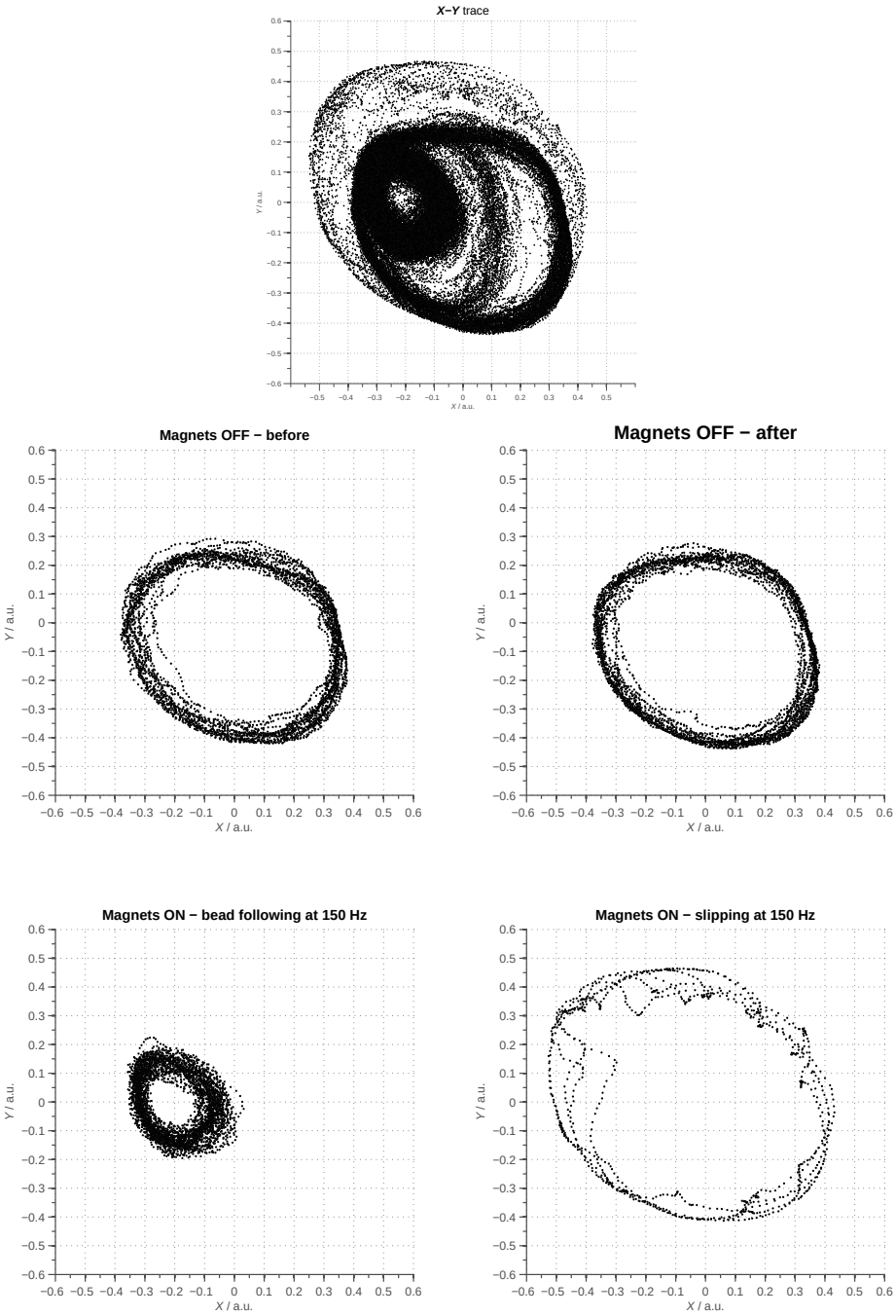

Figure 4.15. *X*-*Y* trace for the 150 Hz-CCW experiment carried out on Cell A. The **(top)** main subfigure shows the full trace taken over 7.0 s while the **(bottom)** subsidiary subfigures show the trace obtained over 0.4 s when the electromagnet was switched off before and after it was switched on, and when it was switched on at a frequency at 150 Hz in which the bead followed. The trace obtained in which slipping occurred was obtained over a 0.1 s. The resting speed of the motor was 50 Hz. The radius of the orbital trajectory when the bead was spun at 150 Hz is approximately 210 nm.

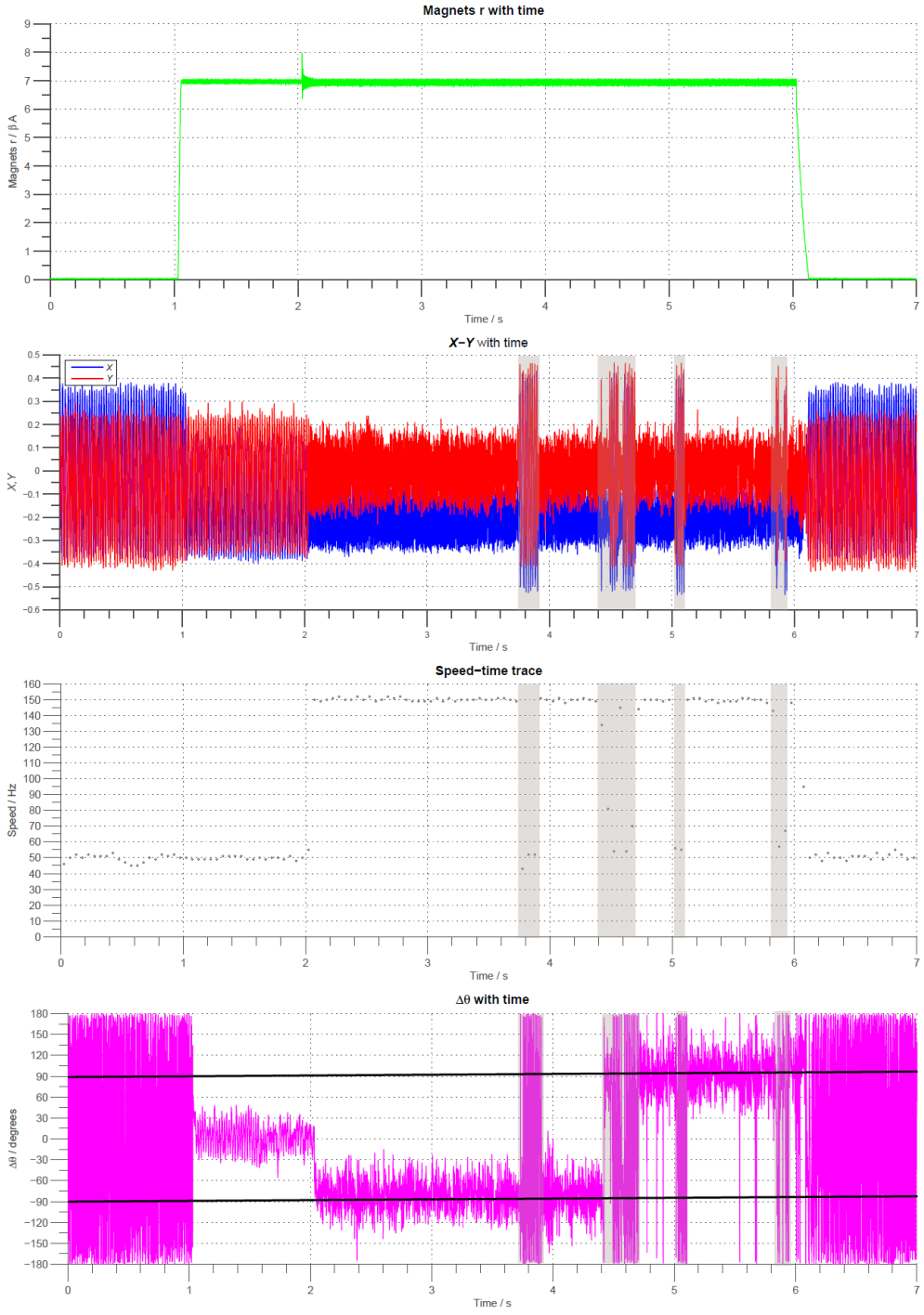

Figure 4.16. 150 Hz-CCW experiment - Cell A. Plots of **(top)** magnitude of the magnetic vector with time, **(middle top)** X-Y with time, **(middle bottom)** speed-time trace, and **(bottom)** $\Delta\theta$ with time where the offset = 59.0°. The regions shaded in grey indicate regions where slipping took place. There are two angles at which the bead, spaced 180° apart. This is an observation in agreement with the $\sin(2\Delta\theta)$ behaviour for superparamagnetic beads.

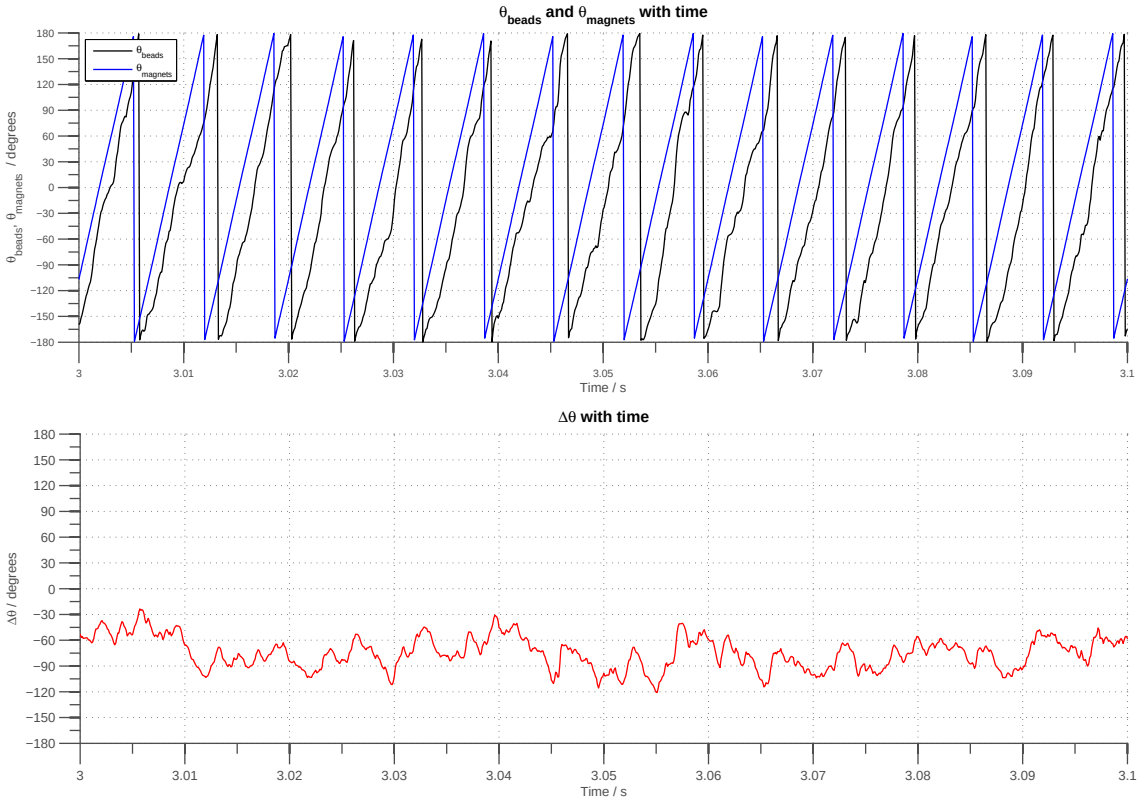

Figure 4.17. 150 Hz-CCW experiment - Cell A. **(Top)** Plots of **(top)** θ_{bead} and θ_{magnet} with time, and **(bottom)** $\Delta\theta$ with time, both shown over the same interval of time. Offset is the same as that quoted in the previous figure and the mean $\Delta\theta = -74.7°$ for this window.

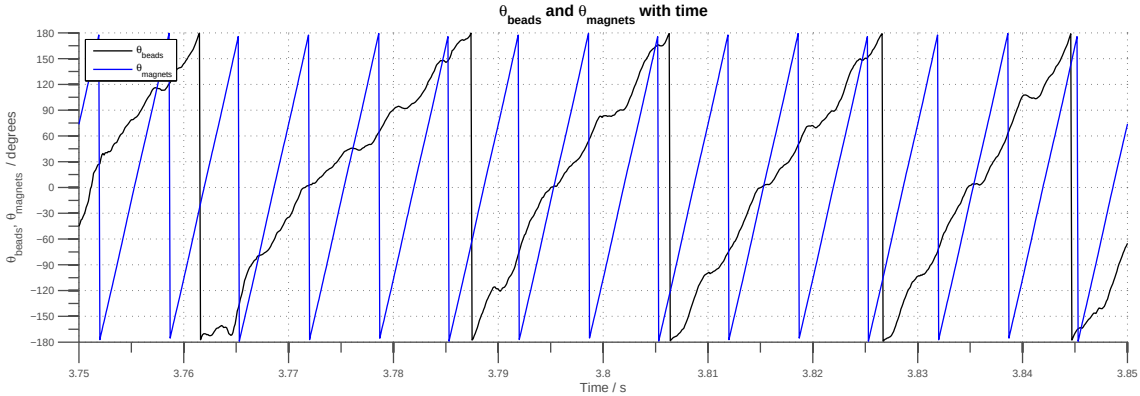

Figure 4.18. 150 Hz-CCW experiment - Cell A. Plot of θ_{bead} and θ_{magnet} over a period of 0.1 s in which slipping took place.

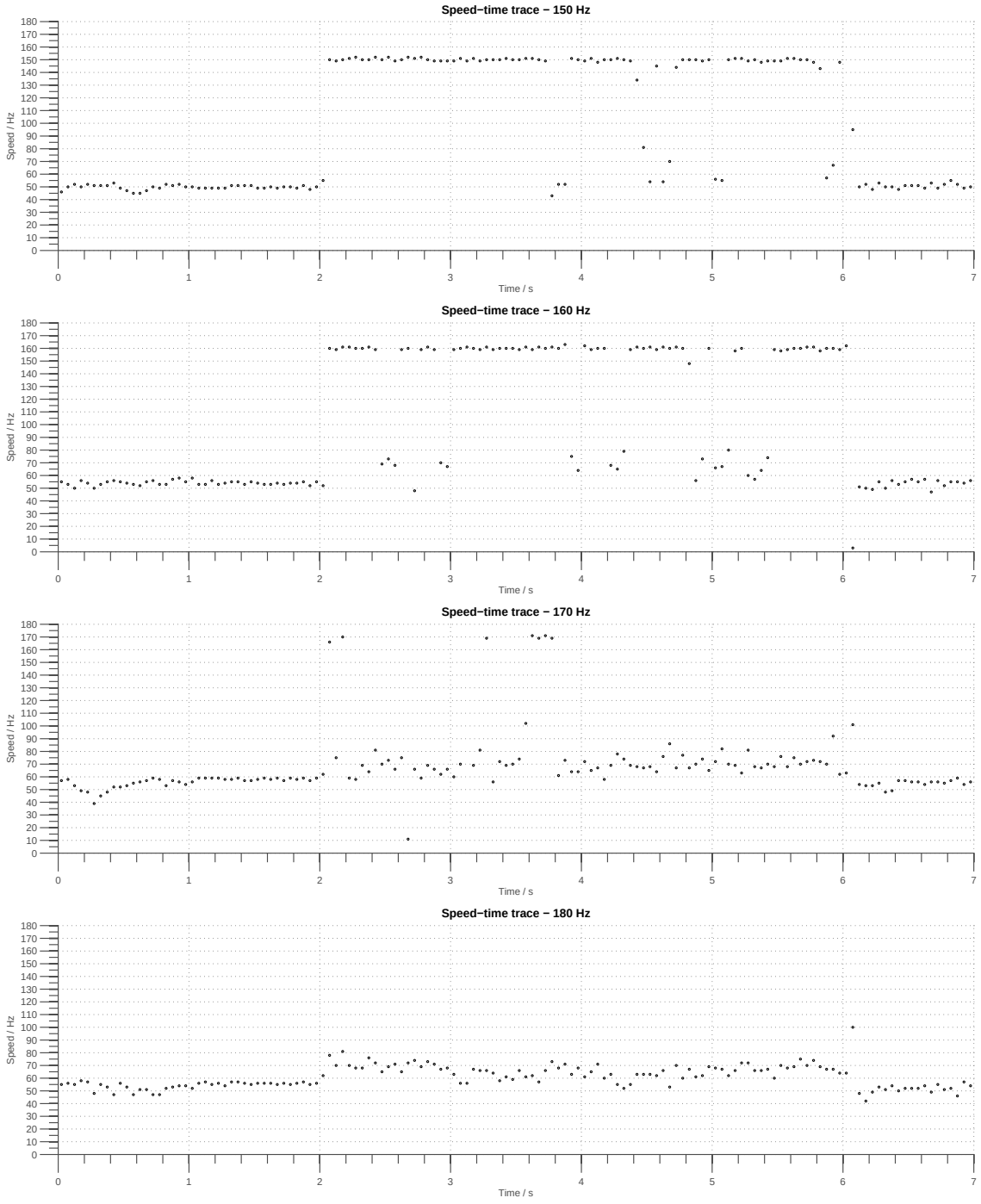

Figure 4.19. Speed-time traces in which experimental details are the same except that the frequency of the electromagnet was varied. It can be easily seen that the frequency of slipping events increase with increasing frequency. The bead is unable to follow the magnetic field at 180 Hz.

Speed-time traces shown in Figure 4.19 reveal how the frequency of slipping events increased with increase frequency at which the magnetic field rotates. The bead is unable to follow the magnetic field at 180 Hz.

The experimental results obtained in this sub-section showed that the orbital trajectories of the magnetic bead-hook assay change under the presence of the rotating magnetic field. Using this electromagnet, I was able to rotate the assay up to 140 Hz in the CCW direction. This speed however is not fast enough to explore the zero-torque behaviour of wild-type bacterial strains. The experiments carried out also showed that varying torque was delivered to the assay within every revolution. The varying torque complicates the ability to use $\Delta\theta$ as a measure of torque. Segmented angular analysis has to be carried out in order to take this project further. Plots of $\Delta\theta$ with time reveal that there are two possible angles at which the bead can follow the magnetic field. This observation is in agreement with a $\sin(2\Delta\theta)$ behaviour for superparamagnetic beads. This behaviour is attributed to the existence of an easy axis in the bead. The physics behind the rotation of such beads in the presence of a rotating magnetic-field is thus similar to that of birefringent particles in a rotating linearly polarised electric field.

4.2.2 Clockwise rotation

In this sub-section, I shall present results from experiments in which the magnetic bead-hook assay was driven in the clockwise direction in which I was interested in exploring the possibility of driving the cells backwards. All the experiments were carried out on one particular magnetic bead-hook assay called Cell B. A resting-CCW experiment was first carried out to determine the offset between the angle of the bead and its easy axis and to show the orbital trajectories when the motor was rotating in the CCW direction. The results of this experiment are shown in Figures 4.20 and 4.21. The offset $= 152.4^\circ$ is different from that obtained for Cell A.

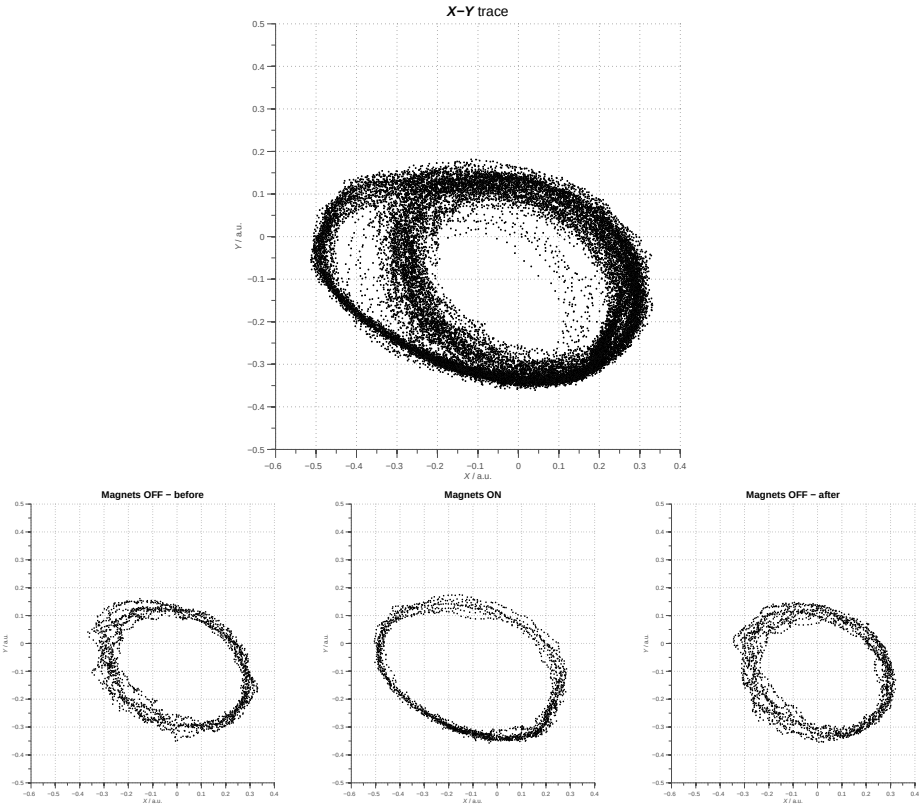

Figure 4.20. *X*-*Y* trace for the resting-CCW experiment carried out on Cell B. The **(top)** main subfigure shows the full trace taken over 2.0 s while the **(bottom)** subsidiary subfigures show the trace obtained over 0.2 s when the electromagnet was switched on, and when it was switched off before and after it was switched on. The resting speed of the motor was 44 Hz. The radii of the orbital trajectory ranged from approximately 240 nm up to 400 nm.

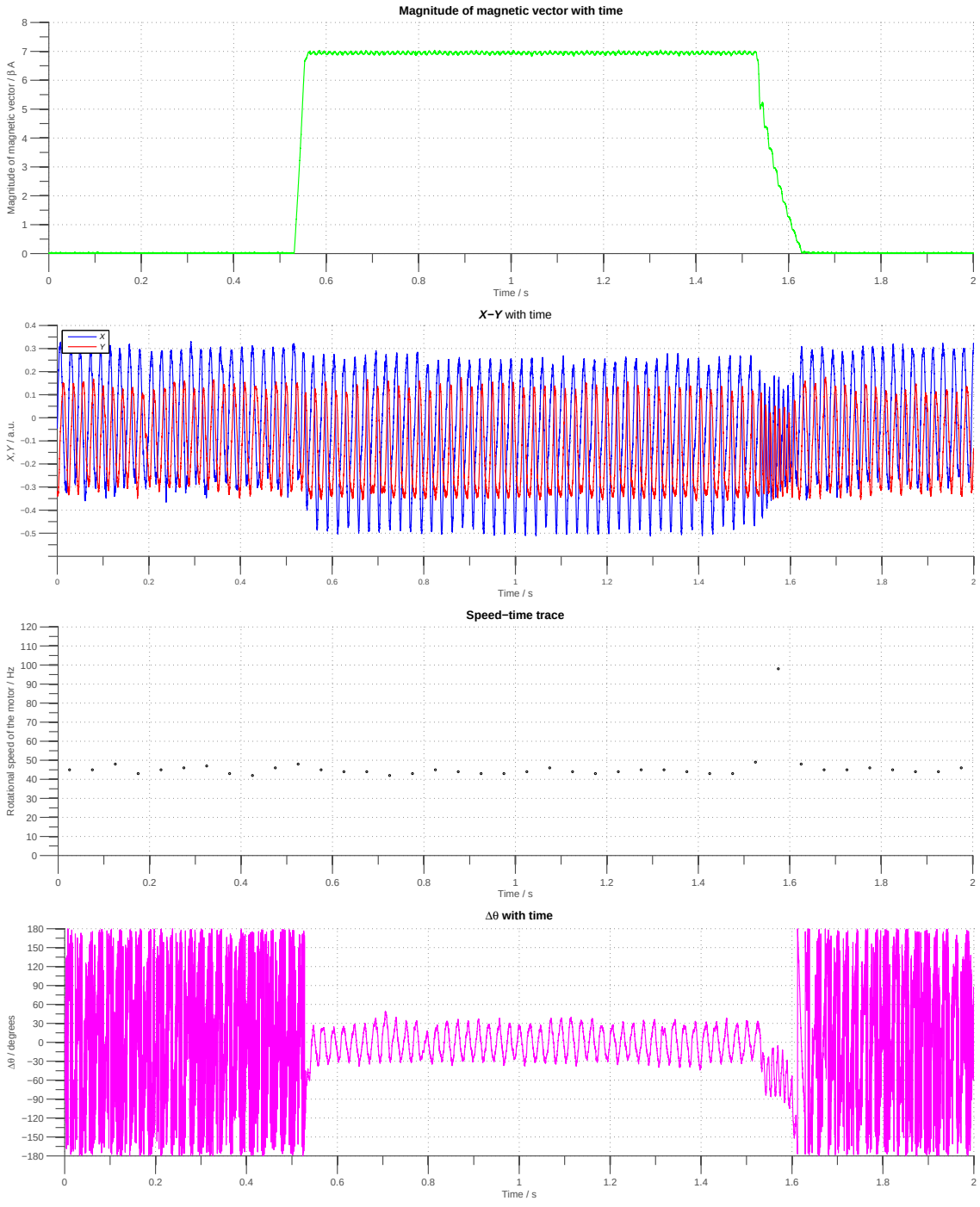

Figure 4.21. Resting-CCW experiment - Cell B. Plots of **(top)** magnitude of the magnetic vector with time, **(middle top)** X-Y with time, **(middle bottom)** speed-time trace, and **(bottom)** $\Delta\theta$ with time where the offset = 152.4°.

The details of experiment in which Cell B was driven in the clockwise direction is the same as that of the 20 Hz-CCW experiment except that the negative frequencies (to induce CW rotation) were used. Figure 4.22 shows the X-Y traces obtained for the 40 Hz-CW experiment where the motor was initially rotating in the CW direction at 38 Hz. The trajectories were different depending on the direction of rotation for the motor and the electromagnet. When the electromagnet was turned on, the motor was observed to lock up indicating that it was not able to generate sufficient torque to overcome the CW-rotating field.

When the electromagnet was switched off, Cell B rotated predominantly in the CW direction, which can be seen in the speed-time trace in Figure 4.23. The plot of $\Delta\theta$ with time shows two range of stable angles at which the bead followed the magnetic field. The offset = 5.2° which was artificially chosen so that the two range of angles can be displayed clearly in the figure. As a result of this, $\Delta\theta$ was not equal to zero during the period at which the bead is rotated at the resting speed of the motor between $t = 1.0$ s and $t = 2.0$ s. It is clear that the bead was observed to follow the magnetic field at two different angles, in agreement with the $\sin(2\Delta\theta)$ behaviour for superparamagnetic beads. However, these angles are not spaced exactly 180° apart. This is particular apparent between $t = 4.0$ s and $t = 6.0$ s. We attributed this to the mis-representation of the bead angle during the ellipse-fitting procedure as the bead was tracing out an elliptical path. The bead traced out an elliptical path because the axis of rotation of the motor was not perpendicular to the plane of the coverslip. As such, the bead is rotating in a circular path which is out-of-plane with the microscope.

Close-ups of $\Delta\theta$ with time at which the bead switches from one range of angles at which it was following the field to the other range are shown in Figures 4.24 and 4.25. These close-ups show that the magnetic field initially led the bead before the bead slipped. The bead consequently led the magnetic field once it was able to follow the field again.

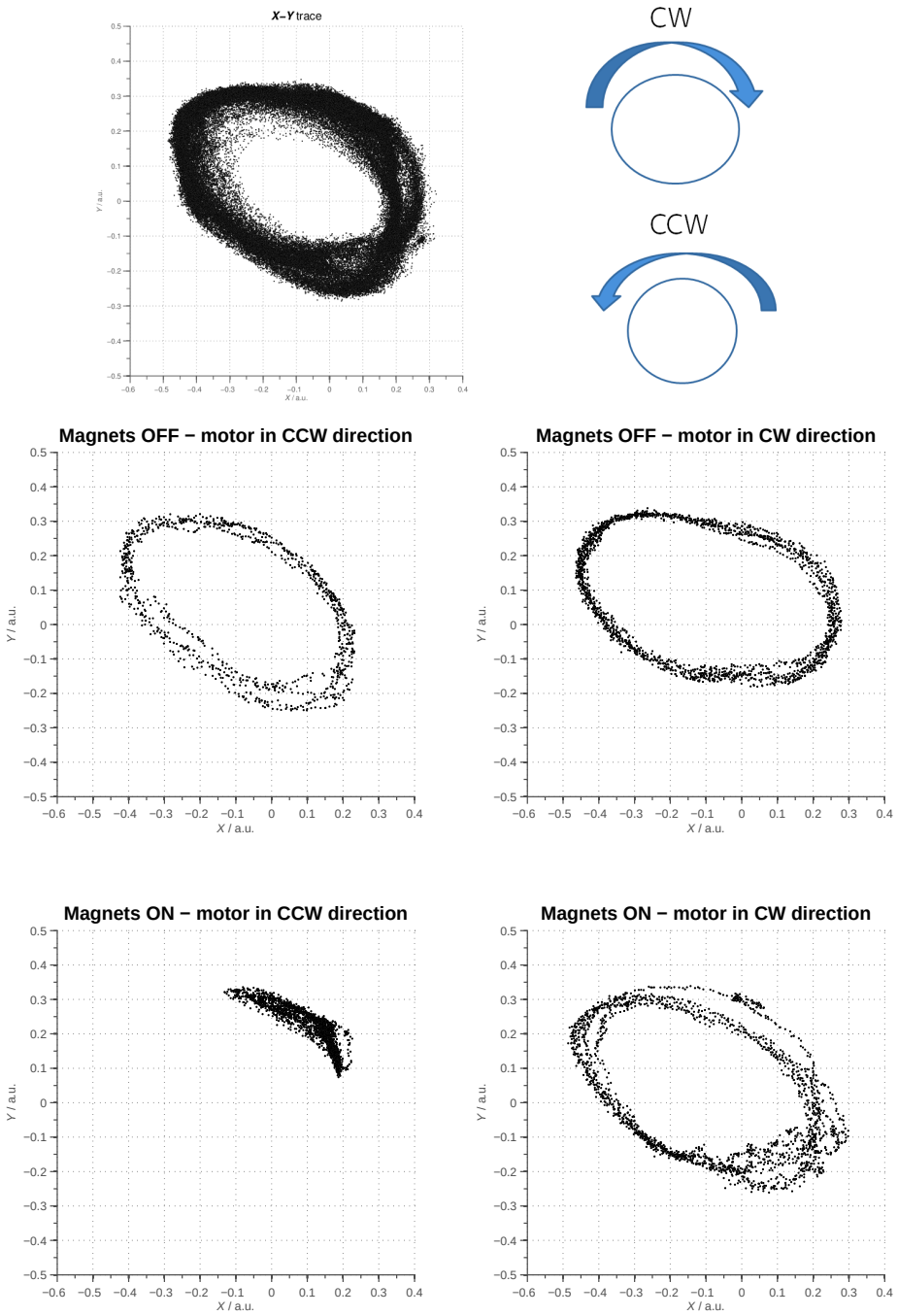

Figure 4.22. *X*-*Y* trace for the 40 Hz-CW experiment carried out on Cell B. The **(top left)** subfigure shows the full trace taken over 7.0 s and the **(top right)** schematic shows the direction of the orbital trajectory for rotation in the CCW and CW directions. The **(bottom)** subsidiary subfigures show the trace obtained when the motor was rotating in different directions under the presence and absence of a rotating magnetic field. The duration for the trace obtained for the subsidiary subfigures was 0.2 s except for the trace obtained when the motor was rotating in the CCW direction. The duration for this trace was 0.1 s. The resting speed of the motor was −38 Hz before the electromagnet was turned on.

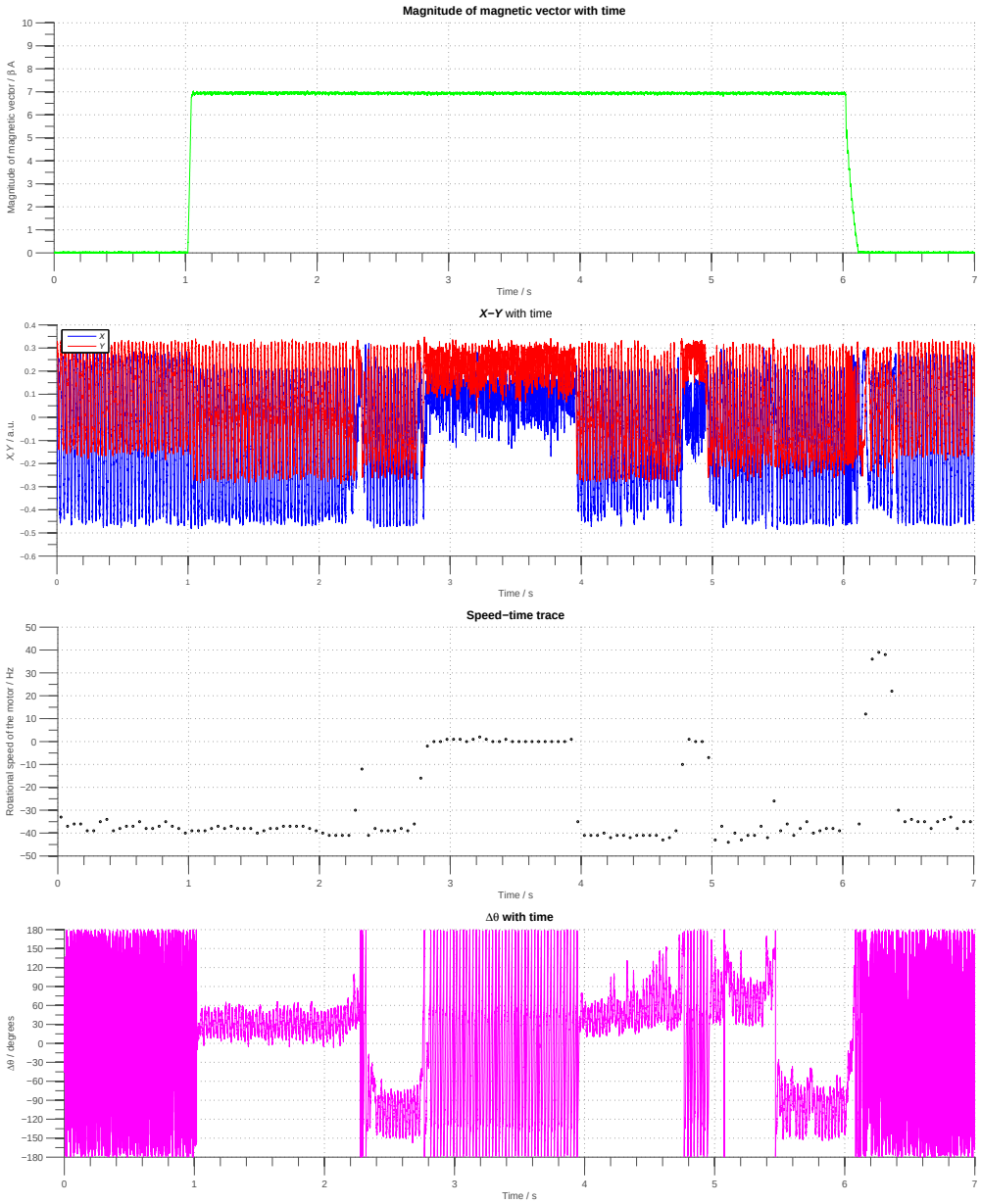

Figure 4.23. 40 Hz-CW experiment - Cell B. Plots of **(top)** magnitude of the magnetic vector with time, **(middle top)** X-Y with time, **(middle bottom)** speed-time trace, and **(bottom)** $\Delta\theta$ with time where the offset = 5.2°. The offset is chosen in such a way so that the two range of stable angles at which the bead followed the magnetic field can be displayed clearly. This also means that $\Delta\theta$ is not equal to zero during the period at which the bead is rotated at the resting speed of the motor between $t = 1.0$ s and $t = 2.0$ s. The bead is observed to follow the magnetic field at two different angles but these angles are not spaced 180° apart. This is particular apparent between $t = 4.0$ s and $t = 6.0$ s. This is attributed to the mis-representation of the bead angle during the ellipse-fitting procedure as the path traced out by the bead was elliptical. The bead traces out an elliptical path because the axis of rotation of the motor is not perpendicular to the plane of the coverslip.

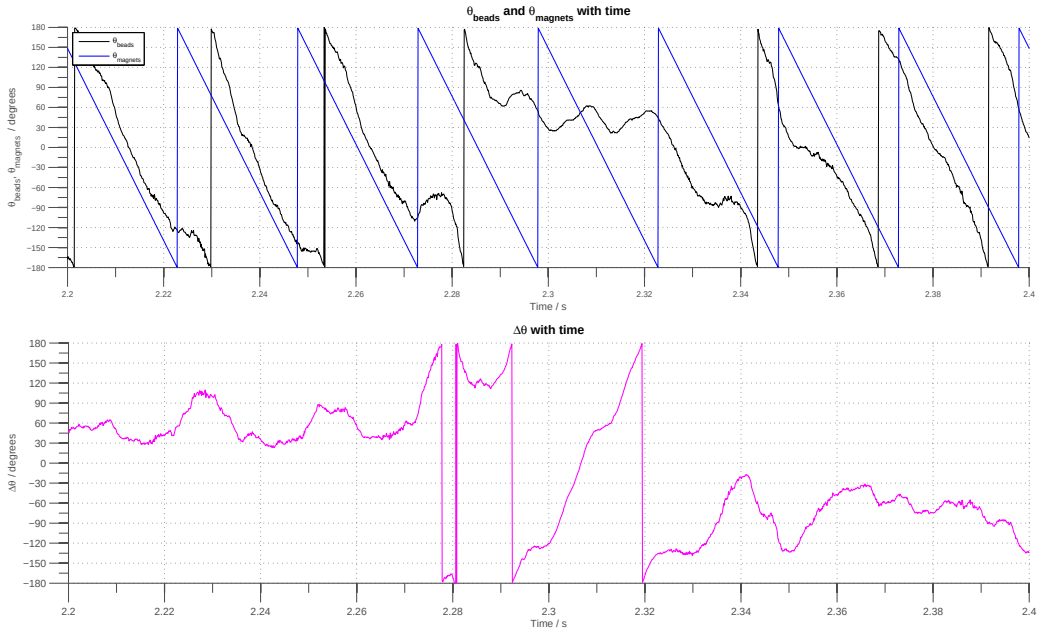

Figure 4.24. 40 Hz-CW experiment - Cell B. **(Top)** Plots of **(top)** θ_{bead} and θ_{magnet} with time, and **(bottom)** $\Delta\theta$ with time, both shown over the same interval of time. At some point during this window, the bead slips before following the rotating field at a different angle about 180° apart from the previous angle.

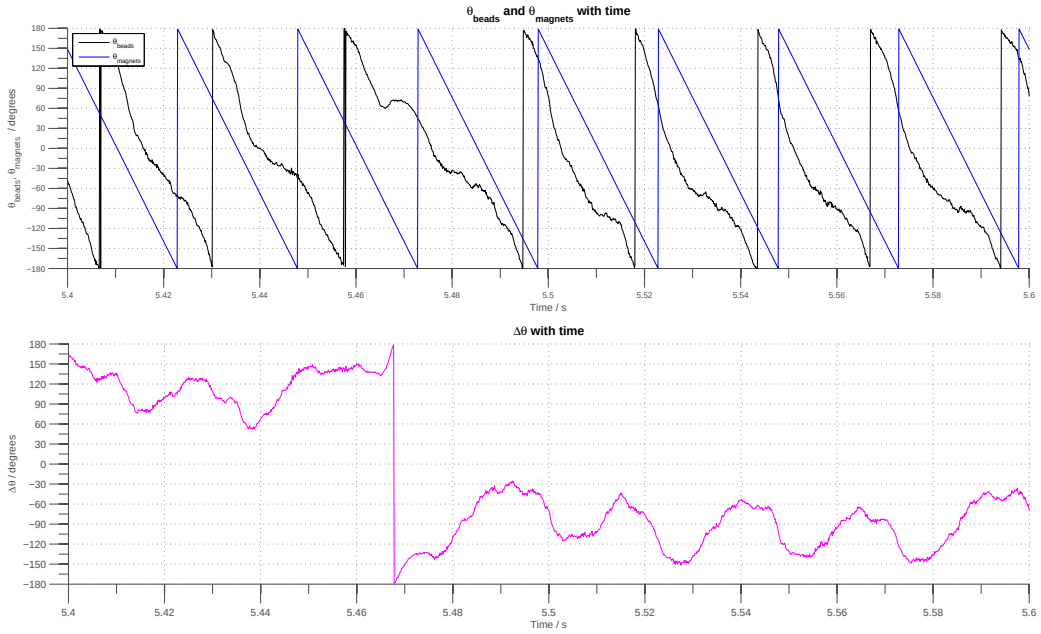

Figure 4.25. 40 Hz-CW experiment - Cell B. **(Top)** Plots of **(top)** θ_{bead} and θ_{magnet} with time, and **(bottom)** $\Delta\theta$ with time, both shown over the same interval of time. Again, the bead slips before following the rotating field at a different angle.

The results in this sub-section showed that it is possible to rotate the magnetic bead-hook assay in the CW direction when the motor is rotating in the opposite direction. It was not possible to drive the cells backwards when the cell rotated in the CCW direction. Sin ($2\Delta\theta$) behaviour associated with the superparamagnetic beads was also observed in the experiments above. However, the two angles at which the bead followed the rotating magnetic field was not exactly spaced 180° apart and this was due to the bead tracing out an elliptical path leading to the mis-representation of the angle after the ellipse fit.

4.2.3 Counter-clockwise ramp

In an attempt to explore the possibility of measuring torque-speed measurements from single motors in the shortest time possible, an input train containing as many frequencies (10 revolutions each) as one could write within 10 s was sent to the amplifier. This experiment is known as the counter-clockwise ramp experiment.

The electromagnet was initially switched off and then turned on at the frequency equal to the resting speed of the motor for 0.1 s. Following this, a ramp in which 10 revolutions at frequencies ranging from 5 Hz up to 200 Hz at 5 Hz intervals were sent to the amplifier before implementing a wind-down procedure to remove any remanence. The results of this experiment carried out on Cell A are shown in Figures 4.26 and 4.27.

The following analysis of the data collected here involved breaking up the data in segments in which the magnetic field rotated at different frequencies. The ellipse-fitting procedure was implemented separately for each block and used to obtained $\Delta\theta$ and its mean. The offset was determined using the block at which the electromagnet rotated at a frequency close to the resting speed of the motor.

The plot of magnitude of the magnetic vector with time showed that the output from the amplifier was fairly steady except at regions there is a frequency change. The

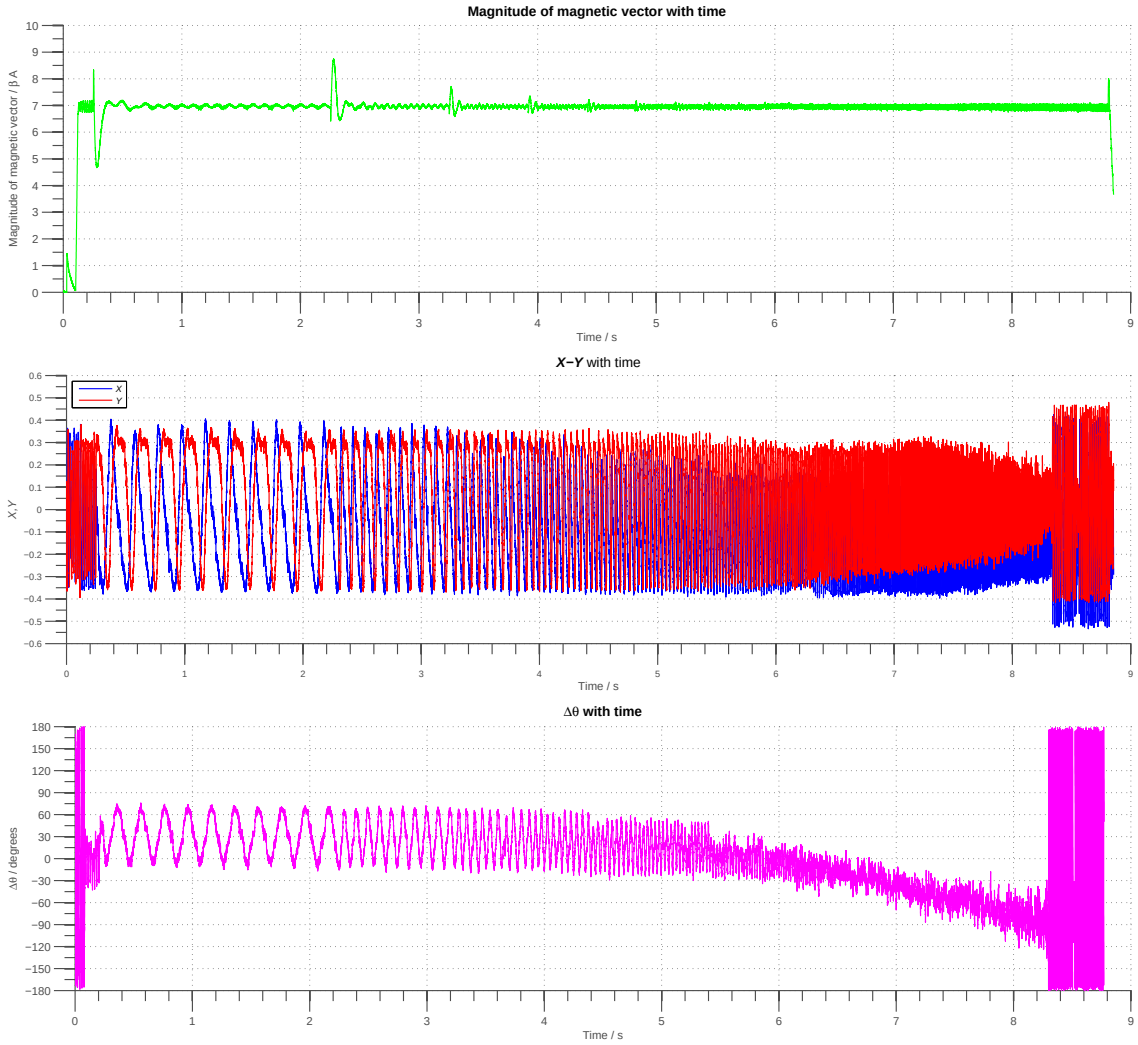

Figure 4.26. Counter-clockwise ramp experiment carried out on Cell A. Plots of **(top)** magnitude of the magnetic vector with time, **(middle)** X-Y with time, and **(bottom)** $\Delta\theta$ with time where the offset = 58.7°. The motor was initially rotating at 54 Hz.

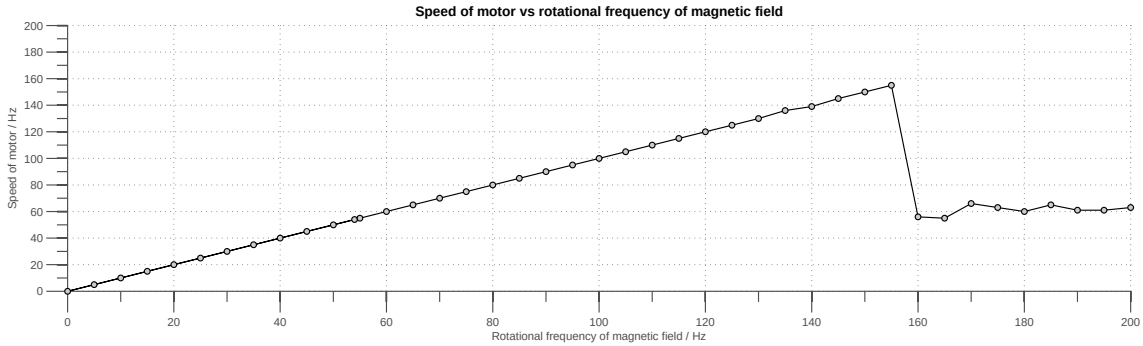

Figure 4.27. Speed of motor plotted against the rotational frequency of the magnetic field.

non-steady effects were more pronounced at low frequencies. The plot of X-Y with time shows that the orbital trajectories became smaller with increasing rotational frequency of the magnetic field before slipping at high frequencies. This can be observed more easily in the graph in which the speed of the motor is plotted against the rotational frequency of the magnetic field. The resting speed of the motor was 54 Hz and the bead was able to follow the magnetic field up to 155 Hz which is higher than the speed achieved previously for the same cell.

A plot of the mean $\Delta\theta$ with time shown in Figure 4.28 shows a downward trend after the ramp has started. The mean of $\Delta\theta$ calculated for each block plotted against the rotational frequency of the magnetic field demonstrates this trend more clearly. The mean of $\Delta\theta$ was close to 90° before the bead started to slip. This is a strong signature for the $\sin\Delta\theta$ behaviour behind the beads used which is at odds with previous observations that the magnetic behaviour of the beads followed a $\sin(2\Delta\theta)$ relationship.

In an attempt to determine the torque produced by the motor, $\Delta\theta$ calculated for three different models were calculated and compared to the data shown in Figure 4.28. The models are listed below:

- Constant motor torque and $\sin(2\Delta\theta)$ model for the bead (assuming a bead with superparamagnetic properties)

- Constant motor torque and $\sin\Delta\theta$ model for the bead (assuming a bead with ferromagnetic properties)
- Constant motor torque with a frequency-dependent drag term, $\sin\Delta\theta$ model for the bead.

The starting equation for this analysis is given by

$$\tau_{\text{drag}} = \tau_{\text{motor}} + \tau_{\text{magnetic}} \tag{4.1}$$

where the torque due to rotational drag is given by $\tau_{\text{drag}} = \gamma\omega$ where γ is the rotational drag coefficient and ω is the angular frequency while τ_{motor} and τ_{magnetic} represent the torque produced by the motor and the magnetic torque respectively. I assumed two models for the magnetic torque delivered to the bead, one of which is given by $\tau_{\text{magnetic},2\theta} = \kappa_1 \sin(2\Delta\theta)$ consistent with Equation (2.8) from Chapter 2 for superparamagnetic beads, and the other is given by $\tau_{\text{magnetic},\theta} = \kappa_2 \sin(\Delta\theta)$ for ferromagnetic beads.

In order to obtain an estimate for κ_1 and κ_2, a straight line, $y = -0.87x + 39.1$, was fitted to points less than 80 Hz where these data points were perceived to be linear. The y-intercept was then taken to be a measure of the mean $\Delta\theta$ at $\omega = 0$. Assuming that the stall-torque produced by the motor is 1260 pNnm measured by Reid *et al.* (2006), $\kappa_1 = 1287$ pNnm and $\kappa_2 = 1998$ pNnm. γ was determined at the resting speed of the motor in which the mean $\Delta\theta = 0$ and so $\tau_{\text{drag}} = \tau_{\text{motor}}$. The resting speed is determined from the stall-fit as it is reasonable to assume that the model-fits and the stall-fit intersect at the resting speed and are linear about this point. The resting speed used was 45 Hz and $\gamma = 4.46$ pNnm·s/rad assuming that the motor torque is the same at this speed as it is at stall.

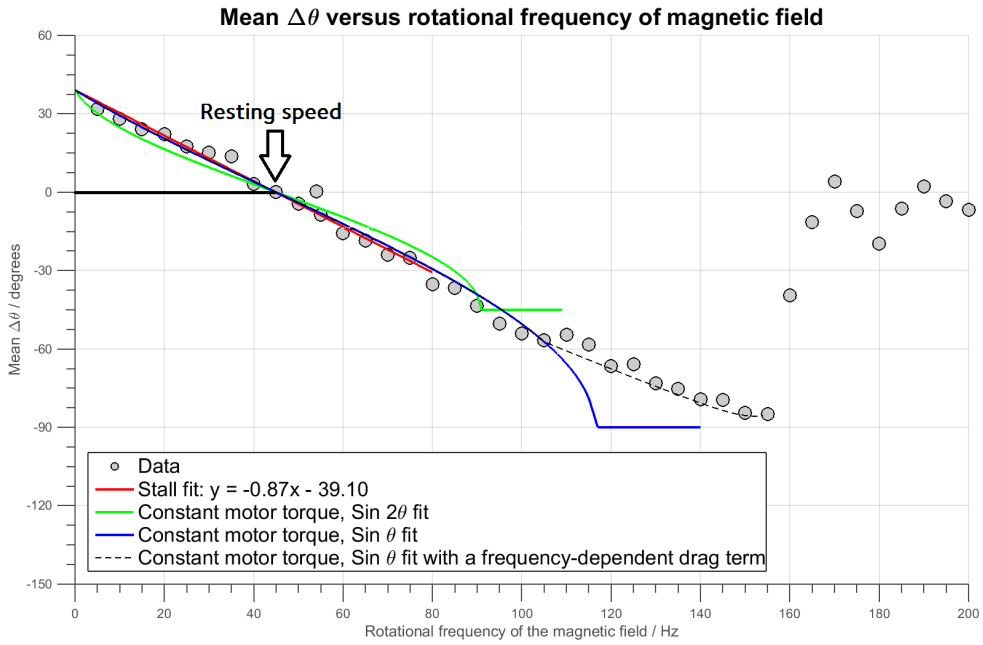

Figure 4.28. Plot of mean $\Delta\theta$ against rotational frequency of the magnetic field. A stall-fit was carried out using data up to 80 Hz to obtain an estimate for the mean $\Delta\theta$ at stall (39.1°). This value was used to determine κ_1 and κ_2 using the stall-torque of the motor which was estimated to be 1260 pNnm by Reid *et al.* (2006). $\Delta\theta$ at different rotational frequencies of the field determined in which a constant motor torque was assumed are plotted for the two different models for the behaviour of the magnetic bead (green and blue for the $\sin(2\Delta\theta)$ and $\sin\Delta\theta$ models respectively). An empirical fit assuming constant motor torque with a frequency-dependent drag term is also plotted. A frequency-dependent drag term was introduced in order to take into account the decrease in drag at high frequencies as a result of the bead tracing out smaller orbit sizes.

The fit for the $\sin(2\Delta\theta)$ model is given by

$$\Delta\theta = \frac{1}{2}\arcsin\left(\frac{\tau_{\text{drag}} - \tau_{\text{motor}}}{\kappa_1}\right) \tag{4.2}$$

while the fit for the $\sin\Delta\theta$ model is given by

$$\Delta\theta = \arcsin\left(\frac{\tau_{\text{drag}} - \tau_{\text{motor}}}{\kappa_2}\right). \tag{4.3}$$

Both these fits exhibit a certain characteristic in which they are linear about the resting speed and concave downwards as the argument of the arcsin function approaches 90°. From the fits above, the $\sin(\Delta\theta)$ model was observed to fit the data better than the $\sin(2\Delta\theta)$ model. This model cannot be made to fit the data at high frequencies due to the downwards concave at this regime. As such, I postulated a frequency-dependent drag term given by $\tau_{\text{drag}} = \gamma\omega \cdot \gamma'$ where γ' is the drag correction factor. This factor was assumed to be equal to 1 up to 105 Hz and decreases linearly to 0.724 at 160 Hz. This linearly decreasing drag factor is consistent with the observation that orbit sizes became smaller leading to a decrease in overall drag at higher frequencies.

This fit assuming constant motor torque, a frequency-dependent drag term and a $\sin\Delta\theta$ model for the magnetic behaviour of the beads used describe the data fairly well. The constant motor torque obtained is consistent with measurements previously measured for *E. coli* where a constant torque is observed at speeds up to 160 Hz in the CCW direction (Berg & Turner, 1993). Models that implement a power-stroke mechanism have been able to replicate torque-speed curves that were measured previously.

However, the $\sin\Delta\theta$ model used to describe the magnetic behaviour of the superparamagnetic bead used is inconsistent with previous observations. A bead that exhibits $\sin\Delta\theta$ behaviour would have to be perfectly ferromagnetic implying that the bead can only follow the magnetic field at one given angle. There were previous

observations made on the same bead in which the bead followed the magnetic field at two different angles suggesting that a $\sin(2\Delta\theta)$ model for the magnetic behaviour of the beads. These contradictory observations tell us that we do not have a good working model for the magnetic behaviour of the beads used in this experiment. This thus complicates the use of $\Delta\theta$ as a measure for the magnetic torque delivered to the motor.

Further work is required to calibrate the relationship between the angle of the bead and the angle of the magnetic field accurately. This can be repeated at different frequencies to take into account the frequency dependence on the drag. This can be achieved by rotating beads attached to cells de-energised using sodium azide or carbonyl cyanide *m*-chlorophenylhydrazone (CCCP) (Gabel & Berg, 2003). On the first instance, I could also look into a segmented angular analysis given that I did not calibrate the beads using de-energised cells. For this analysis, it is assumed that the torque relationship between the angle of the bead and the angle of the magnetic field is well-defined over a small segment of the orbital trajectory for the bead. This ensures that analysis is only carried out on segments of the angle in which the torque is well-defined and ignores the rest of the orbit in which varying torque was delivered to the motor.

4.3 Low-load experiments using the magnetic bead-filament assay

In this section, I will present results in which stators were observed to drop out at low loads. The experiment was also designed to determine how the slipping probability varies with the strength of the magnetic field.

Magnetic torque was delivered to magnetic bead-filament assays located at the centre of the field-of-view of the imaging system. Each assay consisted of a cell capable

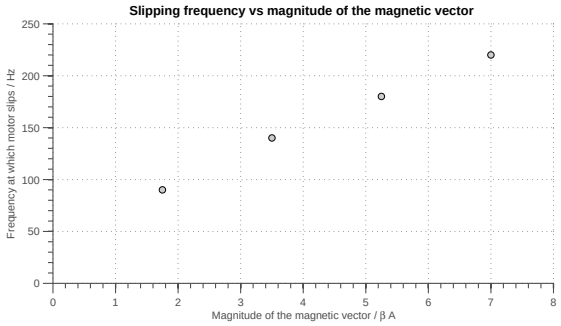

Figure 4.29. Scatter plot of slipping frequency against magnitude of the magnetic vector.

of expressing cysteine residues on the filament which can be easily biotinylated. 1 μm Dynabeads MyOne T1 superparamagnetic beads were attached to these biotinylated filaments. The cells used are capable of switching their direction of rotation. The assays were subjected to a magnetic field rotating in the CCW direction. The series of experiments shown here were carried out using the electromagnet Mk IIa and a long working distance condenser from Nikon having NA = 0.52.

In these experiments, a train of pulses, each a second long, were sent to the amplifier at increasing frequencies. In between each pulse, the electromagnet remained off for 2.0 s. The easy start-up and wind-down procedures were not implemented for these pulses.

Figure 4.29 shows a scatter plot of the frequency at which the motor slips against the magnitude of the magnetic vector. The plot shows a largely linear relationship between the two variables.

Figure 4.30 shows the results obtained when the magnitude of the magnetic vector was 1.75 βA. The motor was observed to follow the magnetic field up to 90 Hz before slipping. When the electromagnet was switched off, the speed of the motor remained constant except when it switched. The resting speed of the motor was about 30 Hz.

When the magnitude of the magnetic vector was increased to 3.5 βA, the motor was able to follow the magnetic field up to 140 Hz, a speed change of at least 110 Hz. This result can be seen in the speed-time trace shown in Figure 4.31. The resting

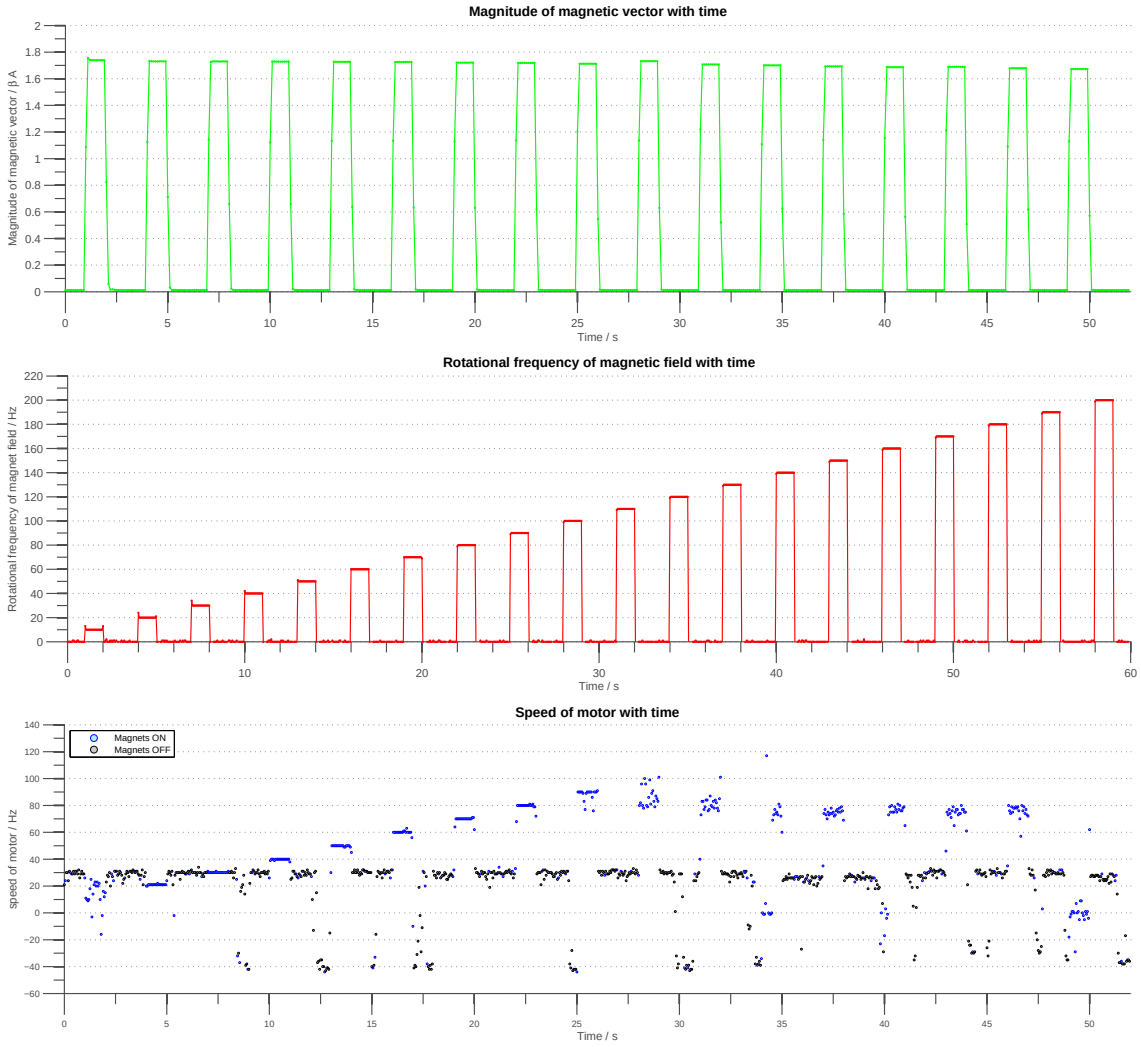

Figure 4.30. Clockwise rotation experiments carried out on a magnetic bead-filament assay. The magnitude of the magnetic vector was 1.75 βA. Plots of **(top)** magnitude of the magnetic vector with time, **(middle)** rotational frequency of the magnetic field, and **(bottom)** speed-time traces for the motor when the electromagnet was switched on and off.

speed of the motor when the electromagnet was switched off remained fairly constant. The plot of the magnitude of the magnetic vector with time exhibits some variation. This observation shows that the calibration method implemented for Mk IIa is not as good as that implemented for Mk IIb.

Figure 4.32 shows the results obtained when the magnitude of the magnetic vector was further increased to 5.25 βA. The motor followed the field up to a speed of about 180 Hz. When the electromagnet was switched off after being turned on at high frequencies, the resting speed of the motor was observed to decrease with time. This is a signature of stators dropping out at low load, a result of which was observed previously using a rotary optical clamp by Pilizota *et al.* (2007).

The cell was allowed to recover its resting speed and the experiment was repeated at using at a higher magnitude about 7.0 βA where the results are shown in Figure 4.33. The motor was capable of following the magnetic vector up to about 220 Hz. Again, the resting speed of the motor was observed to decrease with time especially after having been driven at speeds greater than 140 Hz.

In an attempt to investigate the general speed changes as the motor was made to rotate at higher speeds, histograms of the speeds of the previous four figures are presented in Figure 4.34. Spikes present in the histograms of speeds when the magnets are switched on indicate the speeds at which the motor can follow the magnetic field. The maximum speed at which the motor can follow the magnetic field is clear from the histogram for the largest magnitude of the magnetic vector which is about 220 Hz. Even though the maximum speed change attained is not close to the zero-torque speed, this experiment informs us that it is very well possible to rotate the motor close to this speed simply by doubling the maximum current delivered to each coil.

The most dominant speeds in these histograms represent the resting speed of the motor. Sub-peaks are not present for histograms in which the magnitude of the magnetic vector was less than 5.25 βA. The sub-peaks present in histograms where

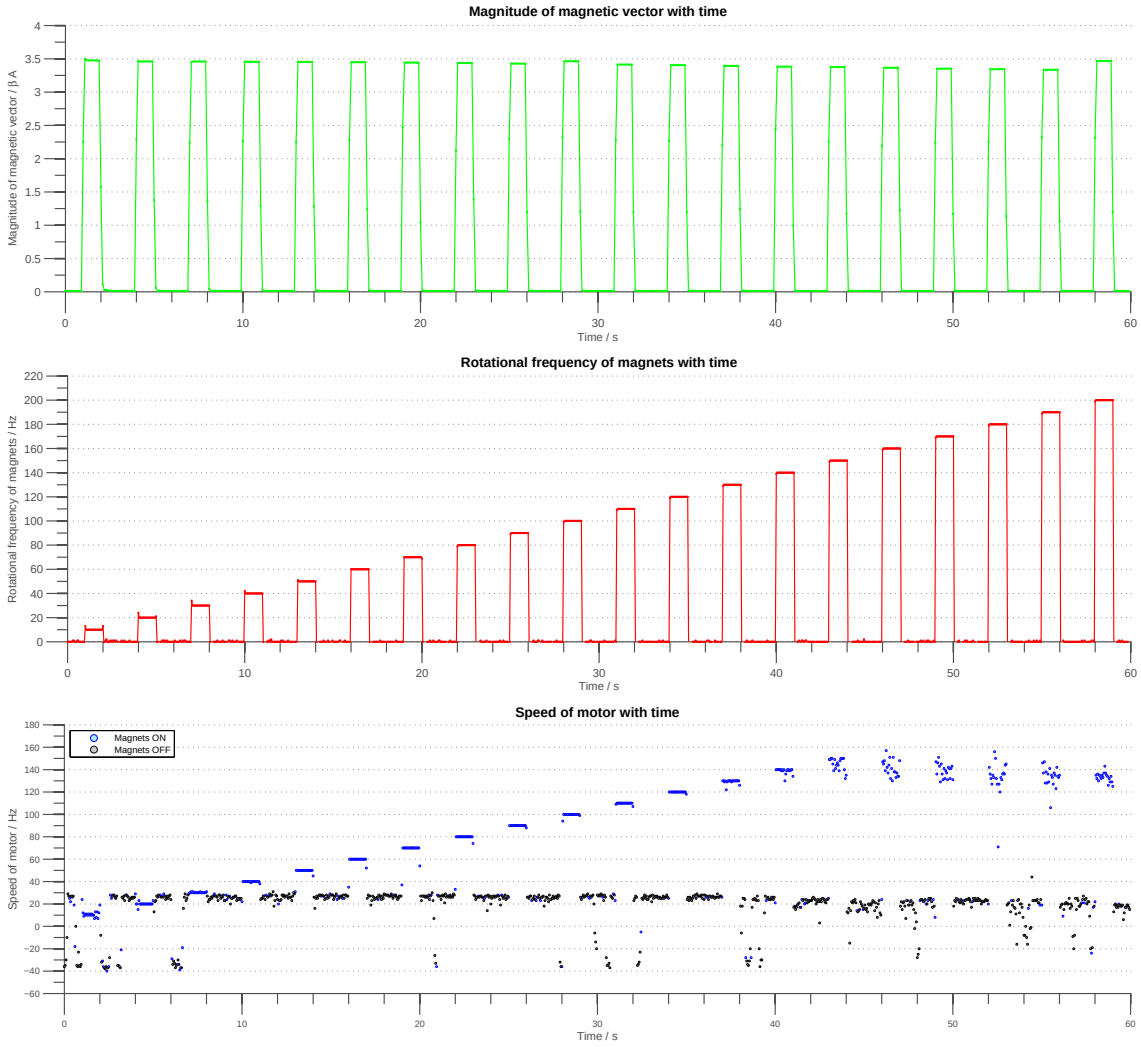

Figure 4.31. Clockwise rotation experiments carried out on a magnetic bead-filament assay. The magnitude of the magnetic vector was 3.5 βA. Plots of **(top)** magnitude of the magnetic vector with time, **(middle)** rotational frequency of the magnetic field, and **(bottom)** speed-time traces for the motor when the electromagnet was switched on and off.

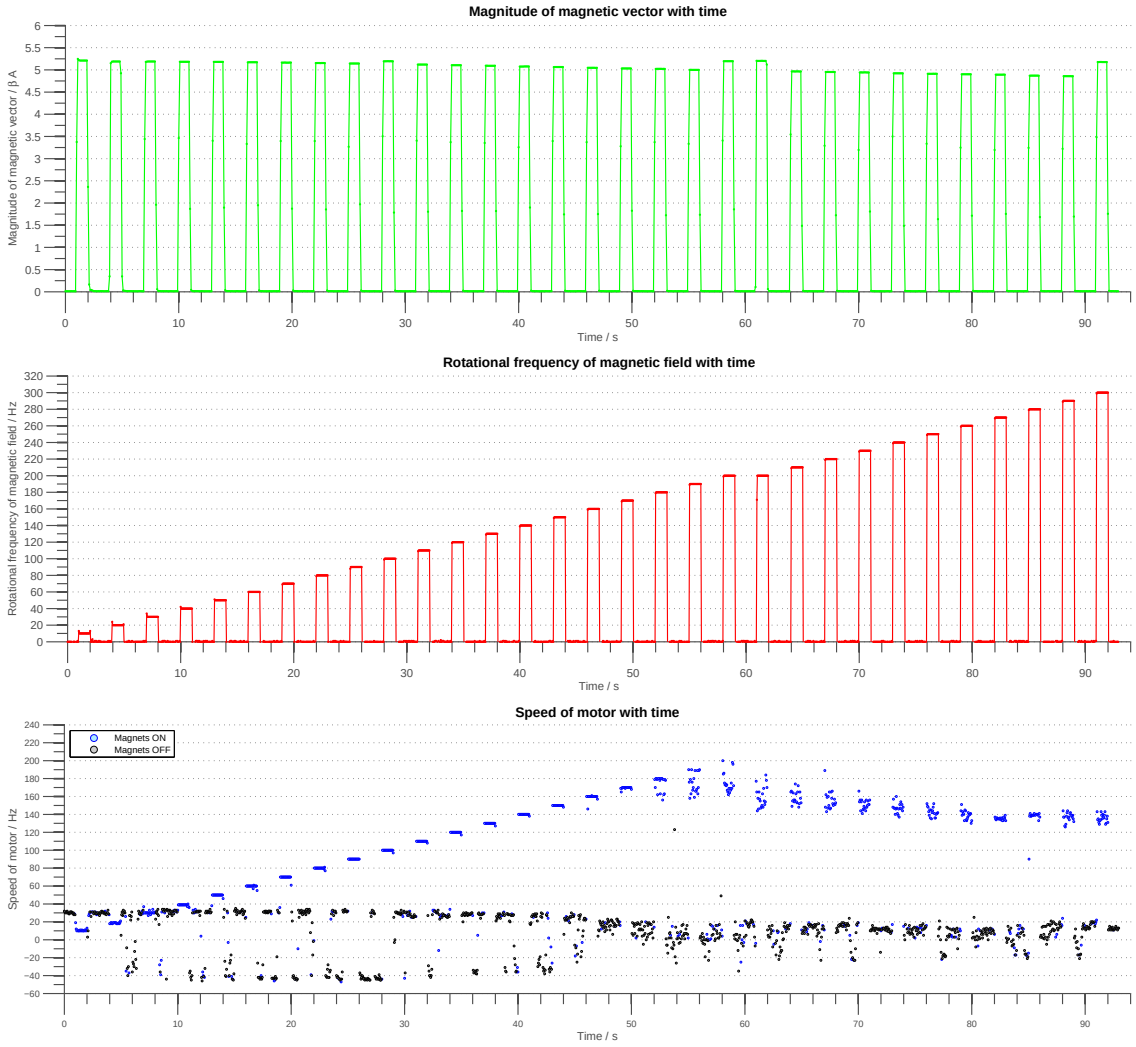

Figure 4.32. Clockwise rotation experiments carried out on a magnetic bead-filament assay. The magnitude of the magnetic vector was 5.25 βA. Plots of **(top)** magnitude of the magnetic vector with time, **(middle)** rotational frequency of the magnetic field, and **(bottom)** speed-time traces for the motor when the electromagnet was switched on and off.

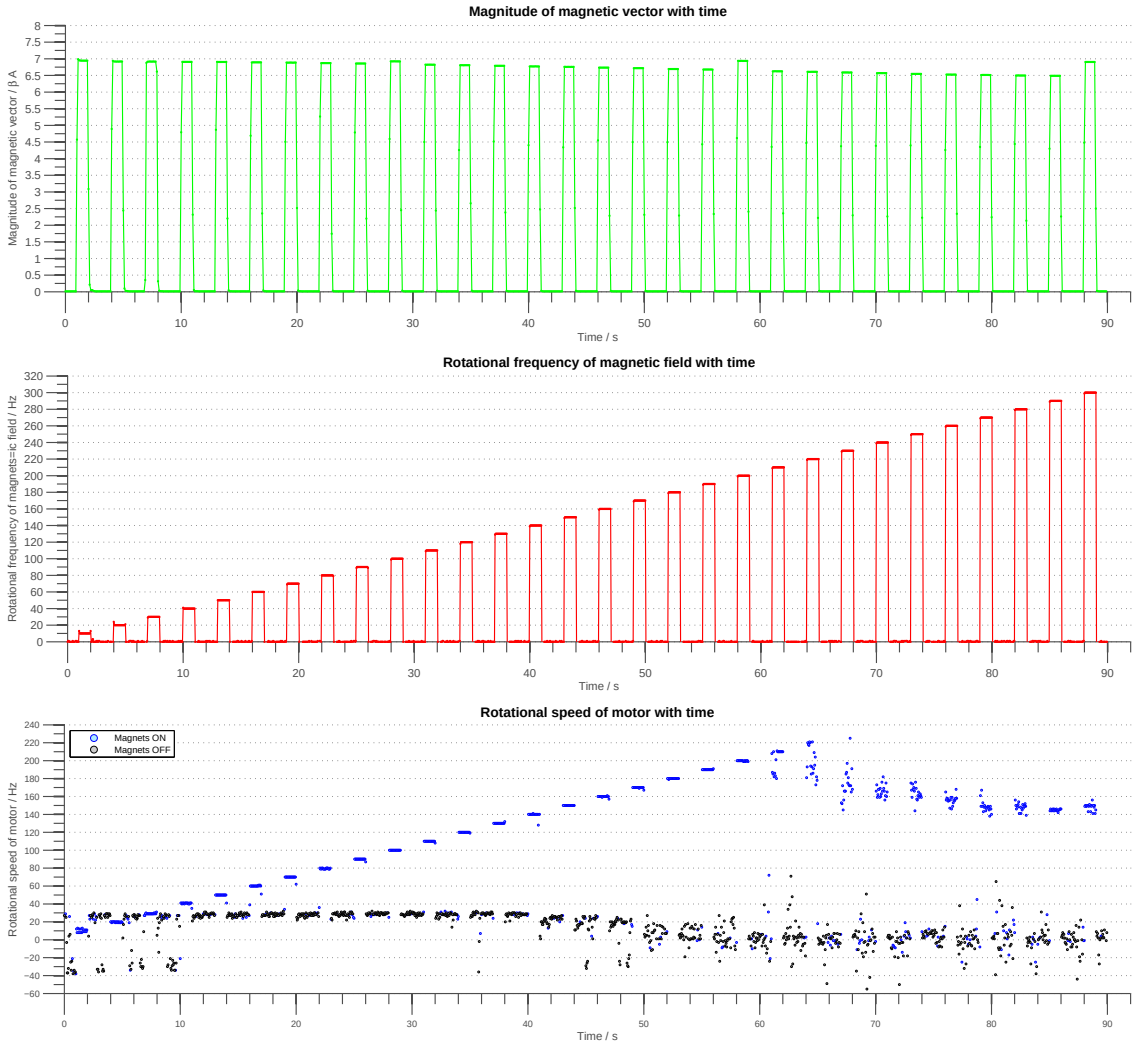

Figure 4.33. Clockwise rotation experiments carried out on a magnetic bead-filament assay. The magnitude of the magnetic vector was 7.0 βA. Plots of **(top)** magnitude of the magnetic vector with time, **(middle)** rotational frequency of the magnetic field, and **(bottom)** speed-time traces for the motor when the electromagnet was switched on and off.

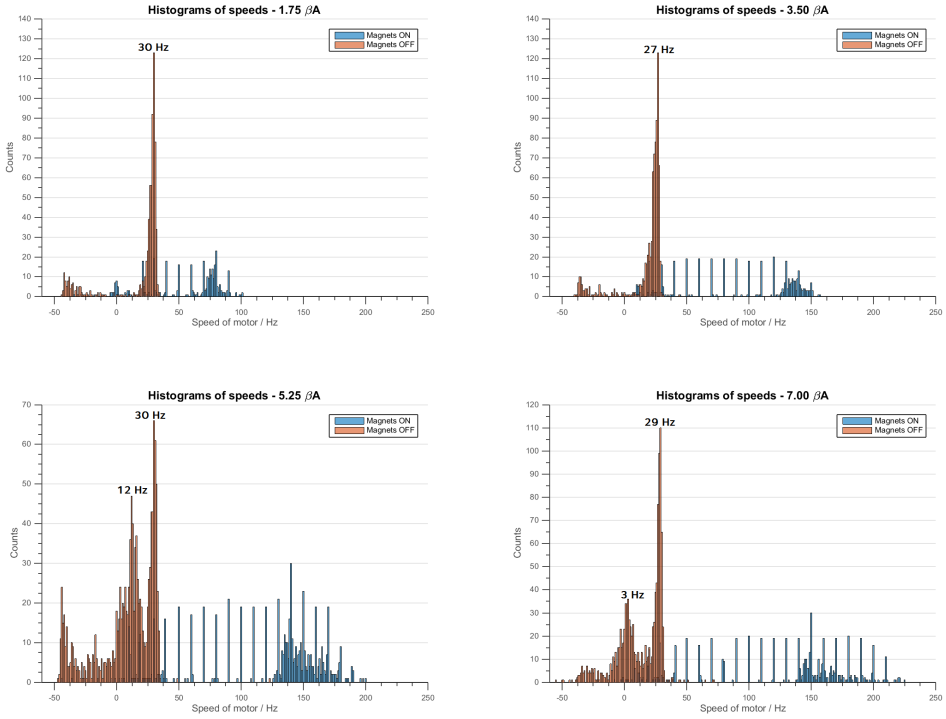

Figure 4.34. Histograms of speeds of the speed-time traces shown in the previous four figures for different magnitude of the magnetic vector. Spikes present in the histograms of speeds when the magnets are switched on indicate the speeds at which the motor can follow the magnetic field. Speed at which peaks or sub-peaks for speeds when the magnets are switched off are quoted in the figure. The largest peaks are associated with the resting speed of the motor and the speeds of the sub-peaks are associated with the dominant speed of the motor after the motor was spun at speeds greater than 150 Hz. The maximum speed at which the motor can follow the magnetic field is about 220 Hz.

the magnitudes of magnetic vector are equal to 5.25 βA and 7.00 βA are representative of the dominant speed of the motors after the motor was spun at speeds greater than 150 Hz. This is indicative of stators dropping out when the motor was been forced to rotate at high speeds which is equivalent to a motor rotating at low loads.

The slowest sub-peak observed is about 3 Hz which is likely to be the speed of a single stator. If this true, approximately 10 stators are present in the motor at the resting speed. It is also known that up to 11 stators can be present in the motor (Reid *et al.*, 2006). However, the resting speed recorded for a motor with an almost

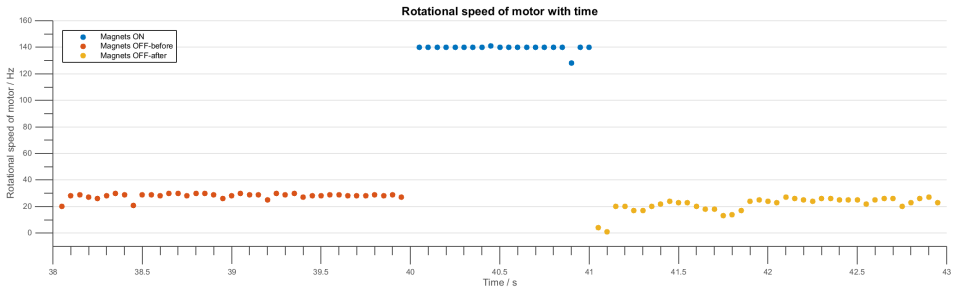

Figure 4.35. Speed-time trace of the motor before and after the motor was spun at 140 Hz. A single stator was deduced to have dropped out as the resting speed of the motor was slower than its initial resting speed.

complete set of stators is not consistent with the findings of Reid *et al.* (2006) in which the speed of a 1 μm bead attached to a motor having a full set of stators was quoted to be 61.6 ± 5.7 Hz. This can be attributed to the lower PMF across the membrane of the motor in this experiment compared to those studied in the work of Reid *et al.* (2006). There is no direct measure for the PMF in this experiment to verify this.

In order to establish the speed drop due to a single stator more accurately, I investigated the speed-time trace before and after the motor was made to rotate at 140 Hz in the forwards direction in which the magnitude of the magnetic vector was 7.0 βA. The speed-time trace is shown in Figure 4.35. This particular section of the speed-time trace was picked because this was the initial speed at which the motor was made to rotate and a single stator was observed to drop out afterwards. Histograms of speeds for this particular speed-time trace is shown in Figure 4.36. The peak of the histogram before the magnets was 29 Hz and the peak of the histogram after the magnets were turned on was 25.5 Hz which is the of the two bins containing the same number of counts. The difference in speed between the peaks is about 3.5 Hz which is within experimental error of the speed of a single stator quoted above.

In conclusion, signatures of stators dropping out at higher frequencies, or low load, were observed, consistent with previous observations made using fast-rotating optical tweezers by Pilizota *et al.* (2007). A single stator was observed to drop out after the

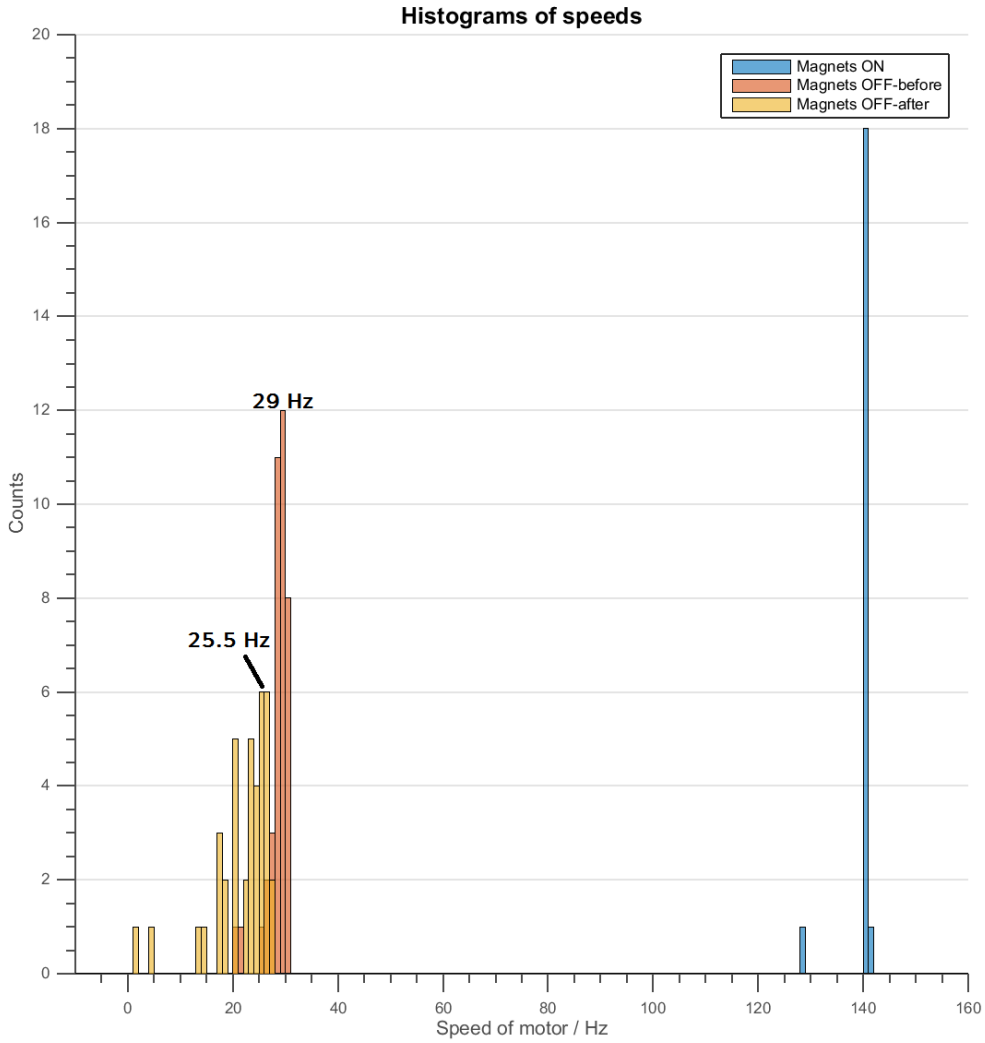

Figure 4.36. Histograms of speeds when the magnets were switched on and off at 140 Hz. When the magnets were turned on, the motor was able to follow the magnet at 140 Hz. The peak of the histogram before the magnets was 29 Hz and the peak of the histogram after the magnets were turned on was 25.5 Hz from the average of the two bins containing the same number of counts. The difference in speed between the peaks is about 3.5 Hz which is within experimental error of the speed of a single stator.

motor has been spun forwards at a speed of 140 Hz and the speed contribution of a single stator is about 3 Hz. Peaks and sub-peaks observed in histograms of speed-time traces in which the motor was made to rotate at high speeds reveal that subsequent dominant resting speeds are always less than the initial resting speed. The results obtained here are consistent with the findings of Tipping *et al.* (2013a) in which stator number decreases with decreasing load. Further systematic studies of the dynamics behind these stators using this method will allow us to determine the on/off rates of stators at different frequencies. Such studies will allow us to address more direct questions about the load-sensing ability of stators.

Chapter 5

Discussion, Conclusions and Future Outlook

The bacterial flagellar motor is a remarkable ion-driven molecular machine, about 50 nm in diameter. It is the main source of propulsion for bacterial cells, allowing these cells to swim towards regions with more favourable conditions (Berg & Brown, 1972; Adler, 1973). Recently, we have begun to recognise the mechanosensing ability of the motor which is essential for the onset of the formation of biofilm - extracellular matrix-forming polymers necessary for bacterial cells to live as members of organised surface-attached microbial communities. Even though we know a great deal about its structure, genetics, assembly and function; we have yet to understand the mechanism of torque-generation at a deeper level, in particular the role of stators and their interactions with the rotor.

There are many published models that describe this mechanism whose main outputs are torque-speed relationships and stepping dynamics. These models fall into three different categories: ion-turbines, ion-turnstiles and conformational-change models. The motion of the rotor relative to stators in ion-turnstile models is driven by thermal forces and a ratchet mechanism is required in order to ensure that the mo-

tor rotates in one preferable direction. Both ion-turbines and conformational-change models follow a power-stroke mechanism in which motion is tightly coupled to ion-transit. The thermal-ratchet mechanism for the motor has been ruled out due to the absence of potential barrier when the motor is made to rotate in the backwards direction demonstrated using optical tweezers (Berry & Berg, 1997). Ion-turbines have also been ruled out due to the lack of structural data to suggest the existence of tilted lines of charges required for these models to work. Conformational-change models are currently the strongest candidate for the torque-generating mechanism. The existence of highly-conserved ion-binding sites in the MotA of stators provide indirect physical evidence for this model and the majority of the models developed in the past decade are derivatives of this category of models.

There is thus a need for a mechanical method capable of driving the motor forwards and backwards at different speeds, as well as reporting the torque produced by the motor. This method will allow us to measure torque-speed relationships which we can use to compare with predictions of the torque-speed curves obtained from conformational-change models that describe the torque-generating mechanism of the motor.

Various methods of delivering torque were considered such as electrorotation, angular optical trapping and magnetic tweezers but they each had their shortcomings. For instance, electrorotation experiments suffered from heating issues and low assay yields while angular optical trapping lacked the availability of a suitable assay. In addition, the handles required were either to difficult to get hold of commercially (quartz cylinders) or hard to trap (rutile). Magnetic tweezers offer a promising way forward, but issues such as the availability of a suitable assay and a device capable of generating fast-rotating magnetic fields at sufficiently high strengths were yet to be resolved at the start of this project. From the theory of superparamagnetic beads,

the magnetic torque delivered to these beads are given by (Mosconi *et al.*, 2011)

$$\tau_{\text{magnetic}} = \frac{\alpha M_{\text{sat}} B}{2} \sin(2\Delta\theta) \tag{5.1}$$

where α is the anisotropy of the beads, M_{sat} is the saturating magnetisation of the superparamagnetic bead, B is the magnetic field strength and $\Delta\theta$ is the angle between the bead's easy axis and the magnetic field angle. Superparamagnetic beads thus obey a $\sin(2\Delta\theta)$ behaviour when following a rotating magnetic field. Such beads can follow the rotating field at two different angles and the maximum torque is attained when $\Delta\theta = 45°$. Back-of-the-envelope calculations revealed that a field on the order of tens of mT is sufficient to rotate a micron-sized particle at speeds up to 300 Hz.

To this end, I have set out to design several variants of the magnetic bead assay and construct an electromagnetic device capable of generating the required magnetic fields. Such a system allowed me to deliver magnetic torque to the bacterial flagellar motor. The two variants of the magnetic bead assay developed include the magnetic bead-hook assay and the magnetic bead-filament assay. In the magnetic bead-hook assay, a streptavidin-coated superparamagnetic bead is attached to an endogenously biotinylated hooks. In the magnetic bead-filament assay, streptavidin-coated superparamagnetic beads are attached to biotinylated filaments. The assays are highly reproducible and yields are very high. As such, it was very straightforward to obtain a good density of spinners with almost circular orbits. Spinners with almost circular orbits were selected because it is important that the plane of their orbits coincide with the plane of the rotating magnetic field and the imaging plane of the microscope.

A three-pole electromagnet was designed and fabricated which allowed fast-rotating magnetic fields to be generated. The magnetic field is made to rotate using 120° out-of-phase sinusoidal current inputs into each coil of the electromagnet. The experimental results obtained in the previous chapter have demonstrated the potential of

delivering external torque using magnetic means. I was able to stall and rotate the motor forward at speeds up to 220 Hz and in the reverse direction. Even though these experiments highlighted certain shortcomings with the delivery of external torque using magnetics means, it still allowed me to establish several key results for the motor.

Stalling experiments carried out contributed massively to the study of the load sensitivity of stators (Tipping *et al.*, 2013a). The main result obtained from stalling experiments revealed that stator mechanosensing is not a direct function of rotation but of torque. Further data supplemented by experimental results obtained from Dr Murray Tipping conclusively show that stator number increases with load. From these results obtained, we noted that the observed decrease of stator number with reduced IMF and load, pointed towards the common feature of reduced torque generated by each stator. The reduction in torque can be attributed to a simple conformational change that altered the length of the linker between the cytoplasmic domains of each stator and its point of anchorage to the peptidoglycan layer. This conformational change could provide the necessary mechanosensitivity as the free-energy difference between long and short forms would contain a term equal to the length change times the force on a stator. There is indirect evidence that such a mechanism is at play, in the form of conformational changes observed in the periplasmic domain of MotB coupled to other conformational changes observed in MotB during stator binding (Hosking *et al.*, 2006; Kojima *et al.*, 2009; Morimoto & Minamino, 2014).

We also proposed more complicated mechanisms involving conformational changes in other motor components sensitive to the change in stator-rotor interface caused by external load. FliL is required for correct motor function in several bacterial species, with some Δ*fliL* mutants being able to swim but unable to swarm (Raha *et al.*, 1994) and some losing motility entirely (Jenal *et al.*, 1994). FliL is an integral motor protein and has shown to be a part of the *P. mirabilis* surface-sensing mechanism (Lee & Belas, 2014). However, the exact nature of the interactions between it and the rest of

the flagellar motor is unclear. Furthermore, these interactions may differ substantially between different species. A mechanosensory role for the stators, perhaps aided or enhanced by FliL, would explain the load-dependence of stators observed.

Forwards rotation of the motors at different speeds using the magnetic tweezers showed that the orbital trajectory of the beads changed with frequency. This has implications on the rotational drag of the motor where smaller orbits will experience less rotational drag. Characterisations of the orbit size and surface drag at different frequencies are essential to obtain an accurate measure for the rotational drag due of viscous drag. It is important that these details are taken into account in order to obtain accurate estimates for the torque produced by the motor.

Results obtained from low-load experiments showed that I was able to rotate the motor using the magnetic tweezers in the forward direction up to approximately 220 Hz. Even though I was not able to rotate the beads at speeds close to the zero-torque speeds of wild-type bacterial strains (approximately 350 Hz), the ability to rotate the motor up to 220 Hz was sufficient to observe signatures of stators dropping out at low load. These signatures are consistent with previous observations made using fast-rotating optical tweezers by Pilizota *et al.* (2007). A single stator was observed to drop out after the motor has been spun forwards at a speed of 140 Hz and the speed contribution of a single stator was about 3 Hz. Peaks and sub-peaks observed in histograms of speed-time traces in which the motor was made to rotate at high speeds reveal that subsequent dominant resting speeds are always less than the initial resting speed. The results obtained here are consistent with the findings of Tipping *et al.* (2013a) in which the number of stators decreases with decreasing load.

An attempt to measure the torque-speed curve of a single motor was carried out using a counter-clockwise torque ramp consisting of 10 revolutions at rotational frequencies ranging from 5 Hz up to 200 Hz at 5 Hz intervals. In this experiment, the motor was able to follow the field up to 155 Hz before the bead began to slip

due to the inability of the combined magnetic and motor torque to overcome the rotational viscous drag of the bead. In an attempt to determine the torque produced by the motor, the measurements of the mean $\Delta\theta$ obtained at different frequencies were compared with those calculated from various models assuming constant motor torques but different models for the magnetic beads. The starting point for this analysis makes use of the equation

$$\tau_{\text{drag}} = \tau_{\text{motor}} + \tau_{\text{magnetic}} \tag{5.2}$$

where the torque due to rotational drag is given by $\tau_{\text{drag}} = \gamma\omega$ where γ is the rotational drag coefficient for the rotating assay and ω is the angular frequency while τ_{motor} and τ_{magnetic} represent the torque produced by the motor and the magnetic torque respectively. γ was empirically determined using the resting speed of the motor and the constants in τ_{magnetic} were determined using the stall torque quoted in literature (1260 pNnm measured by Reid *et al.* (2006)).

The best fit that describe the data obtained assumes a constant motor torque with a frequency-dependent drag term and a $\sin\Delta\theta$ model for the magnetic behaviour of the beads used describe the data fairly well. The constant motor torque obtained is consistent with measurements previously measured for *E. coli* where a constant torque is observed at speeds up to 160 Hz in the CCW direction (Berg & Turner, 1993). This torque-speed relationship agree with outputs obtained from models that implement the power-stroke mechanism.

However, the $\sin\Delta\theta$ model used to describe the magnetic behaviour of the superparamagnetic bead used is inconsistent with previous observations made on the same bead. A bead that exhibits $\sin\Delta\theta$ behaviour would have to be perfectly ferromagnetic and follows the magnetic field at one given angle. Previous observations made on the same bead showed that the bead was capable of following the magnetic

field at two different angles, suggesting a $\sin(2\Delta\theta)$ model for the magnetic behaviour of the bead. These contradictory observations tell us that we do not have a good working model for the magnetic behaviour of the beads used in this experiment. This thus complicates the use of $\Delta\theta$ as a measure for the magnetic torque delivered to the motor.

Despite the shortcomings above, the ability to deliver magnetic torque to the bacterial flagellar motor will pave way for many interesting experiments to come. This is especially true as there many avenues in which the existing method can be improved.

It is strongly encouraged that the relationship between the angle of the bead and the angle of the magnetic field is calibrated by de-energising motors after each experiment. This calibration technique can be repeated at different frequencies which will generate a look-up table which takes into account variations in the local hydrodynamics (as a result of changing orbital trajectories at different frequencies), our lack of understanding of the behaviour of the beads used in a rotating magnetic field and any possible angular inhomogeneities in the magnetic field. Even though this calibration method has not been implemented, it is still possible to extract information about the torque delivered from the existing datasets. A segmented angular analysis can be carried out the in which it is assumed that torque relationship between the angle of the bead and the angle of the magnetic field is well-defined over a small segment of the bead's orbit. This ensures that the analysis is only carried out on segments of the angle in which the torque is well-defined and ignores the rest of the orbit in which varying torque was delivered to the motor.

Another possible avenue for improvement is to increase the linear regime of the existing set-up by constricting the waist of the trapping beam (Pilizota *et al.*, 2007). This implementation will increase our confidence in the angular data for larger orbits. Other methods to resolve the angle of the bead orientation were not explored but

they can be investigated in future experiments. Finally, combining fluorescence and rotation experiments in order to conduct ion-flux experiments using bacterial cells that report sodium concentration using fluorescence.

An amplifier with steady and predictable outputs requiring minimal calibration is strongly recommended. Given that I was not very far from being able to rotate the motor at speeds close to the motor's zero-torque speed, an amplifier capable of delivering more current will certainly help achieve this goal. In addition, it is worth exploring the option of amplifiers with both DC and AC capabilities. Such amplifiers will allow stall measurements to be carried out without the need of permanent magnets.

The experiments here can be extended to other *E. coli* strains such as non-switching ones. To this end, I have isolated plasmids containing the single-site cysteine mutation in the filament gene, work of which I did not present in this thesis. Such plasmids can be used to transform other strains so that they express cysteine residues on the filament. This transformation can be carried out using a method of allelic exchange as described in Brown *et al.* (2012).

I am also very much interested in extending this work to other bacterial species. Attempts to construct a suitable magnetic bead assay for *Caulobacter crescentus* were carried out in collaboration with Radhika Agarwal from the University of Indiana in work that was not published here. We were not successful as we were not able to establish a method of attaching the bead to the motor in the time period in which the cells were still motile.

There are indeed plenty of things that can be done and we can only look forward to carrying them out in the near future. In the long term, we would be interested in faster experiments with higher angular resolutions. The magnetic handles suitable for such experiments are not currently available but the journey to discover and carry these experiments out will be an exciting one.

Bibliography

Adachi, K., Oiwa, K., Nishizaka, T., Furuike, S., Noji, H., Itoh, H., Yoshida, M. & Kinosita, Jr., K. (2007). Coupling of rotation and catalysis in F(1)-ATPase revealed by single-molecule imaging and manipulation. *Cell* **130**, 309–321.

Adler, J. (1973). A method for measuring chemotaxis and use of the method to determine optimum conditions for chemotaxis by *Escherichia coli*. *J. Gen. Microbiol.* **74**, 77–91.

Aizawa, S. I. (1996). Flagellar assembly in *Salmonella typhimurium*. *Mol. Microbiol.* **19**, 1–5.

Allen, L., Beijersbergen, M. W., Spreeuw, R. J. C. & Woerdman, J. P. (1992). Orbital angular momentum of light and the transformation of Laguerre-Gaussian laser modes. *Phys. Rev. A* **45**, 8185–8189.

Andrews, D. A., Xie, M., Hughes, V., Wilce, M. C. & Roujeinikova, A. (2013). Design, purification and characterization of a soluble variant of the integral membrane protein MotB for structural studies. *J. R. Soc. Interface* **10**, 20120717.

Armitage, J. P. & Schmitt, R. (1997). Bacterial chemotaxis: *Rhodobacter sphaeroides* and *Sinorhizobium meliloti* – variations on a theme? *Microbiology* **143**, 3671–3682.

Armitage, J. P., Pitta, T. P., Vigeant, M. A., Packer, H. L. & Ford, R. M. (1999). Transformations in flagellar structure of *Rhodobacter sphaeroides* and possible relationship to changes in swimming speed. *J. Bacteriol.* **181**, 4825–4833.

Armstrong, J. B., Adler, J. & Dahl, M. M. (1967). Nonchemotactic mutants of *Escherichia coli*. *J. Bacteriol.* **93**, 390–398.

Asai, Y., Kojima, S., Kato, H., Nishioka, N., Kawagishi, I. & Homma, M. (1997). Putative channel components for the fast-rotating sodium-driven flagellar motor of a marine bacterium. *J. Bacteriol.* **179**, 5104–5110.

Asai, Y., Kawagishi, I., Sockett, R. E. & Homma, M. (1999). Hybrid motor with H(+)- and Na(+)-driven components can rotate *Vibrio* polar flagella by using sodium ions. *J. Bacteriol.* **181**, 6332–6338.

Asai, Y., Kawagishi, I., Sockett, R. E. & Homma, M. (2000)a. Coupling ion specificity of chimeras between H(+)- and Na(+)-driven motor proteins, MotB and PomB, in *Vibrio* polar flagella. *EMBO J.* **19**, 3639–3648.

Asai, Y., Shoji, T., Kawagishi, I. & Homma, M. (2000)b. Cysteine-scanning mutagenesis of the periplasmic loop regions of PomA, a putative channel component of the sodium-driven flagellar motor in *Vibrio alginolyticus*. *J. Bacteriol.* **182**, 1001–1007.

Asai, Y., Yakushi, T., Kawagishi, I. & Homma, M. (2003). Ion-coupling determinants of Na(+)-driven and H(+)-driven flagellar motors. *J. Mol. Biol.* **327**, 453–463.

Ashkin, A., Dziedzic, J. M., Bjorkholm, J. E. & Chu, S. (1986). Observation of a single-beam gradient force optical trap for dielectric particles. *Opt. Lett.* **11**, 288.

Belas, R. (2014). Biofilms, flagella, and mechanosensing of surfaces by bacteria. *Trends Microbiol.* **22**, 517–527.

Berg, H. C. (1971). How to track bacteria. *Rev. Sci. Instrum.* **42**, 868–871.

Berg, H. C. (1974). Dynamic properties of bacterial flagellar motors. *Nature* **249**, 77–79.

Berg, H. C. (2003). The rotary motor of bacterial flagella. *Annu. Rev. Biochem.* **72**, 19–54.

Berg, H. C. & Anderson, R. A. (1973). Bacteria swim by rotating their flagellar filaments. *Nature* **245**, 380–382.

Berg, H. C. & Brown, D. A. (1972). Chemotaxis in *Escherichia coli* analysed by three-dimensional tracking. *Nature* **239**, 500–504.

Berg, H. C. & Turner, L. (1993). Torque generated by the flagellar motor of *Escherichia coli*. *Biophys. J.* **65**, 2201–2216.

Berry, R. M. (1993). Torque and switching in the bacterial flagellar motor. An electrostatic model. *Biophys. J.* **64**, 961–973.

Berry, R. M. (2000). Theories of rotary motors. *Philos. Trans. R. Soc. Lond. B Biol. Sci.* **355**, 503–509.

Berry, R. M. & Berg, H. C. (1996). Torque generated by the bacterial flagellar motor close to stall. *Biophys. J.* **71**, 3501–3510.

Berry, R. M. & Berg, H. C. (1997). Absence of a barrier to backwards rotation of the bacterial flagellar motor demonstrated with optical tweezers. *Proc. Natl. Acad. Sci. USA* **94**, 14433–14437.

Berry, R. M. & Berg, H. C. (1999). Torque generated by the flagellar motor of *Escherichia coli* while driven backward. *Biophys. J.* **76**, 580–587.

Berry, R. M., Turner, L. & Berg, H. C. (1995). Mechanical limits of bacterial flagellar motors probed by electrorotation. *Biophys. J.* **69**, 280–286.

Beth, R. A. (1936). Mechanical detection and measurement of the angular momentum of light. *Phys. Rev.* **50**, 115–125.

Bishop, A. I., Nieminen, T. A., Heckenberg, N. R. & Rubinsztein-Dunlop, H. (2003). Optical application and measurement of torque on microparticles of isotropic nonabsorbing material. *Phys. Rev. A* **68**, 033802.

Bishop, A. I., Nieminen, T. A., Heckenberg, N. R. & Rubinsztein-Dunlop, H. (2004). Optical microrheology using rotating laser-trapped particles. *Phys. Rev. Lett.* **92**, 198104.

Blair, D. F. (1995). How bacteria sense and swim. *Annu. Rev. Microbiol.* **49**, 489–522.

Blair, D. F. (2003). Flagellar movement driven by proton translocation. *FEBS Lett.* **545**, 86–95.

Blair, D. F. & Berg, H. C. (1988). Restoration of torque in defective flagellar motors. *Science* **242**, 1678–1681.

Blair, D. F. & Berg, H. C. (1990). The MotA protein of *E. coli* is a proton-conducting component of the flagellar motor. *Cell* **60**, 439–449.

Branch, R. W., Sayegh, M. N., Shen, C., Nathan, V. S. & Berg, H. C. (2014). Adaptive remodelling by FliN in the bacterial rotary motor. *J. Mol. Biol.* **426**, 3314–3324.

Braun, T. F. & Blair, D. F. (2001). Targeted disulfide cross-linking of the MotB protein of *Escherichia coli*: evidence for two H(+) channels in the stator Complex. *Biochemistry* **40**, 13051–13059.

Braun, T. F., Poulson, S., Gully, J. B., Empey, J. C., Van Way, S., Putnam, A. & Blair, D. F. (1999). Function of proline residues of MotA in torque generation by the flagellar motor of *Escherichia coli*. *J. Bacteriol.* **181**, 3542–3551.

Braun, T. F., Al-Mawsawi, L. Q., Kojima, S. & Blair, D. F. (2004). Arrangement of core membrane segments in the MotA/MotB proton-channel complex of *Escherichia coli*. *Biochemistry* **43**, 35–45.

Brown, M. T., Steel, B. C., Silvestrin, C., Wilkinson, D. A., Delalez, N. J., Lumb, C. N., Obara, B., Armitage, J. P. & Berry, R. M. (2012). Flagellar hook flexibility is essential for bundle formation in swimming *Escherichia coli* cells. *J. Bacteriol.* **194**, 3495–3501.

Brown, P. N., Hill, C. P. & Blair, D. F. (2002). Crystal structure of the middle and C-terminal domains of the flagellar rotor protein FliG. *EMBO J.* **21**, 3225–3234.

Brown, P. N., Mathews, M. A., Joss, L. A., Hill, C. P. & Blair, D. F. (2005). Crystal structure of the flagellar rotor protein FliN from *Thermotoga maritima*. *J. Bacteriol.* **187**, 2890–2902.

Brown, P. N., Terrazas, M., Paul, K. & Blair, D. F. (2007). Mutational analysis of the flagellar protein FliG: sites of interaction with FliM and implications for organization of the switch complex. *J. Bacteriol.* **189**, 305–312.

Calladine, C. R. (1974). Bacteria can swim without rotating flagellar filaments. *Nature* **249**, 385.

Celedon, A., Nodelman, I. M., Wildt, B., Dewan, R., Searson, P., Wirtz, D., Bowman, G. D. & Sun, S. X. (2009). Magnetic tweezers measurement of single molecule torque. *Nano Lett.* **9**, 1720–1725.

Celedon, A., Wirtz, D. & Sun, S. (2010). Torsional mechanics of DNA are regulated by small-molecule intercalation. *J. Phys. Chem. B* **114**, 16929–16935.

Chen, S., Beeby, M., Murphy, G. E., Leadbetter, J. R., Hendrixson, D. R., Briegel, A., Li, Z., Shi, J., Tocheva, E. I., Muller, A., Dobro, M. J. & Jensen, G. J. (2011). Structural diversity of bacterial flagellar motors. *EMBO J.* **30**, 2972–2981.

Chen, X. & Berg, H. C. (2000)a. Torque-speed relationship of the flagellar rotary motor of *Escherichia coli*. *Biophys. J.* **78**, 1036–1041.

Chen, X. & Berg, H. C. (2000)b. Solvent-isotope and pH effects on flagellar rotation in *Escherichia coli*. *Biophys. J.* **78**, 2280–2284.

Chernyak, B. V., Dibrov, P. A., Glagolev, A. N., Sherman, M. Yu & Skulachev, V. P. (1983). A novel type of energetics in a marine alkali-tolerant bacterium: $\Delta\mu$-Na-driven motility and sodium cycle. *FEBS Lett.* **164**, 38–42.

Chevance, F. F. & Hughes, K. T. (2008). Coordinating assembly of a bacterial macromolecular machine. *Nat. Rev. Microbiol.* **6**, 455–465.

Chun, S. Y. & Parkinson, J. S. (1988). Bacterial motility: membrane topology of the *Escherichia coli* MotB protein. *Science* **239**, 276–278.

Coulton, J. W. & Murray, R. G. (1978). Cell envelope associations of *Aquaspirillum serpens* flagella. *J. Bacteriol.* **136**, 1037–1049.

De Mot, R. & Vanderleyden, J. (1994). The C-terminal sequence conservation between OmpA-related outer membrane proteins and MotB suggests a common

function in both gram-positive and gram-negative bacteria, possibly in the interaction of these domains with peptidoglycan. *Mol. Microbiol.* **12**, 333–334.

Dean, G. E., Macnab, R. M., Stader, J., Matsumura, P. & Burks, C. (1984). Gene sequence and predicted amino acid sequence of the MotA protein, a membrane-associated protein required for flagellar rotation in *Escherichia coli*. *J. Bacteriol.* **159**, 991–999.

Delalez, N. J., Wadhams, G. H., Rosser, G., Xue, Q., Brown, M. T., Dobbie, I. M., Berry, R. M., Leake, M. C. & Armitage, J. P. (2010). Signal-dependent turnover of the bacterial flagellar switch protein FliM. *Proc. Natl. Acad. Sci. USA* **107**, 11347–11351.

Delalez, N. J., Berry, R. M. & Armitage, J. P. (2014). Stoichiometry and turnover of the bacterial flagellar switch protein FliN. *mBio* **5**, e01216–01214.

DePamphilis, M. L. & Adler, J. (1971)a. Attachment of flagellar basal bodies to the cell envelope: specific attachment to the outer, lipopolysaccharide membrane and the cytoplasmic membrane. *J. Bacteriol.* **105**, 396–407.

DePamphilis, M. L. & Adler, J. (1971)b. Purification of intact flagella from *Escherichia coli* and *Bacillus subtilis*. *J. Bacteriol.* **105**, 376–383.

DePamphilis, M. L. & Adler, J. (1971)c. Fine structure and isolation of the hook-basal body complex of flagella from *Escherichia coli* and *Bacillus subtilis*. *J. Bacteriol.* **105**, 384–395.

Deufel, C., Forth, S., Simmons, C. R., Dejgosha, S. & Wang, M. D. (2007). Nanofabricated quartz cylinders for angular trapping: DNA supercoiling torque detection. *Nat. Methods* **4**, 223–225.

Elston, T. C. & Oster, G. (1997). Protein turbines. I: The bacterial flagellar motor. *Biophys. J.* **73**, 703–721.

Fan, F. & Macnab, R. M. (1996). Enzymatic characterization of FliI. An ATPase involved in flagellar assembly in *Salmonella typhimurium*. *J. Biol. Chem.* **271**, 31981–31988.

Forth, S., Sheinin, M. Y., Inman, J. & Wang, M. D. (2013). Torque measurement at the single-molecule level. *Annu. Rev. Biophys.* **42**, 583–604.

Francis, N. R., Irikura, V. M., Yamaguchi, S., DeRosier, D. J. & Macnab, R. M. (1992). Localization of the *Salmonella typhimurium* flagellar switch protein FliG to the cytoplasmic M-ring face of the basal body. *Proc. Natl. Acad. Sci. USA* **89**, 6304–6308.

Francis, N. R., Sosinsky, G. E., Thomas, D. & DeRosier, D. J. (1994). Isolation, characterization and structure of bacterial flagellar motors containing the switch complex. *J. Mol. Biol.* **235**, 1261–1270.

Friese, M. E. J., Nieminen, T. A., Heckenberg, N. R. & Rubinsztein-Dunlop, H. (1998). Optical alignment and spinning of laser-trapped microscopic particles. *Nature* **394**, 348–350.

Fung, D. C. & Berg, H. C. (1995). Powering the flagellar motor of *Escherichia coli* with an external voltage source. *Nature* **375**, 809–812.

Funk, M., Parkin, S. J., Stilgoe, A. B., Nieminen, T. A., Heckenberg, N. R. & Rubinsztein-Dunlop, H. (2009). Constant power optical tweezers with controllable torque. *Opt. Lett.* **34**, 139–141.

Gabel, C. V. & Berg, H. C. (2003). The speed of the flagellar rotary motor of *Escherichia coli* varies linearly with protonmotive force. *Proc. Natl. Acad. Sci. USA* **100**, 8748–8751.

Galajda, P. & Ormos, P. (2003). Orientation of flat particles in optical tweezers by linearly polarized light. *Opt. Express* **11**, 446–451.

Gao, B., Lara-Tejero, M., Lefebre, M., Goodman, A. L. & Galan, J. E. (2014). Novel components of the flagellar system in epsilonproteobacteria. *mBio* **5**, e01349–01314.

Garza, A. G., Harris-Haller, L. W., Stoebner, R. A. & Manson, M. D. (1995). Motility protein interactions in the bacterial flagellar motor. *Proc. Natl. Acad. Sci. USA* **92**, 1970–1974.

Gittes, F. & Schmidt, C. F. (1998). Interference model for back-focal-plane displacement detection in optical tweezers. *Opt. Lett.* **23**, 7–9.

Gosink, K. K. & Hase, C. C. (2000). Requirements for conversion of the Na(+)-driven flagellar motor of *Vibrio* cholerae to the H(+)-driven motor of *Escherichia coli*. *J. Bacteriol.* **182**, 4234–4240.

Gosse, C. & Croquette, V. (2002). Magnetic tweezers: micromanipulation and force measurement at the molecular level. *Biophys. J.* **82**, 3314–3329.

Gutierrez-Medina, B., Andreasson, J. O., Greenleaf, W. J., Laporta, A. & Block, S. M. (2010). An optical apparatus for rotation and trapping. *Methods Enzymol.* **475**, 377–404.

Higurashi, E., Sawada, R. & Ito, T. (1999). Optically induced angular alignment of trapped birefringent micro-objects by linearly polarized light. *Phys. Rev. E* **59**, 3676–3681.

Hirota, N. & Imae, Y. (1983). Na(+)-driven flagellar motors of an alkalophilic *Bacillus* strain YN-1. *J. Biol. Chem.* **258**, 10577–10581.

Hirota, N., Kitada, M. & Imae, Y. (1981). Flagellar motors of alkalophilic *Bacillus* are powered by an electrochemical potential gradient of Na(+). *FEBS Lett.* **132**, 278–280.

Homma, M., Oota, H., Kojima, S., Kawagishi, I. & Imae, Y. (1996). Chemotactic responses to an attractant and a repellent by the polar and lateral flagellar systems of *Vibrio alginolyticus*. *Microbiology* **142**, 2777–2783.

Hosking, E. R., Vogt, C., Bakker, E. P. & Manson, M. D. (2006). The *Escherichia coli* MotAB proton channel unplugged. *J. Mol. Biol.* **364**, 921–937.

Huang, Z., Pedaci, F., van Oene, M., Wiggin, M. J. & Dekker, N. H. (2011). Electron beam fabrication of birefringent microcylinders. *ACS Nano* **5**, 1418–1427.

Inman, J., Forth, S. & Wang, M. D. (2010). Passive torque wrench and angular position detection using a single-beam optical trap. *Opt. Lett.* **35**, 2949–2951.

Inoue, Y., Lo, C. J., Fukuoka, H., Takahashi, H., Sowa, Y., Pilizota, T., Wadhams, G. H., Homma, M., Berry, R. M. & Ishijima, A. (2008). Torque-speed relationships of Na(+)-driven chimeric flagellar motors in *Escherichia coli*. *J. Mol. Biol.* **376**, 1251–1259.

Inoue, Y., Baker, M. A., Fukuoka, H., Takahashi, H., Berry, R. M. & Ishijima, A. (2013). Temperature dependences of torque generation and membrane voltage in the bacterial flagellar motor. *Biophys. J.* **105**, 2801–2810.

Ito, M., Hicks, D. B., Henkin, T. M., Guffanti, A. A., Powers, B. D., Zvi, L., Uematsu, K. & Krulwich, T. A. (2004). MotPS is the stator-

force generator for motility of alkaliphilic *Bacillus*, and its homologue is a second functional Mot in *Bacillus subtilis*. *Mol. Microbiol.* **53**, 1035–1049.

Ito, M., Terahara, N., Fujinami, S. & Krulwich, T. A. (2005). Properties of motility in *Bacillus subtilis* powered by the H(+)-coupled MotAB flagellar stator, Na(+)-coupled MotPS or hybrid stators MotAS or MotPB. *J. Mol. Biol.* **352**, 396–408.

Janssen, X. J., Lipfert, J., Jager, T., Daudey, R., Beekman, J. & Dekker, N. H. (2012). Electromagnetic torque tweezers: a versatile approach for measurement of single-molecule twist and torque. *Nano Lett.* **12**, 3634–3639.

Jefferson, K. K. (2004). What drives bacteria to produce a biofilm? *FEMS Microbiol. Lett.* **236**, 163–173.

Jenal, U., White, J. & Shapiro, L. (1994). *Caulobacter* flagellar function, but not assembly, requires FliL, a non-polarly localized membrane protein present in all cell types. *J. Mol. Biol.* **243**, 227–244.

Jones, T. B. (2003). Basic theory of dielectrophoresis and electrorotation. *IEEE Eng. Med. Biol. Mag.* **22**, 33–42.

Katayama, E., Shiraishi, T., Oosawa, K., Baba, N. & Aizawa, S. (1996). Geometry of the flagellar motor in the cytoplasmic membrane of *Salmonella typhimurium* as determined by stereo-photogrammetry of quick-freeze deep-etch replica images. *J. Mol. Biol.* **255**, 458–475.

Kauert, D. J., Kurth, T., Liedl, T. & Seidel, R. (2011). Direct mechanical measurements reveal the material properties of three-dimensional DNA origami. *Nano Lett.* **11**, 5558–5563.

Khan, I. H., Reese, T. S. & Khan, S. (1992). The cytoplasmic component of the bacterial flagellar motor. *Proc. Natl. Acad. Sci. USA* **89**, 5956–5960.

Khan, S. & Berg, H. C. (1983). Isotope and thermal effects in chemiosmotic coupling to the flagellar motor of *Streptococcus*. *Cell* **32**, 913–919.

Khan, S., Meister, M. & Berg, H. C. (1985). Constraints on flagellar rotation. *J. Mol. Biol.* **184**, 645–656.

Khan, S., Dapice, M. & Reese, T. S. (1988). Effects of mot gene expression on the structure of the flagellar motor. *J. Mol. Biol.* **202**, 575–584.

Khan, S., Khan, I. H. & Reese, T. S. (1991). New structural features of the flagellar base in *Salmonella typhimurium* revealed by rapid-freeze electron microscopy. *J. Bacteriol.* **173**, 2888–2896.

Klaue, D. & Seidel, R. (2009). Torsional stiffness of single superparamagnetic microspheres in an external magnetic field. *Phys. Rev. Lett.* **102**, 028302.

Kojima, S. & Blair, D. F. (2001). Conformational change in the stator of the bacterial flagellar motor. *Biochemistry* **40**, 13041–13050.

Kojima, S. & Blair, D. F. (2004). Solubilization and purification of the MotA/MotB complex of *Escherichia coli*. *Biochemistry* **43**, 26–34.

Kojima, S., Imada, K., Sakuma, M., Sudo, Y., Kojima, C., Minamino, T., Homma, M. & Namba, K. (2009). Stator assembly and activation mechanism of the flagellar motor by the periplasmic region of MotB. *Mol. Microbiol.* **73**, 710–718.

Kubori, T., Shimamoto, N., Yamaguchi, S., Namba, K. & Aizawa, S. (1992). Morphological pathway of flagellar assembly in *Salmonella typhimurium*. *J. Mol. Biol.* **226**, 433–446.

Kudo, S., Magariyama, Y. & Aizawa, S. (1990). Abrupt changes in flagellar rotation observed by laser dark-field microscopy. *Nature* **346**, 677–680.

La Porta, A. & Wang, M. D. (2004). Optical torque wrench: angular trapping, rotation, and torque detection of quartz microparticles. *Phys. Rev. Lett.* **92**, 190801.

Lam, K. H., Ip, W. S., Lam, Y. W., Chan, S. O., Ling, T. K. & Au, S. W. (2012). Multiple conformations of the FliG C-terminal domain provide insight into flagellar motor switching. *Structure* **20**, 315–325.

Lam, K. H., Lam, W. W., Wong, J. Y., Chan, L. C., Kotaka, M., Ling, T. K., Jin, D. Y., Ottemann, K. M. & Au, S. W. (2013). Structural basis of FliG-FliM interaction in *Helicobacter pylori*. *Mol. Microbiol.* **88**, 798–812.

Larsen, S. H., Adler, J., Gargus, J. J. & Hogg, R. W. (1974)a. Chemomechanical coupling without ATP: the source of energy for motility and chemotaxis in bacteria. *Proc. Natl. Acad. Sci. USA* **71**, 1239–1243.

Larsen, S. H., Reader, R. W., Kort, E. N., Tso, W. W. & Adler, J. (1974)b. Change in direction of flagellar rotation is the basis of the chemotactic response in *Escherichia coli*. *Nature* **249**, 74–77.

Läuger, P. (1977). Ion transport and rotation of bacterial flagella. *Nature* **268**, 360–362.

Läuger, P. (1988). Torque and rotation rate of the bacterial flagellar motor. *Biophys. J.* **53**, 53–65.

Leake, M. C., Chandler, J. H., Wadhams, G. H., Bai, F., Berry, R. M. & Armitage, J. P. (2006). Stoichiometry and turnover in single, functioning membrane protein complexes. *Nature* **443**, 355–358.

Lebel, P., Basu, A., Oberstrass, F. C., Tretter, E. M. & Bryant, Z. (2014). Gold rotor bead tracking for high-speed measurements of DNA twist, torque and extension. *Nat. Methods* **11**, 456–462.

Lee, L. K., Ginsburg, M. A., Crovace, C., Donohoe, M. & Stock, D. (2010). Structure of the torque ring of the flagellar motor and the molecular basis for rotational switching. *Nature* **466**, 996–1000.

Lee, Y. Y. & Belas, R. (2014). Loss of FliL alters Proteus mirabilis surface-sensing and temperature-dependent swarming. *J. Bacteriol.*

Lele, P. P., Hosu, B. G. & Berg, H. C. (2013). Dynamics of mechanosensing in the bacterial flagellar motor. *Proc. Natl. Acad. Sci. USA* **110**, 11839–11844.

Li, G. & Tang, J. X. (2006). Low flagellar motor torque and high swimming efficiency of *Caulobacter crescentus* swarmer cells. *Biophys. J.* **91**, 2726–2734.

Li, N., Kojima, S. & Homma, M. (2011). Sodium-driven motor of the polar flagellum in marine bacteria *Vibrio*. *Genes Cells* **16**, 985–999.

Lipfert, J., Hao, X. & Dekker, N. H. (2009). Quantitative modeling and optimization of magnetic tweezers. *Biophys. J.* **96**, 5040–5049.

Lipfert, J., Kerssemakers, J. W., Jager, T. & Dekker, N. H. (2010). Magnetic torque tweezers: measuring torsional stiffness in DNA and RecA-DNA filaments. *Nat. Methods* **7**, 977–980.

Lipfert, J., Wiggin, M. J., Kerssemakers, J. W. J., Pedaci, F. & Dekker, N. H. (2011). Freely orbiting magnetic tweezers to directly monitor changes in the twist of nucleic acids. *Nat. Commun.* **2**, 439.

Liu, B., Gulino, M., Morse, M., Tang, J. X., Powers, T. R. & Breuer, K. S. (2014). Helical motion of the cell body enhances *Caulobacter crescentus* motility. *Proc. Natl. Acad. Sci. USA* **111**, 11252–11256.

Lloyd, S. A. & Blair, D. F. (1997). Charged residues of the rotor protein FliG essential for torque generation in the flagellar motor of *Escherichia coli*. *J. Mol. Biol.* **266**, 733–744.

Lloyd, S. A., Whitby, F. G., Blair, D. F. & Hill, C. P. (1999). Structure of the C-terminal domain of FliG, a component of the rotor in the bacterial flagellar motor. *Nature* **400**, 472–475.

Lo, C. J., Leake, M. C. & Berry, R. M. (2006). Fluorescence measurement of intracellular sodium concentration in single *Escherichia coli* cells. *Biophys. J.* **90**, 357–365.

Lo, C. J., Leake, M. C., Pilizota, T. & Berry, R. M. (2007). Nonequivalence of membrane voltage and ion-gradient as driving forces for the bacterial flagellar motor at low load. *Biophys. J.* **93**, 294–302.

Lo, C. J., Sowa, Y., Pilizota, T. & Berry, R. M. (2013). Mechanism and kinetics of a sodium-driven bacterial flagellar motor. *Proc. Natl. Acad. Sci. USA* **110**, E2544–2551.

Lowe, G., Meister, M. & Berg, H. C. (1987). Rapid rotation of flagellar bundles in swimming bacteria. *Nature* **325**, 637–640.

Macnab, R. & Koshland, Jr., D. E. (1974). Bacterial motility and chemotaxis: light-induced tumbling response and visualization of individual flagella. *J. Mol. Biol.* **84**, 399–406.

Macnab, R. M. (1976). Examination of bacterial flagellation by dark-field microscopy. *J. Clin. Microbiol.* **4**, 258–265.

Macnab, R. M. (2003). How bacteria assemble flagella. *Annu. Rev. Microbiol.* **57**, 77–100.

Macnab, R. M. (2004). Type III flagellar protein export and flagellar assembly. *Biochim. Biophys. Acta* **1694**, 207–217.

Magariyama, Y., Sugiyama, S., Muramoto, K., Maekawa, Y., Kawagishi, I., Imae, Y. & Kudo, S. (1994). Very fast flagellar rotation. *Nature* **371**, 752.

Manson, M. D., Tedesco, P., Berg, H. C., Harold, F. M. & Van der Drift, C. (1977). A protonmotive force drives bacterial flagella. *Proc. Natl. Acad. Sci. USA* **74**, 3060–3064.

Manson, M. D., Tedesco, P. M. & Berg, H. C. (1980). Energetics of flagellar rotation in bacteria. *J. Mol. Biol.* **138**, 541–561.

Matsuura, S, Shioi, J & Imae, Y. (1977). Motility in *Bacillus subtilis* driven by an artificial protonmotive force. *FEBS Lett.* **82**, 187–190.

McCarter, L. L. (1994)a. MotY, a component of the sodium-type flagellar motor. *J. Bacteriol.* **176**, 4219–4225.

McCarter, L. L. (1994)b. MotX, the channel component of the sodium-type flagellar motor. *J. Bacteriol.* **176**, 5988–5998.

Meacci, G. & Tu, Y. (2009). Dynamics of the bacterial flagellar motor with multiple stators. *Proc. Natl. Acad. Sci. USA* **106**, 3746–3751.

Meacci, G., Lan, G. & Tu, Y. (2011). Dynamics of the bacterial flagellar motor: the effects of stator compliance, back steps, temperature, and rotational asymmetry. *Biophys. J.* **100**, 1986–1995.

Meister, M. & Berg, H. C. (1987). The stall torque of the bacterial flagellar motor. *Biophys. J.* **52**, 413–419.

Meister, M., Lowe, G. & Berg, H. C. (1987). The proton flux through the bacterial flagellar motor. *Cell* **49**, 643–650.

Meister, M., Caplan, S. R. & Berg, H. C. (1989). Dynamics of a tightly coupled mechanism for flagellar rotation. Bacterial motility, chemiosmotic coupling, protonmotive force. *Biophys. J.* **55**, 905–914.

Minamino, T. & Namba, K. (2004). Self-assembly and type III protein export of the bacterial flagellum. *J. Mol. Microbiol. Biotechnol.* **7**, 5–17.

Minamino, T. & Namba, K. (2008). Distinct roles of the FliI ATPase and proton motive force in bacterial flagellar protein export. *Nature* **451**, 485–488.

Minamino, T., Imada, K., Kinoshita, M., Nakamura, S., Morimoto, Y. V. & Namba, K. (2011). Structural insight into the rotational switching mechanism of the bacterial flagellar motor. *PLoS Biol.* **9**, e1000616.

Mitchell, P. (1966). Chemiosmotic coupling in oxidative and photosynthetic phosphorylation. *Biol. Rev. Camb. Philos. Soc.* **41**, 445–502.

Molloy, J. E., Burns, J. E., Kendrick-Jones, J., Tregear, R. T. & White, D. C. (1995). Movement and force produced by a single myosin head. *Nature* **378**, 209–212.

Monds, R. D. & O'Toole, G. A. (2009). The developmental model of microbial biofilms: ten years of a paradigm up for review. *Trends Microbiol.* **17**, 73–87.

Mora, T., Yu, H., Sowa, Y. & Wingreen, N. S. (2009)a. Steps in the bacterial flagellar motor. *PLoS Comput Biol* **5**, e1000540.

Mora, T., Yu, H. & Wingreen, N. S. (2009)b. Modeling torque versus speed, shot noise, and rotational diffusion of the bacterial flagellar motor. *Phys. Rev. Lett.* **103**, 248102.

Morimoto, Y. V. & Minamino, T. (2014). Structure and function of the bi-directional bacterial flagellar motor. *Biomolecules* **4**, 217–234.

Mosconi, F., Allemand, J. F. & Croquette, V. (2011). Soft magnetic tweezers: a proof of principle. *Rev. Sci. Instrum.* **82**, 034302.

Muramoto, K., Kawagishi, I., Kudo, S., Magariyama, Y., Imae, Y. & Homma, M. (1995). High-speed rotation and speed stability of the sodium-driven flagellar motor in *Vibrio alginolyticus*. *J. Mol. Biol.* **251**, 50–58.

Murphy, G. E., Leadbetter, J. R. & Jensen, G. J. (2006). In situ structure of the complete *Treponema primitia* flagellar motor. *Nature* **442**, 1062–1064.

Neuman, K. C., Chadd, E. H., Liou, G. F., Bergman, K. & Block, S. M. (1999). Characterization of photodamage to *Escherichia coli* in optical traps. *Biophys. J.* **77**, 2856–2863.

Nieminen, T. A., Heckenberg, N. R. & Rubinsztein-Dunlop, H. (2001). Optical measurement of microscopic torques. *J. Mod. Opt.* **48**, 405–413.

Normanno, D., Capitanio, M. & Pavone, F. S. (2004). Spin absorption, windmill, and magneto-optic effects in optical angular momentum transfer. *Phys. Rev. A* **70**, 053829.

Obara, M., Yakushi, T., Kojima, S. & Homma, M. (2008). Roles of charged residues in the C-terminal region of PomA, a stator component of the Na(+)-driven flagellar motor. *J. Bacteriol.* **190**, 3565–3571.

O'Neil, A. T. & Padgett, M. J. (2002). Rotational control within optical tweezers by use of a rotating aperture. *Opt. Lett.* **27**, 743–745.

O'Neill, J. & Roujeinikova, A. (2008). Cloning, purification and crystallization of MotB, a stator component of the proton-driven bacterial flagellar motor. *Acta Crystallogr. Sect. F Struct. Biol. Cryst. Commun.* **64**, 561–563.

O'Neill, J., Xie, M., Hijnen, M. & Roujeinikova, A. (2011). Role of the MotB linker in the assembly and activation of the bacterial flagellar motor. *Acta Crystallogr. D Biol. Crystallogr.* **67**, 1009–1016.

Oosawa, F. & Hayashi, S. (1986). The loose coupling mechanism in molecular machines of living cells. *Adv. Biophys.* **22**, 151–183.

Oosawa, K., Ueno, T. & Aizawa, S. (1994). Overproduction of the bacterial flagellar switch proteins and their interactions with the MS ring complex *in vitro*. *J. Bacteriol.* **176**, 3683–3691.

Oroszi, L., Galajda, P., Kirei, H., Bottka, S. & Ormos, P. (2006). Direct measurement of torque in an optical trap and Its application to double-strand DNA. *Phys. Rev. Lett.* **97**, 058301.

Park, S. Y., Lowder, B., Bilwes, A. M., Blair, D. F. & Crane, B. R. (2006). Structure of FliM provides insight into assembly of the switch complex in the bacterial flagella motor. *Proc. Natl. Acad. Sci. USA* **103**, 11886–11891.

Parkin, S. J., Vogel, R., Persson, M., Funk, M., Loke, V. L., Nieminen, T. A., Heckenberg, N. R. & Rubinsztein-Dunlop, H. (2009). Highly birefringent vaterite microspheres: production, characterization and applications for optical micromanipulation. *Opt. Express* **17**, 21944–21955.

Parkinson, J. S. (1976). cheA, cheB, and cheC genes of *Escherichia coli* and their role in chemotaxis. *J. Bacteriol.* **126**, 758–770.

Parkinson, J. S. (1978). Complementation analysis and deletion mapping of *Escherichia coli* mutants defective in chemotaxis. *J. Bacteriol.* **135**, 45–53.

Paul, K., Erhardt, M., Hirano, T., Blair, D. F. & Hughes, K. T. (2008). Energy source of flagellar type III secretion. *Nature* **451**, 489–492.

Paul, K., Gonzalez-Bonet, G., Bilwes, A. M., Crane, B. R. & Blair, D. (2011). Architecture of the flagellar rotor. *EMBO J.* **30**, 2962–2971.

Paulick, A., Koerdt, A., Lassak, J., Huntley, S., Wilms, I., Narberhaus, F. & Thormann, K. M. (2009). Two different stator systems drive a single polar flagellum in *Shewanella oneidensis* MR-1. *Mol. Microbiol.* **71**, 836–850.

Pedaci, F., Huang, Z., van Oene, M., Barland, S. & Dekker, N. H. (2011). Excitable particles in an optical torque wrench. *Nature Phys.* **7**, 259–264.

Pilizota, T., Bilyard, T., Bai, F., Futai, M., Hosokawa, H. & Berry, R. M. (2007). A programmable optical angle clamp for rotary molecular motors. *Biophys. J.* **93**, 264–275.

Purcell, E. M. (1977). Life at low Reynold's number. *Am. J. Phys.* **45**, 3–11.

Raha, M., Sockett, H. & Macnab, R. M. (1994). Characterization of the fliL gene in the flagellar regulon of *Escherichia coli* and *Salmonella typhimurium*. *J. Bacteriol.* **176**, 2308–2311.

Reboul, C. F., Andrews, D. A., Nahar, M. F., Buckle, A. M. & Roujeinikova, A. (2011). Crystallographic and molecular dynamics analysis of loop motions unmasking the peptidoglycan-binding site in stator protein MotB of flagellar motor. *PLoS One* **6**, e18981.

Reid, S. W., Leake, M. C., Chandler, J. H., Lo, C. J., Armitage, J. P. & Berry, R. M. (2006). The maximum number of torque-generating units in the flagellar motor of *Escherichia coli* is at least 11. *Proc. Natl. Acad. Sci. USA* **103**, 8066–8071.

Rondelez, Y., Tresset, G., Nakashima, T., Kato-Yamada, Y., Fujita, H., Takeuchi, S. & Noji, H. (2005). Highly coupled ATP synthesis by F1-ATPase single molecules. *Nature* **433**, 773–777.

Roujeinikova, A. (2008)a. Cloning, purification and preliminary X-ray analysis of the C-terminal domain of *Helicobacter pylori* MotB. *Acta Crystallogr. Sect. F Struct. Biol. Cryst. Commun.* **64**, 277–280.

Roujeinikova, A. (2008)b. Crystal structure of the cell wall anchor domain of MotB, a stator component of the bacterial flagellar motor: implications for peptidoglycan recognition. *Proc. Natl. Acad. Sci. USA* **105**, 10348–10353.

Rowe, A. D. (2005). *Rotation of the sodium driven bacterial flagellar motor.* D.Phil. thesis, University of Oxford.

Ryu, W. S., Berry, R. M. & Berg, H. C. (2000). Torque-generating units of the flagellar motor of *Escherichia coli* have a high duty ratio. *Nature* **403**, 444–447.

Sato, K. & Homma, M. (2000). Functional reconstitution of the Na(+)-driven polar flagellar motor component of *Vibrio alginolyticus*. *J. Biol. Chem.* **275**, 5718–5722.

Saxl, T. E. (2007). *Electrorotation of the bacterial flagellar motor.* D.Phil. thesis, University of Oxford.

Sharp, L. L., Zhou, J. & Blair, D. F. (1995)a. Tryptophan-scanning mutagenesis of MotB, an integral membrane protein essential for flagellar rotation in *Escherichia coli*. *Biochemistry* **34**, 9166–9171.

Sharp, L. L., Zhou, J. & Blair, D. F. (1995)b. Features of MotA proton channel structure revealed by tryptophan-scanning mutagenesis. *Proc. Natl. Acad. Sci. USA* **92**, 7946–7950.

Silverman, M. R. & Simon, M. I. (1972). Flagellar assembly mutants in *Escherichia coli*. *J. Bacteriol.* **112**, 986–993.

Silverman, M. R. & Simon, M. I. (1974). Flagellar rotation and the mechanism of bacterial motility. *Nature* **249**, 73–74.

Simpson, N. B., Dholakia, K., Allen, L. & Padgett, M. J. (1997). Mechanical equivalence of spin and orbital angular momentum of light: an optical spanner. *Opt. Lett.* **22**, 52–54.

Sircar, R., Borbat, P. P., Lynch, M. J., Bhatnagar, J., Beyersdorf, M. S., Halkides, C. J., Freed, J. H. & Crane, B. R. (2014). Assembly States of FliM and FliG within the Flagellar Switch Complex. *J. Mol. Biol.*

Son, K., Guasto, J. S. & Stocker, R. (2013). Bacteria can exploit a flagellar buckling instability to change direction. *Nat Phys* **9**, 494–498.

Sourjik, V. & Schmitt, R. (1996). Different roles of CheY1 and CheY2 in the chemotaxis of *Rhizobium meliloti*. *Mol. Microbiol.* **22**, 427–436.

Sowa, Y. & Berry, R. M. (2008). Bacterial flagellar motor. *Q. Rev. Biophys.* **41**, 103–132.

Sowa, Y., Hotta, H., Homma, M. & Ishijima, A. (2003). Torque-speed relationship of the Na(+)-driven flagellar motor of *Vibrio alginolyticus*. *J. Mol. Biol.* **327**, 1043–1051.

Sowa, Y., Rowe, A. D., Leake, M. C., Yakushi, T., Homma, M., Ishijima, A. & Berry, R. M. (2005). Direct observation of steps in rotation of the bacterial flagellar motor. *Nature* **437**, 916–919.

Sowa, Y., Steel, B. C. & Berry, R. M. (2010). A simple backscattering microscope for fast tracking of biological molecules. *Rev. Sci. Instrum.* **81**, 113704.

Sowa, Y., Homma, M., Ishijima, A. & Berry, R. M. (2014). Hybrid-fuel bacterial flagellar motors in *Escherichia coli*. *Proc. Natl. Acad. Sci. USA* **111**, 3436–3441.

Stader, J., Matsumura, P., Vacante, D., Dean, G. E. & Macnab, R. M. (1986). Nucleotide sequence of the *Escherichia coli* MotB gene and site-limited incorporation of its product into the cytoplasmic membrane. *J. Bacteriol.* **166**, 244–252.

Stallmeyer, M. J., Aizawa, S., Macnab, R. M. & DeRosier, D. J. (1989). Image reconstruction of the flagellar basal body of *Salmonella typhimurium*. *J. Mol. Biol.* **205**, 519–528.

Stock, D., Namba, K. & Lee, L. K. (2012). Nanorotors and self-assembling macromolecular machines: the torque ring of the bacterial flagellar motor. *Curr. Opin. Biotechnol.* **23**, 545–554.

Strick, T. R., Allemand, J. F., Bensimon, D., Bensimon, A. & Croquette, V. (1996). The elasticity of a single supercoiled DNA molecule. *Science* **271**, 1835–1837.

Suzuki, H., Yonekura, K. & Namba, K. (2004). Structure of the rotor of the bacterial flagellar motor revealed by electron cryomicroscopy and single-particle image analysis. *J. Mol. Biol.* **337**, 105–113.

Svoboda, K., Schmidt, C. F., Schnapp, B. J. & Block, S. M. (1993). Direct observation of kinesin stepping by optical trapping interferometry. *Nature* **365**, 721–727.

Terashima, H., Fukuoka, H., Yakushi, T., Kojima, S. & Homma, M. (2006). The *Vibrio* motor proteins, MotX and MotY, are associated with the basal body of Na-driven flagella and required for stator formation. *Mol. Microbiol.* **62**, 1170–1180.

Terashima, H., Kojima, S. & Homma, M. (2010). Functional transfer of an essential aspartate for the ion-binding site in the stator proteins of the bacterial flagellar motor. *J. Mol. Biol.* **397**, 689–696.

Thomas, D. R., Morgan, D. G. & DeRosier, D. J. (1999). Rotational symmetry of the C ring and a mechanism for the flagellar rotary motor. *Proc. Natl. Acad. Sci. USA* **96**, 10134–10139.

Thomas, D. R., Francis, N. R., Xu, C. & DeRosier, D. J. (2006). The three-dimensional structure of the flagellar rotor from a clockwise-locked mutant of Salmonella enterica serovar Typhimurium. *J. Bacteriol.* **188**, 7039–7048.

Thormann, K. M. & Paulick, A. (2010). Tuning the flagellar motor. *Microbiology* **156**, 1275–1283.

Tipping, M. J., Delalez, N. J., Lim, R., Berry, R. M. & Armitage, J. P. (2013)a. Load-dependent assembly of the bacterial flagellar motor. *mBio* **4**, e00551–00513.

Tipping, M. J., Steel, B. C., Delalez, N. J., Berry, R. M. & Armitage, J. P. (2013)b. Quantification of flagellar motor stator dynamics through in vivo proton-motive force control. *Mol. Microbiol.* **87**, 338–347.

Togashi, F., Yamaguchi, S., Kihara, M., Aizawa, S. I. & Macnab, R. M. (1997). An extreme clockwise switch bias mutation in fliG of *Salmonella typhimurium* and its suppression by slow-motile mutations in MotA and MotB. *J. Bacteriol.* **179**, 2994–3003.

Turner, L., Ryu, W. S. & Berg, H. C. (2000). Real-time imaging of fluorescent flagellar filaments. *J. Bacteriol.* **182**, 2793–2801.

Turner, L., Stern, A. S. & Berg, H. C. (2012). Growth of flagellar filaments of *Escherichia coli* is independent of filament length. *J. Bacteriol.* **194**, 2437–2442.

Ueno, T., Oosawa, K. & Aizawa, S. (1992). M ring, S ring and proximal rod of the flagellar basal body of *Salmonella typhimurium* are composed of subunits of a single protein, FliF. *J. Mol. Biol.* **227**, 672–677.

Ueno, T., Oosawa, K. & Aizawa, S. (1994). Domain structures of the MS ring component protein (FliF) of the flagellar basal body of *Salmonella typhimurium*. *J. Mol. Biol.* **236**, 546–555.

Vartanian, A. S., Paz, A., Fortgang, E. A., Abramson, J. & Dahlquist, F. W. (2012). Structure of flagellar motor proteins in complex allows for insights into motor structure and switching. *J. Biol. Chem.* **287**, 35779–35783.

Vogel, R., Persson, M., Feng, C., Parkin, S. J., Nieminen, T. A., Wood, B., Heckenberg, N. R. & Rubinsztein-Dunlop, H. (2009). Synthesis and surface modification of birefringent vaterite microspheres. *Langmuir* **25**, 11672–11679.

Wadhams, G. H. & Armitage, J. P. (2004). Making sense of it all: bacterial chemotaxis. *Nat. Rev. Mol. Cell Biol.* **5**, 1024–1037.

Walz, D. & Caplan, S. R. (2000). An electrostatic mechanism closely reproducing observed behavior in the bacterial flagellar motor. *Biophys. J.* **78**, 626–651.

Washizu, M., Kurahashi, Y., Iochi, H., Kurosawa, O., Aizawa, S., Kudo, S., Magariyama, Y. & Hotani, H. (1993). Dielectrophoretic measurement of bacterial motor characteristics. *IEEE Trans. Ind. Appl.* **29**, 286–294.

Xing, J., Bai, F., Berry, R. & Oster, G. (2006). Torque-speed relationship of the bacterial flagellar motor. *Proc. Natl. Acad. Sci. USA* **103**, 1260–1265.

Yakushi, T., Maki, S. & Homma, M. (2004). Interaction of PomB with the third transmembrane segment of PomA in the Na(+)-driven polar flagellum of *Vibrio alginolyticus*. *J. Bacteriol.* **186**, 5281–5291.

Yakushi, T., Yang, J., Fukuoka, H., Homma, M. & Blair, D. F. (2006). Roles of charged residues of rotor and stator in flagellar rotation: comparative study using H(+)-driven and Na(+)-driven motors in *Escherichia coli*. *J. Bacteriol.* **188**, 1466–1472.

Yamaguchi, S., Aizawa, S., Kihara, M., Isomura, M., Jones, C. J. & Macnab, R. M. (1986)a. Genetic evidence for a switching and energy-transducing complex in the flagellar motor of *Salmonella typhimurium*. *J. Bacteriol.* **168**, 1172–1179.

Yamaguchi, S., Fujita, H., Ishihara, A., Aizawa, S. & Macnab, R. M. (1986)b. Subdivision of flagellar genes of *Salmonella typhimurium* into regions responsible for assembly, rotation, and switching. *J. Bacteriol.* **166**, 187–193.

Yorimitsu, T. & Homma, M. (2001). Na(+)-driven flagellar motor of *Vibrio*. *Biochim. Biophys. Acta* **1505**, 82–93.

Yorimitsu, T., Sowa, Y., Ishijima, A., Yakushi, T. & Homma, M. (2002). The systematic substitutions around the conserved charged residues of the cytoplasmic loop of Na(+)-driven flagellar motor component PomA. *J. Mol. Biol.* **320**, 403–413.

Yorimitsu, T., Mimaki, A., Yakushi, T. & Homma, M. (2003). The conserved charged residues of the C-terminal region of FliG, a rotor component of the Na(+)-driven flagellar motor. *J. Mol. Biol.* **334**, 567–583.

Yuan, J. & Berg, H. C. (2008). Resurrection of the flagellar rotary motor near zero load. *Proc. Natl. Acad. Sci. USA* **105**, 1182–1185.

Yuan, J. & Berg, H. C. (2010). Thermal and solvent-isotope effects on the flagellar rotary motor near zero load. *Biophys. J.* **98**, 2121–2126.

Zhao, X., Zhang, K., Boquoi, T., Hu, B., Motaleb, M. A., Miller, K. A., James, M. E., Charon, N. W., Manson, M. D., Norris, S. J., Li, C. & Liu, J. (2013). Cryoelectron tomography reveals the sequential assembly of bacterial flagella in *Borrelia burgdorferi*. *Proc. Natl. Acad. Sci. USA* **110**, 14390–14395.

Zhao, X., Norris, S. J. & Liu, J. (2014). Molecular architecture of the bacterial flagellar motor in cells. *Biochemistry* **53**, 4323–4333.

Zhou, J. & Blair, D. F. (1997). Residues of the cytoplasmic domain of MotA essential for torque generation in the bacterial flagellar motor. *J. Mol. Biol.* **273**, 428–439.

Zhou, J., Lloyd, S. A. & Blair, D. F. (1998)a. Electrostatic interactions between rotor and stator in the bacterial flagellar motor. *Proc. Natl. Acad. Sci. USA* **95**, 6436–6441.

Zhou, J., Sharp, L. L., Tang, H. L., Lloyd, S. A., Billings, S., Braun, T. F. & Blair, D. F. (1998)b. Function of protonatable residues in the flagellar motor of *Escherichia coli*: a critical role for Asp 32 of MotB. *J. Bacteriol.* **180**, 2729–2735.